UNIVERSITÉ DU QUÉBEC À MONTRÉAL

SCALE-DECOMPOSED QUANTITATIVE STUDIES OF THE ATMOSPHERIC WATER BUDGET OVER AFRICA, AS SIMULATED BY THE FIFTH. GENERATION CANADIAN REGIONAL CLIMATE MODEL (CRCM5)

THESIS

PRESENTED AS PARTIAL REQUIREMENT

OF THE MASTERS OF ATMOSPHERIC SCIENCES

BY

VALENTINA MINKOVSKA

JANUARY 2013

UNIVERSITÉ DU QUÉBEC À MONTRÉAL

ÉTUDE QUANTITATIVE DU BILAN D'EAU ATMOSPHÉRIQUE SUR L'AFRIQUE AVEC DÉCOMPOSITION D'ÉCHELLE, TEL QUE SIMULÉ PAR LE MODÈLE RÉGIONAL CANADIEN DU CLIMAT, VERSION 5 (MRCC5)

MÉMOIRE

PRÉSENTÉ COMME EXIGENCE PARTIELLE

DE LA MAÎTRISE EN SCIENCES DE L'ATMOSPHÈRE

PAR

VALENTINA MINKOVSKA

JANVIER 2013

REMERCIEMENTS

Je voudrais tout d'abord remercier le Professeur René Laprise, mon directeur de recherche, pour les précieux conseils et l'encadrement qu'il m'a fourni afin de réaliser ce travail. Ses vastes connaissances scientifiques, qualités pédagogiques et son écoute attentive étaient une grande inspiration pour moi. Je lui suis reconnaissante pour l'aide et le temps qu'il a bien voulu me consacrer, malgré ses autres charges académiques et professionnelles. Je le remercie, ainsi que le Centre ESCER, pour le financement reçu tout au long de mes études.

Mes remerciements s'adressent aussi à Katja Winger, agente de recherche, pour avoir mis à ma disposition les données analysées dans ce mémoire, et à Bernard Dugas, chercheur à Environnement Canada et professeur associé au Centre ESCER, pour la résolution expéditive de problèmes survenus pendant les tests préliminaires.

Je suis reconnaissante à Nadjet Labassi, analyste informatique, et Georges Huard, technicien en informatique, qui ont fourni un support informatique efficace pour que je puisse effectuer mes tâches.

Ma gratitude va également à tous mes enseignants de l'UQAM et tous mes collègues, qui m'ont apporté leur appui moral et intellectuel.

Finalement, je tiens à remercier mes amis, ma famille, et surtout mes parents, qui m'ont toujours soutenue et encouragée dans les périodes difficiles.

TABLE DES MATIÈRES

LISTE DES FIGURES

LISTE DES ABRÉVIATIONS ET ACRONYMES

AEJ	African Easterly Jet
AEW	African Easterly Waves
AMIP2	Atmospheric Model Intercomparison Project, version 2
AV	Added value
CGCM	Canadian Global Climate Model
CLASS	Canadian Land-Surface Scheme
CRCM	Canadian Regional Climate Model
CRCM5	Canadian Regional Climate Model (version 5)
CRU	Climatic Research Unit
CORDEX	COordinated Regional climate Downscaling EXperiment
DCT	Discrete Cosine Transform
DJF	December – January - February
DRC	Democratic Republic of Congo
Fig.	Figure
GCM	Global Climate Model

GPCP	Global Precipitation Climatology Project
HMDC	Historical and Meteorological Data Center
IPCC	Intergovernemental Panel on Climate Change
ITCZ	Inter-Tropical Convergence Zone
ITD	Inter-Tropical Discontinuity
JJA	June – July - August
MCS	Mesoscale Convective Systems
NCEP/GFS	National Centers for Environmental Prediction/ Global Forecast System
PAV	Potential Added value
RCM	Regional Climate Model
SHL	Saharan Heat Low
SST	Sea Surface Temperature
STD	Standard deviation
TEJ	Tropical Easterly Jet
TRMM	Tropical Rainfall Measuring Mission
WAM	West African Monsoon
WVB	Water Vapour Budget

LISTE DES SYMBOLES

$\overline{(*)}$	Intégration verticale
$[*]$	Moyenne temporelle
$(*)'$	Déviation par rapport à la moyenne temporelle
$\mathrm{cov}(*\,,*)$	Covariance
$\partial_t(*)$	Dérivée temporelle locale (s^{-1})
$\nabla \cdot (*)$	Divergence horizontale (m^{-1})
λ	Latitude géographique
φ	Longitude géographique
ψ	Variable (humidité spécifique ou flux horizontal d'humidité atmosphérique)
$\sum$	Somme
L	Indice des grandes échelles
L_v	Chaleur latente d'évaporation
p	Niveau de pression
P	Précipitation à la surface (mm/jour)

q	Humidité spécifique
r	Rayon de la Terre
R	Indice de terme «Resolved divergence»
S	Indice des petites échelles
(u,v)	Composantes zonale et méridienne du vent horizontal
U	Indice de terme «Unresolved divergence»
V	Vent horizontal (m/s)
X	Variable quelconque
$X_{j,y}$	Archive de la variable X au pas de temps j de l'année *y*
$[X]_y^J$	Moyenne saisonnière de la variable X pour l'année *y*
$[X]^{J,Y}$	Moyenne saisonnière climatologique de la variable X
y	Indice d'année
Y	Nombre d'années

RÉSUMÉ

Pendant les dernières années, l'Afrique est affectée par des fluctuations dramatiques des précipitations, qui ont des effets dévastateurs sur l'économie, la santé et la subsistance de la population. L'adaptation aux changements climatiques nécessite une étude approfondie du cycle hydrologique, menant aux projections climatiques améliorées sur le continent.

Les objectifs de ce mémoire sont de tester les performances de la cinquième génération du Modèle régional canadien du climat (MRCC5) dans la simulation du bilan de l'eau atmosphérique sur l'Afrique à l'été (JJA) et en hiver (DJF) et d'évaluer la valeur ajoutée potentielle (VAP) du modèle, concernant la moyenne saisonnière et la variabilité temporelle. À cette fin, chacune des variables atmosphériques est décomposée en grandes échelles, résolues par le MRCC5 et la réanalyse ERA-Interim qui pilote le MRCC5, et de petites échelles, non résolues par la réanalyse. De plus, la divergence du flux d'humidité horizontale intégrée verticalement est représentée comme une somme des quatre termes d'interaction, obtenue à partir du vent et de l'humidité décomposés dans l'espace. La divergence moyenne saisonnière est également décomposée en deux termes, résultant de la contribution des tourbillons stationnaires et transitoires. La valeur ajoutée potentielle est associée aux petites échelles des moyennes saisonnières, à la divergence non résolue, et à leurs variances.

Les résultats révèlent que le bilan moyen saisonnier de l'eau atmosphérique est dominé par les grandes échelles. La contribution des petites échelles est limitée et localisée sur le terrain escarpé et le long de la côte. La divergence moyenne du flux d'humidité intégrée verticalement est contrôlée par la composante stationnaire, tandis que la composante transitoire est présentée essentiellement dans le front intertropical et latitudes tempérées. Les deux composantes sont étroitement liées à la circulation tridimensionnelle associée à la dépression saharienne. Il a été démontré que la divergence non résolue résulte principalement de l'interaction entre le vent à petite échelle et l'humidité à grande échelle, et que sa contribution est moindre que de la divergence résolue. Finalement, la VAP pour la divergence moyenne de l'humidité est due principalement au forçage topographique et découle en parti de la composante résolue.

Pour conclure, la variabilité climatologique du cycle hydrologique de l'atmosphère est marquée par un apport essentiel des petites échelles déterminant la supériorité de la variance de divergence non résolue du flux d'humidité. Les termes d'interaction dominants sont identifiés pour les principales régions géographiques. L'écart-type maximal observé dans la zone de convergence intertropicale, l'Océan Indien, l'Atlantique Central et les latitudes moyennes suggère une VAP significative avec origine synoptique et convective pour la variabilité.

Mots-clés : MRCC5, valeur ajoutée, décomposition d'échelle, bilan d'eau atmosphérique, divergence du flux d'humidité, Afrique.

ABSTRACT

In recent years Africa is affected by dramatic rainfall fluctuations having devastating impacts on the economy, health and livelihoods of people. Better adaptation of the African population to climate changes needs a thorough study of the hydrological cycle, resulting in improved climate projections for the continent.

The objectives of this study are to test the performance of the fifth-generation of the Canadian Regional Climate Model (CRCM5) in its simulation the summer (JJA) and winter (DJF) atmospheric water budget over Africa and to assess the potential added value of the model concerning seasonal mean and time variability. For these purposes each atmospheric variables is decomposed into large scales, resolved by CRCM5 and ERA-Interim driving reanalysis, and small scales, unresolved by the Reanalysis. The divergence of the vertically integrated horizontal moisture flux is alternatively represented as a sum of four interaction terms obtained from the spatially decomposed wind and humidity. The seasonal-mean divergence is also decomposed into stationary- and transient-eddy contribution terms, emphasizing the role of the circulation associated with the Saharan Heat Low (SHL). The PAV was associated with the seasonal-mean small-scale fields and with the unresolved divergence, and their variances.

Results show that the seasonal-mean water budget is dominated by the large scales, with small-scale contribution limited over the steep terrain and along the shore. The time-mean vertically integrated moisture flux divergence is controlled by the stationary-eddy component through large-scale self-interactions, while the transient-eddy component is present essentially in Inter-Tropical Discontinuity and in temperate latitudes. It was shown that unresolved divergence results mainly from interactions between small-scale wind and large-scale humidity and provides a smaller contribution than resolved divergence. Overall, PAV in seasonal-mean moisture divergence is topographically forced and partly due to resolved component (i.e. large-scale wind and humidity).

Finally, the climate variability of the atmospheric hydrological cycle is characterized by a dominance of small-scale contribution. The variance of the unresolved humidity flux divergence is greater than that of the resolved term. The dominant interaction terms are determined for the main geographical regions. Maximum standard deviation observed in the ITCZ, Indian Ocean, Central Atlantic and mid-latitudes suggests significant PAV with synoptic and convective origins for the variability.

Keywords: CRCM5, added value, scale decomposition, atmospheric water budget, moisture flux divergence, Africa

CHAPTER I

INTRODUCTION

The Earth's atmosphere exchanges energy, momentum and moisture with the ocean and the land, at global and local scales.

The water in the atmosphere, present in the form of vapour, cloud droplets and ice crystals, is a very important substance in the climate system. The three phases coexist, affecting the solar and terrestrial radiation transfers that depend on its radiative properties, and exchanging latent heat with the environment during its transformations. While the liquid water in the clouds reflects sunlight and decreases the surface temperatures, water vapour appears as the most abundant and very powerful greenhouse gas in the atmosphere. Transported by the general circulation, atmospheric water participates in the local radiative, energy and heat balance, and contributes to its spatial redistribution.

The tropics are the Earth's atmospheric engine, delivering the principal amount of latent heat of the planet, associated with meso-scale convection and cloud formations. Therefore, understanding the operating principles of this machine and the processes governing its variability is essential for the prediction of future changes in the climate, not only in tropical regions, but also over the globe. Nevertheless, climate change scenarios for Africa differ in provided estimation of projected precipitation, especially in arid and semi-arid regions. In the same time these are the regions that are most affected by climate extremes. Persistently dry and wet periods dramatically affect African economies, completely dependent on agriculture and water resources.

Periods of drought and flood impact on food security and health, leading in long time to desertification, famine, epidemics, human migration and death. Drought-prone areas, mainly the Sahel region of West Africa, Horn of Africa and southern Africa are extremely sensitive to time and space variability of the inter-tropical convergence zone (ITCZ), which defines the length of the rain season (IPCC 2007). For example in 2011 Somalia was hit of one of the worst humanitarian crises in the world today; currently, according to a study conducted by a group of nongovernmental organizations including CARE (Cooperative for Assistance and Relief Everywhere, www.care.org), 18 million people are at risk of a food crisis in the Sahel, including more than 1 million children at risk of severe malnutrition.

Hence, the motivation for the present study is that the elaboration of effective adaptation strategies must be based on thorough study of the hydrological cycle over Africa, considering of whole range of time and spatial scales, and the interaction between them, which is one of the most important characteristics of the atmospheric process over the continent. Our intention is to examine how well the fifth-generation Canadian Regional Climate Model (CRCM5), used for simulation of the atmospheric hydrological cycle, represents the synoptic and meso-scale contribution in the water vapour budget. The second reason for this study is to assess quantitatively the model ability to create meso-scales fields, which do not exist in the assimilated observations.

The coupling between the atmosphere and land surface is determinant for the water cycle in the tropics. Although the evaporative cooling restrains surface temperature increases, in absence of precipitations evapotranspiration (direct evaporation from the surfaces and evaporation of transpired water from plant leaves) can cause drought, crop failure and wildfires (Trenberth et al. 2003). Meynadier et al. (2010a) estimated the evapotranspiration in the Guinean region, which is characterized with weaker seasonal cycle of vegetation and with large rainfall amounts, larger than 1.5 mm/day all year long, while in semi-arid Sahelian region

evapotranspiration varied between zero during the dry season and 2 mm/day in August. In this region, where the soil depth is not as large, the precipitation's quantity was the main limiting factor to evaporation. The authors highlighted the dominant role of the moisture flux convergence in West Africa for the rainfall amount at regional scale. In contrast, in Sahel, the results suggested that almost all the cumulated rainfall was re-evaporated in atmosphere in annual mean. By examining the ratio of local evaporation versus externally advected evaporation, called recycling, Trenberth (1999a) estimated that, for 100 km scales, less than 20% of the annual precipitation comes from evaporation within a region. So, moisture transport is a crucial mechanism providing local atmospheric moistening. Relatively high annual values of recycling (>20%) occurred only in the subtropical high pressures, where evaporation is high and the advective moisture flux is small, and in convergence zones where, again, the advective moisture flux is small.

Globally, precipitation exceeds evaporation in equatorial inter-tropical convergence zone and in mid-latitudes. The precipitation mechanisms, trajectories and propagation speeds of the squall lines and other mesoscale rainfall systems over Sahel are influenced by the position and strength of the ITCZ in Africa. The northernmost extent of the ITCZ determines the amount of precipitations in this region, which is characterized with extreme interannual and decadal variability. Lebel et al. (1997) and Le Barbé and Lebel (1997) showed that dry years in Sahel are accompanied by more southward-located ITCZ, and result more from smaller number of rainy events than from reduced intensity of these events.

Over the entire globe and over a long period of time, evaporation is balanced by precipitation (Peixoto and Oort 1992). For a smaller area, however, the transport of moisture in the region is crucial and must be accounted, and for periods of time shorter than a month, changes in the total water vapour content (precipitable water) in the atmosphere should also be considered. Depending non-linearly on the temperature

through the Clausius-Clapeyron relation, atmospheric water content is generally higher in low latitudes and in warmer climate.

The evapotranspiration and precipitation are the coupling terms between the atmosphere and the terrestrial water cycles. This connection enables the assessment of the runoff and the surface storage directly from atmospheric variables, or on the basis of precipitation and evapotranspiration, the latter being obtained from the atmospheric water balance or deduced from other atmospheric quantities. In the absence of data for these fields, regional climate models (RCM) can be put to use to generate the missing information. RCMs add high-resolution information to data provided from Global Climate Models (GCM) and observations. Improved representation of topography and physical process is beneficial for the simulation of regional and local circulation, meteorological variables and their extremes. The more realistic fields provided by RCM are used for climate analyses and to force various regional impact models (Rummukainen 2010).

As precise long-term and high-density measurements of winds and precipitation are difficult to realize (Lawford et al. 2007), the available observations are often inaccurate and irregular in space and time. For the purpose of climate modelling, the available observational data are interpolated on a uniform grid. However, the interpolation can introduce errors in the gridded data, particularly over mountainous areas and along the coastlines due to the high spatial variability, height dependence of many meteorological variables and differences between real and model orography (Prömmel et al. 2010). As the large-scale data supplied from GCM or Reanalyses are used as boundary conditions to drive regional climate models over a limited area, and for verification of the RCM-output fields, the correct assimilation of the observations contributes significantly to model improvement. In contrary, if systematic errors introduced by the scarcity of observation and the poorly approximated parameterization of the physical processes in the driving data are transmitted to RCM,

they can affect the generated fine-scale features. For example, testing a new version RCA3.5 of the Rossby Centre model over Africa, forced by ERA-Interim boundary conditions for the period 1997-2007, Jones et al. (2009) have found that the simulated precipitation was systematically overestimated over the mountains. They explained it with excessive triggering of convection in these regions, but assume also that a portion of this overestimation could reflect deficiencies in the low-resolution Global Precipitation Climatology Model (GPCP), used for validation of the rainfall. So, the question of the accuracy of the observational data products used for model verification should also be taken into account.

The regional weather is considered to be the result of interaction between large-scale atmospheric circulation and regional physiographic details. This concept takes place in regional climate modelling trough the classical assumption that RCMs do not modify the large scales, transmitted as lateral boundary conditions or spectral nudging large-scale forcing, and that the regional scales are developed exclusively by the regional model (Laprise 2003, 2008). These small scales are referred to as added value (AV) of the RCM, as they are not resolved by low-resolution driving data. Following this concept, Bielli and Laprise (2006, 2007), Bresson and Laprise (2011), and Di Luca et al. (2011) have used the presence and magnitude of fine-scale variability to assess the potential of the Canadian Regional Climate Model (CRCM) to add value.

Under specific application of large-scale nudging and for some variables, the higher resolution could also improve intermediate scales common to both RCMs and GCMs, as showed by the experiments of Rockel et al. (2008), Feser (2006) and Feser et al. (2011). In such case the AV verification requires comparing of the commonly resolved scales with different observational products, to determine which one produces better performance. Using Reanalyses as driving data may simplify the evaluation of the RCM-simulated large scales, as the Reanalyses represent

assimilated observations with small systematic bias in their large scales (i.e. so-called "perfect boundary conditions", e.g. Prömmel et al. 2010). In spite of all this, the model validation is always affected by uncertainties in observed variables that should be taken into account.

Given the scarceness of fine-scale observations, it is difficult to objectively verify that the fine-scale details are reliable, i.e. if RCM improves or degrades GCM (or Reanalysis) statistics. That is why in this work we refer to the concept of a potential added value (PAV), as presented in Di Luca et al. (2011) and Bresson and Laprise (2011), according to which the presence of small scales indicates only the potential for eventual existence of AV, but is not a sufficient condition to state its real existence. Hereinafter, by the term added value, we will mean potential added value.

Castro et al. (2005) identified the surface boundary forcing as the dominant factor in generating of small-scale variability. Feser (2006), Feser et al. (2011), Di Luca et al. (2011) confirmed that RCM can add value, but usually mostly for variables influenced by regional specifics such as coastlines, complex topography, vegetation and soil characteristics or mesoscale dynamics. Other factors determining AV are the model parameterizations, domain size and horizontal resolution (Castro et al. 2005, Giorgi and Marinucci 1996), the nesting technique and lateral boundary conditions (Feser 2006, Colin et al. 2010, von Storch et al. 2000, Alexandru et al. 2009, Laprise 2008, Meynadier 2010a), simulated scales of motion and the season (Leduc et al. 2011, Bielli and Laprise 2006 and 2007, Bresson and Laprise 2011). As discussed by several authors, the AV is apparent mainly in the time variability and much less in the time-mean variables, and it is often larger in the summer season. In the regions with little small-scale physiographic forcing, generally little AV must be expected.

In recent years a comparison between various RCM, nested with the same Reanalysis data, has been adopted as a useful tool for evaluating and improving their performances. In the COordinated Regional climate Downscaling Experiment CORDEX (Giorgi et al. 2009) the limited-area models are run for a common region with lateral and surface boundary conditions coming from ERA-Interim Reanalysis (Dee et al. 2011, Uppala et al. 2008) for the period 1989-2008. These reanalysis have improved surface fluxes, global total column water vapour and hydrological cycle in the tropics compared to ERA-40 Reanalysis. However, Era-Interim still exceeds the GPCP estimated precipitation. In the CORDEX project Africa was chosen as first priority region, because of its vulnerability to climate changes affecting the atmosphere dynamics, precipitation patterns and rainfall variability. The consequences may be disastrous for the livelihood and health of the population. In this sense, within the CORDEX framework, our study tries to contribute to better understand of the African water cycle and its variability.

The knowledge of African weather systems requires phenomena at different scales to be considered. Several studies (Desbois et al. 1988, Redelsperger et al. 2002, Berry and Thorncroft 2005, Kiladis et al. 2006, Jury and Pathack 1991) suggest a relationship between the evolution and location of the mesoscale convection and the large-scale circulation. The complex multi-scale interaction reflects in spatio-temporal rainfall variability and calls for a scale-decomposition in its research. For this reason, and to detect the contribution of different wavebands in the added value, a scale decomposition of the terms of the water vapour budget into large and small scales will be carried out in the thesis. The scales will be separated by using DCT filter (Discrete Cosine Transform, Denis et al. 2002), and following a methodology for space decomposition, proposed by Bielli and Laprise (2006). The authors applied this methodology to the time-mean water vapour budget simulated with the CRCM for one winter month over North America, driven by NCEP-NCAR reanalysis. They focused on the vertically integrated divergence of the moisture flux and on its

nonlinear-interaction terms, working with three scale bands. Results showed added value resided mostly in the nonlinear interaction between large and small scales. The latter were forced by the topography for the wind and by the synoptic systems for the humidity. It was indicated that the small scales were confined in the stationary part of the time-mean water flux divergence, with very little contribution due to transient eddies.

In a sequel investigation for 25-year winter and summer seasons, Bielli and Laprise (2007) revealed the dominance of the intra-seasonal variance in the total variability and the leading role of the convectively-forced small scales during the summer in the added value over the North American continent. In winter season, the influence of the topography and ocean on the small-scale generation prevailed the convection. Bresson and Laprise (2011) applied the same methodology for investigation of the WVB over North America as simulated by CRCM-4.2 version, driven with Canadian Global Climate Model (CGCM). The statistics calculated for current and future winter and summer seasons confirmed the significant dominance of small-scale contribution in the added value of the summer time variability. The scale decomposition brought to the conclusion that for the humidity flux divergence, part of the large-scale variability was due to interactions involving small scales that are not resolved by low-resolution CGCM.

Bielli and Roca (2010) adapted the technique of decomposition to West African Monsoon, using NCEP/GFS operational analysis for the active monsoon period of 2006. Results showed dominating large scales (greater than 1400 km) in the seasonal mean precipitations and moisture flux divergence, except over the topography, where the scales smaller than 900 km had strong contribution. Precipitation was strongly correlated to moisture flux divergence below 800 hPa and in the layer 800-500 hPa via both large and small scales. Precipitation and evaporation were positively correlated over the ocean mainly through the large scales and over the northern part

of Sahel through the small scales. South of Sahel this correlation was negative and driven by large scale.

The purpose of our work is to test the performance of the fifth version of the CRCM in reproducing of the main features of the water vapour budget over Africa, and to assess the PAV of the model with regard of the seasonal mean water budget and its time-variability. The thesis is organized as follows. Chapter 2 describes the model simulation and data used in the thesis, as well as the scale-decomposition methodology. Chapter 3 presents a brief overview of the principal circulation systems in the domain. Chapter 4 focuses on the boreal summer (JJA) and winter (DJF) climatological-mean water budget, and on the scale interactions involved in the seasonal-mean moisture flux divergence. Time variability of the total and decomposed budget terms and of the interaction-components of the moisture divergence is addressed in Chapter 5. Finally, Chapter 6 summarizes the results and conclusions.

CHAPTER II

EXPERIMENTAL FRAMEWORK AND METHODOLOGY

2.1 The CRCM5 and Experimental configuration

The fifth-generation Canadian Regional Climate Model (CRCM5) is used in this study. The CRCM5 dynamical kernel and several physical parameterizations evolve from a limited-area version of the existing Global Environmental Multiscale (GEM) model, developed for Numerical Weather Prediction by the Meteorological Service of Canada (Côté et al. 1998a and b). GEM employs a semi-implicit semi-Lagrangian numerical scheme used for the integration of the fully elastic nonhydrostatic Euler equations (Yeh et al. 2002). GEM supports a variety of domain configurations: global uniform latitude-longitude, global stretched grid, and nested limited-area domain, all with optional rotation. A description of CRCM5 is presented in Zadra et al. (2008). The physical parameterisations of CRCM5 include the Kain-Fritsch deep and shallow convection scheme (1990), large-scale condensation scheme (Sundqvist et al. 1989), correlated-K radiation (Li and Barker 2005) and the Canadian Land-Surface Scheme CLASS3.5 (Verseghy 1991 and 2000, Verseghy et al. 1993) with 3 soil layers.

A 20-year simulation is run over Africa from Jan. 1st 1989 to Jan. 1st 2009. The horizontal coordinate system is uniform non-rotated latitude-longitude grid with grid spacing of 0.22° on 452 x 462 grid-point domain, using a 10-minute timestep. The experiment is performed with 56 hybrid terrain-following levels in the vertical, with a top at 10 hPa. The large-scale lateral boundary conditions in CRCM5 are

interpolated from reanalyses or global-model simulations through one-way nesting (Davies 1976) over a 10 grid-point sponge zone. An option for weakly nudging the large scales inside the domain also exists, but is not used for these simulations. The lateral boundary conditions are provided by ERA-Interim reanalysis with a resolution of 2°, available every 6 hours on 22 pressure levels (1000, 975, 950, 925, 900, 850, 800, 700, 600, 500, 400, 300, 250, 200, 150, 100, 70, 50, 30, 20, 15 and 10 hPa). The sea-surface temperature and sea-ice distribution are interpolated from the AMIP2 (Atmospheric Model Intercomparison Project v2) monthly mean values, analysed on 1°x1° grid. For this simulation the initial conditions for land-surface fields come from earlier CRCM5-simulation.

In the following, only the inner region of 392 x 402 grid points will be analysed. Later scale decomposition will be performed over a 388 x 388 grid-point square domain. Figure 2.1 shows the model topography over this domain. Subsequently all fields will be displayed on a sub-domain of 368 x 368 grid points, corresponding to about 9000 km x 9000 km. Model output is saved every 3h. The first 5 years are discarded as spin-up period and a 15-year period from 1994 to 2009 will be studied.

2.2 Methodology

The methodology applied in this study follows closely that of Bielli and Laprise (2006, 2007). The vertically integrated water budget in the atmosphere can be expressed (e.g. Peixoto and Oort 1992) as:

$$\partial_t \overline{q} = -\nabla \cdot \overline{\mathbf{F}} + E - P \qquad (1)$$

where q is the specific humidity, **F**=**V**q is horizontal moisture flux vector, E is the evapotranspiration rate, P is the precipitation rate, **V**=(u,v) is horizontal wind vector. The overbar represents vertical integration in pressure coordinate:

$$\overline{\psi} = \frac{1}{g}\int_{p_{top}}^{p_{sfc}} \psi \, dp = \frac{1}{g}\int_{p_{top}}^{p_0} \beta\psi \, dp \qquad (2)$$

Here $p_0 = 1013.3$ hPa and $p_{top} = 0$ hPa are used. The term β represents a mask to take into account for the topography (Boer 1982); it allows integration on pressure levels to be made only above the terrain, in spite of the same lower integration limit p_0.

The divergence of vertically integrated horizontal humidity flux is calculated as:

$$\nabla \cdot \overline{\mathbf{F}} = \frac{1}{r\cos\varphi}\left(\frac{\partial(\overline{uq})}{\partial\lambda} + \frac{\partial(\overline{vq}\cos\varphi)}{\partial\varphi}\right) \qquad (3)$$

with r the Earth radius, and (λ, φ) the geographical latitude and longitude. All the terms of water vapour budget are calculated in units of millimetres per day. The evapotranspiration is estimated by dividing the latent-heat flux by the latent heat of vaporization (L_v=2.5 10^6 J/kg).

2.2.1 Water budget calculations

The specific humidity q and the horizontal wind **V** at each archival time are interpolated from 56 terrain-following model levels on 23 pressure levels between 1000 hPa and 100 hPa: (1000, 975, 950, 925, 900, 875, 850, 825, 800, 775, 750, 725,

700, 650, 600, 550, 500, 400, 300, 250, 200, 150 and 100 hPa). This procedure is necessary to perform scale decomposition on quasi-horizontal surfaces. We note that 12 of these pressure levels are chosen below 700 hPa to provide a better vertical resolution in the boundary layer where atmospheric moisture is concentrated and where the Saharan Heat Low (see Chapter 3) is located. The moisture flux **F** is calculated, vertically integrated on pressure levels, and its divergence is computed using centred finite differences at each archival time. The specific humidity is also vertically integrated at each archival time. The water vapour tendency $\partial_t \overline{q}$ is evaluated as a finite difference between two archival times. Model-simulated cumulative precipitation is archived every 1 hour, while cumulative latent heat flux, and instantaneous values of specific humidity, horizontal wind and surface pressure are archived every 3 hours.

Figure 2.2 compares the averaged boreal summer (JJA) and boreal winter (DJF) vertically integrated moisture-flux divergence, evaluated from ERA-Interim Reanalysed (Fig. 2.2a, b) and CRCM5-simulated (Fig. 2.2c, d) data, as well as the CRCM5 field E-P (e and f). We note that the ERA-Interim data are available to us on pressure levels, with only 8 levels below 700 hPa compared to 12 for CRCM5, at 6-hourly interval rather than 3-hourly for CRCM5. The ERA-Interim winds and specific humidity were interpolated on the CRCM5 horizontal grid for easier comparison. As is well known and confirmed by the aforementioned studies of Bielli and Laprise, the monthly-mean moisture budget consists of a quasi equilibrium between E-P and the vertically integrated moisture-flux divergence $\nabla \cdot \overline{\mathbf{F}}$, with the precipitable water tendency about an order of magnitude smaller. Hence the difference E-P may be used as proxy for the correct vertically integrated moisture flux divergence, given that this quantity can only be calculated approximately with data that are time-sampled and interpolated on pressure levels. Figures 2.2c and 2.2e, and respectively Figs. 2.2d and 2.2f, show a generally good agreement between $\nabla \cdot \overline{\mathbf{F}}$

and E-P, with most differences located mainly in coastal zones and over the topography (refer to Fig. 2.1). As discussed by Bielli and Laprise (2006, 2007) and Meynadier et al. (2010b), the possible sources of this discrepancy could reside in time sampling errors due to the use of 3 hourly wind and humidity fields, interpolation from model to pressure levels, approximation of the divergence operator with finite differences, and coarse vertical resolution in lower troposphere. The figure also shows a relatively good overall agreement between $\nabla \cdot \overline{\mathbf{F}}$ in the CRCM5 simulation (Fig. 2.2c, d) and that calculated from ERA-Interim data (Fig. 2.2a, b). Some differences, arising from simulated dynamic fields, occur around 20°N in JJA and in equatorial Atlantic in DJF.

2.2.2 Spatial scale decomposition

Following Bielli and Roca (2010), each term X of the water budget, as well as horizontal wind components and specific humidity, are decomposed into two spatial scales and two time components. The spectral decomposition is performed on pressure levels, such that $X = X_L + X_S$, where X_L represents the large (planetary and synoptic) scales that are resolved by the Reanalysis fields as they are available to us. Over Africa these X_L scales are associated with the Inter Tropical Convergence Zone, subtropical Highs, monsoons, African Easterly Waves (AEW), Tropical Easterly Jet (TEJ) and with the mid-latitude weather systems. The smaller scales, noted as X_S, correspond to those that are only resolved by CRCM5; these are indicative of the potential added value (PAV) of the CRCM5 and represent the circulations associated with mesoscale convective systems, land-sea distribution and sharp topography.

Considering that the smallest features resolved by a numerical model range from a scale of the order of two grid-boxes as an absolute minimum (e.g. Laprise 2003) to one of the order of four or more grid boxes, as an effective minimum (e.g.

Feser et al. 2011, Pielke 1991, Grasso 2000), the effective resolution of the 2°-truncated Era-Interim Reanalysis resides around 880 km. Indeed, the spectra of the time fluctuation of the specific humidity and the zonal wind at 850 hPa over Africa for CRCM and ERA-Interim data for the month of July 2000. Figure 2.3 shows that the Reanalyses start to lose power around 900 km wavelength compared to CRCM5-simulated fields. For the time-mean spectra this wavelength is around 500 km (not shown). The separation between large and small scales is performed using a low-pass DCT filter with a gradual cut-off between 440 and 880 km to reduce the Gibbs' effects (Denis et al. 2002). Scales greater than 880 km are entirely kept in the large scales L, and scales smaller than 440 km are entirely kept for small scales S.

In addition, the vertically integrated moisture flux divergence field, which is a quadratic term, is calculated after the horizontal wind V=(u,v) and specific humidity q have been decomposed into their L and S components, following Bielli and Laprise (2006):

$$\nabla \cdot \overline{\mathbf{F}} = \nabla \cdot \overline{\mathbf{V}_L q_L} + \nabla \cdot \overline{\mathbf{V}_L q_S} + \nabla \cdot \overline{\mathbf{V}_S q_L} + \nabla \cdot \overline{\mathbf{V}_S q_S} \qquad (4)$$

This decomposition allows identifying the non-linear interactions between large- and small-scale wind and humidity fields.

Moreover, we define a Reanalysis-resolved divergence R, that involves interactions of large-scale wind with large-scale humidity, and Reanalysis–unresolved divergence U, involving at least one small-scale component that is not captured by the Reanalysis at 2° as it is available to us. Hence,

$$\nabla \cdot \overline{\mathbf{F}} = R + U \qquad (5a)$$

where

$$R = \nabla \cdot \overline{\mathbf{V}_L q_L} \tag{5b}$$

$$U = \nabla \cdot \overline{\mathbf{V}_L q_S} + \nabla \cdot \overline{\mathbf{V}_S q_L} + \nabla \cdot \overline{\mathbf{V}_S q_S} \tag{5c}$$

It is worth noting that the resolved and unresolved terms may contain both large (respectively noted R_L and U_L) and small scales (noted R_S and U_S), as their components involve large- and small-scale interactions. That is why the physical meaning of R and U is different from that of $(\nabla \cdot \bar{\mathbf{F}})_L$ and $(\nabla \cdot \bar{\mathbf{F}})_S$, which express the contribution of each scale in the total divergence. As consequence, the potential added value in atmospheric water vapour flux divergence can be expressed in terms of directly decomposed small-scale divergence PAV_S:

$$PAV_S \propto (\nabla \cdot \bar{\mathbf{F}})_S = R_S + U_S, \tag{6}$$

or in terms of unresolved divergence PAV_U:

$$PAV_U \propto U = U_L + U_S \tag{7}$$

The two approaches are not equivalent: although the unresolved small scales U_S contribute in both PAV_S and PAV_U, PAV_S is influenced also by the small-scale resolved divergence R_S, whereas unresolved divergence PAV_U is in part due to the large-scale unresolved divergence U_L. In summary

$$\begin{aligned}
&\nabla \cdot \bar{\mathbf{F}} = R + U = (\nabla \cdot \bar{\mathbf{F}})_L + (\nabla \cdot \bar{\mathbf{F}})_S \\
&R = \nabla \cdot \overline{\mathbf{V}_L q_L} = R_L + R_S \\
&U = \nabla \cdot \overline{\mathbf{V}_L q_S} + \nabla \cdot \overline{\mathbf{V}_S q_L} + \nabla \cdot \overline{\mathbf{V}_S q_S} = U_L + U_S \\
&(\nabla \cdot \bar{\mathbf{F}})_L = R_L + U_L \\
&PAV_S \propto (\nabla \cdot \bar{\mathbf{F}})_S = R_S + U_S \\
&PAV_U \propto U = U_L + U_S
\end{aligned} \tag{8}$$

These equations demonstrate that in principle (1) large-scale wind and humidity fields could participate in PAV_S through generated small scales R_S, and (2) regional model could add some value in the large scales of the moisture divergence through U_L. But as shown by Bielli and Laprise (2006), the interaction between large and small scales generates divergence with predominantly small scales, and self-interaction of large scales creates both large and small scales, with dominating domain-average large scales. From these remarks and Eq. 8 we deduce the following approximations:

$$\begin{aligned} &\nabla \cdot \overline{\mathbf{V}_L q_L} = R_L + R_S \text{ where } \left\{ |R_S| < |R_L| \right\} \\ &\nabla \cdot \overline{\mathbf{V}_S q_S} \approx 0 \\ &U_L \approx 0 \\ &PAV_U \approx U_S \approx \nabla \cdot \overline{\mathbf{V}_L q_S} + \nabla \cdot \overline{\mathbf{V}_S q_L} \end{aligned} \tag{9}$$

It will be verified later if these approximations remain valid for the African tropical climate.

2.2.3 Temporal decomposition and statistics

Besides decomposition in space, the water budget terms are decomposed in the time as:

$$X = [X] + X',$$

where $[X]$ denotes temporal mean and X' the time deviation.

Using the time decomposition of **V** and q, the time-mean vertically integrated water vapour divergence can be expressed as:

$$[\nabla \cdot \bar{\mathbf{F}}] = \nabla \cdot \overline{[\mathbf{V}][q]} + \nabla \cdot [\overline{\mathbf{V}'q'}] \tag{10}$$

The first term represents the stationary eddies contribution, dominated by topographic features and semi-permanent large-scale circulation, and the second – transient eddies contribution such as AEW, mid-latitude cyclones and convective disturbances.

Applying spatial and temporal decompositions, the large and small scales contribution to the time average can be identified as:

$$[X] = [X_L] + [X_S]$$

The study carried out with water budget fields for the summer (JJA) and winter (DJF) seasons during 15-year period. Let us denote the archive of the quantity X as $X_{j,y}$, where the subscript j refers to the archival time step within the season of year y.

The seasonal mean for the year y is defined as

$$[X]_y^J = \frac{1}{J}\sum_{j=1}^{J} X_{j,y} \tag{11a}$$

The seasonal climatological average is:

$$[X]^{Y,J} = \frac{1}{Y}\sum_{y=1}^{Y}[X]_y^J = \frac{1}{Y \cdot J}\sum_{y=1}^{Y}\sum_{j=1}^{J} X_{j,y} \tag{11b}$$

J is the total number of time steps within the season and Y=15 is the number of analysed years.

We define also the intra-seasonal climatological variance as

$$\sigma^2_{cis} = \frac{1}{Y \cdot J} \sum_{y=1}^{Y} \sum_{j=1}^{J} (X_{j,y} - [X]^J_y)^2, \tag{12a}$$

the interannual seasonal variance

$$\sigma^2_{cia} = \frac{1}{Y} \sum_{y=1}^{Y} ([X]^J_y - [X]^{J,Y})^2, \tag{12b}$$

and the total seasonal variance:

$$\sigma^2_c = \frac{1}{Y \cdot J} \sum_{y=1}^{Y} \sum_{j=1}^{J} (X_{j,y} - [X]^{J,Y})^2 \tag{12c}$$

Note that $\sigma^2_c = \sigma^2_{cis} + \sigma^2_{cia}$.

After combining of the time- and spatial-scale decomposition, we can represent the variance of the field X as:

$$\sigma^2(X) = \sigma^2(X_L) + \sigma^2(X_S) + \mathrm{cov}(X_L, X_S),$$

where $\mathrm{cov}(X_L, X_S) = 2[\, X'_L X'_S \,]$.

Similarly, the temporal variance of the moisture divergence (i.e. $X = \nabla \cdot \overline{\mathbf{F}}$) is a sum of the temporal variances of the resolved scales R, unresolved scales U and the covariance between U and R scales:

$$\sigma^2(\nabla \cdot \overline{\mathbf{F}}) = \sigma^2((\nabla \cdot \overline{\mathbf{F}})_R) + \sigma^2((\nabla \cdot \overline{\mathbf{F}})_U) + \mathrm{cov}(\nabla \cdot \overline{F}_R, \nabla \cdot \overline{\mathbf{F}}_U)$$

Concerning moisture divergence, we will note for short

$$\sigma_L^2 = \sigma^2((\nabla \cdot \overline{\mathbf{F}})_L); \qquad \sigma_S^2 = \sigma^2((\nabla \cdot \overline{\mathbf{F}})_S) + \mathrm{cov}((\nabla \cdot \overline{\mathbf{F}}_L, (\nabla \cdot \overline{\mathbf{F}}_S) \tag{13a}$$

$$\sigma_R^2 = \sigma^2((\nabla \cdot \overline{\mathbf{F}})_R); \qquad \sigma_U^2 = \sigma^2((\nabla \cdot \overline{\mathbf{F}})_U) + \mathrm{cov}((\nabla \cdot \overline{\mathbf{F}}_R, (\nabla \cdot \overline{\mathbf{F}}_U), \tag{13b}$$

so that in summary the time-variance of the moisture divergence can be expressed by the two ways:

$$\sigma^2(\nabla \cdot \overline{\mathbf{F}}) = \sigma_L^2 + \sigma_S^2 \tag{14a}$$

$$\sigma^2(\nabla \cdot \overline{\mathbf{F}}) = \sigma_R^2 + \sigma_U^2 \tag{14b}$$

The potential added value of the CRCM5 in the time variability for $\nabla \cdot \overline{\mathbf{F}}$ contains in the sums σ_S^2 and σ_U^2. These sums will be considered respectively as small-scale variance and unresolved variance.

CHAPTER III

THERMODYNAMIC FACTORS AND SYSTEMS ASSOCIATED WITH ATMOSPHERIC WATER TRANSPORT OVER AFRICA

Here we present a brief description of the African topography and atmospheric circulation. This will be useful for further validation of the simulated water vapour budget and for identification of the physical processes associated with the spatial-scale interactions.

The average elevation of the North Africa is relatively low (~400 m). The main orographic systems here are Atlas (31°N, 7°W), Hoggar (23°N, 5°E) and Tibesti mountains (18°N, 19°E), Fouta Djalon highlands (11°N, 12°W), Joss plateau (9°N, 9°E), Cameroon mountains (4°N, 10°E), Darfur (15°N, 24°E) and Ethiopian highlands. Higher eastern and southern plateaus (mean elevation of 1000m) are bounded by rugged mountain chains that give rise to strong water flux gradients and topographic forcing (Fig 2.1).

The global circulation over Africa is determined to a large extent by the strength and position of the Subtropical Highs in the Atlantic and Indian oceans, and the trade winds that converge into ITCZ over the Atlantic. The ITCZ represents the ascending branch of the Hadley cell, characterized by deep convection and maximum of precipitation. In West Africa the main precipitation band is situated around 10°N in boreal summer and 0° in winter (Thorncroft at al. 2011). Near the continent the land-sea temperature contrast results in southwesterly monsoon circulation in West Africa in June, July, and August (JJA), whereas over the tropical Indian Ocean it is

the Indian monsoon that controls the wind circulation. The West African monsoon flux transports moisture from the Gulf of Guinea towards the Sahel. Over the continent the monsoon-induced precipitation represents a sort of continuation of the ITCZ precipitation, determining a maximum of the moist static energy. Northward the region with maximum potential temperature around 20°-22°N defines the Saharan Heat Low (SHL), characterized by strong dry convection up to 600 hPa, and northerly return flow at 800-600 hPa associated with the divergence at the Heat Low top (Meynadier et al. 2010b, Zhang et al. 2008). As discussed in Zhang et al. (2008), Peyrillé and Lafore (2007), the winds at this level actually penetrate the monsoon rain band, inhibit the deep convection and suppress northward migration of precipitation.

The elements of the large-scale dynamics in West Africa are shown in Fig. 3.1. The low-level circulation consists of a southwesterly monsoon flow to the south and northeasterly dry Harmattan flow to the north. Their confluence corresponds to the Inter-Tropical Discontinuity (ITD) representing the northernmost penetration of the monsoon flux into the continent. Peyrillé et al. (2007) and Thorncroft et al. (2011) localize it in August at around 20°N, near the centre of the SHL. In Fig. 3.1a, which represents the simulated by CRCM5 mean pressure and surface winds in boreal summer, ITD is situated between 12°N and 18°N. The ITD is marked by many topographically-forced convective cells and westward propagating Mesoscale Convective systems (MCS) (Redelsperger et al. 2002, Desbois et al. 1998). Investigating intraseasonal variability in the West African monsoon, Sultan et al. (2003) found that westward propagating convection and rainfall from the Eastern Africa to the tropical Atlantic are modulated at intraseasonal timescales of 10-25, 25-60 and 38 days.

The cool waters in the Gulf of Guinea and the warm waters of the Mediterranean Sea contribute to enhance the moisture advection over the Sahelian region (15°N-20°N) (Peyrillé et al. 2007, Peyrillé and Lafore 2007). The rainfall and

the moisture convergence over the eastern part of the Sahel are influenced by variations in the Indian Ocean's SST (Palmer 1986, Mohino et al. 2012). Radiative forcing, aerosols and soil moisture (Peyrillé et al. 2007, Chauvin et al. 2005) also affect the African climate.

The mid- and high-level large-scale dynamics characterizing the West African climate includes the African Easterly Jet (AEJ) at around 600-700 hPa, related with him African Easterly Waves (AEW) and evolved from Indian monsoon Tropical easterly Jet (TEJ) located at about 200 hPa. Their position according to the CRCM5 simulation is shown in Figs. 3.1a and 3.1b. AEJ results from the meridional thermal contrast between SHL and relatively cold Gulf of Guinea and from the reversal of this gradient near 700-600 hPa (Thorncroft and Blackburn, 1999). In boreal summer the jet is weakened at its edges by both barotropic and baroclinic conversions that give rise to AEW (Bupree 1972), with length scales between 2000 km and 5000 km and initiated by convection over the region between 10°E and 30°E. Two main modes of disturbances at 850 hPa over Sahel and at 600 hPa equatorward of 15°N (Thorncroft and Hodges 2001, Berry and Thorncroft 2005) are with periods of respectively 6-9 days and 3-5 days (Diedhiou et al. 1999).

During the austral summer (DJF), the shift of the ITCZ into Southern Hemisphere leads to more active atmospheric processes over South African sub-continent. The ITCZ position in this season is determined by the interaction between three surface airstreams: southeast trades originating over the Indian Ocean, northeasterly flow originating from the winter Indian monsoon, and westerly current originating over the South Atlantic and moving eastward across the Congo basin to converge with the two easterly airstreams (cf. Fig. 3.2c, d). Cold Benguela and warm Agulhas and Mozambique oceanic currents have an effect on the moisture content and shore rainfall amounts on the southwest and southeast coast of Africa (Jury et al. 1993, Crimp et al. 1998, Shilington et al 2006). Precipitation is also influenced by

perturbations in temperate westerlies, coupled to tropical lows over southern Angola and Namibia, known as tropical-temperate troughs (Todd et al. 2004, Vigaud et al. 2007, Jury and Pathack 1991, McHugh and Rogers 2001).

It is useful to look how successfully the regional model represents the key features of the surface circulation over Africa. To indicate the differences between the reanalysis and CRCM5-simulated circulation, Fig. 3.2 represents the JJA (first row) and DJF (second row) seasonal-mean specific humidity and wind vectors at 1000 hPa and the mean sea-level pressure for 15 years (1994-2008) from CRCM5 (Fig. 3.2a, c) and ERA-Interim (Fig. 3.2b, d). The model reproduces the mean features of the average distribution of pressure, surface winds and moisture, but exhibits a southward bias in SHL position (15°N -20°N unlike to 20°N -25°N in ERA-Interim), resulting in less northward penetration of the monsoon winds. The band of maximum meridional gradients of the specific humidity in Sahel (Fig. 3.2a) is narrower and located too far south, consistently with the location of the Heat Low in the simulation. In consequence, ITD is displaced from 20°N in ERA-Interim to around 15°N in CRCM5. The sea-level pressure and atmospheric moisture are lower than that in Reanalysis for the Central Africa in JJA and for the southern sub-continent in DJF. In DJF this causes a northerly advection of dry air up to equator in the centre of the continent and stronger southwesterly winds in North Congo basin (Fig. 3.2c). Some of the reasons for the differences between the regional model and the driving reanalysis according Hernández-Díaz et al. (1012) may be due to discrepancies in CRCM5-simulated 2m-temperatures (cold bias in Sahara), convective parameterization scheme and surface albedo, possibly exacerbated by the use of a very large African domain without large-scale spectral nudging. On the other hand, the fields in ERA-Interim is also possible to be imperfect, since all the Reanalyses are a product of data assimilation and do not represent the real atmospheric state. The disparities between Reanalysis and model dynamics will further influence the

intensity and position of the simulated meridional and vertical circulation, the precipitation field and moisture flux divergence in the region (shown later).

CHAPTER IV

SEASONAL-MEAN WATER VAPOUR BUDGET OVER AFRICA

In this and next section we will present the seasonal-mean budget for boreal summer (JJA) and boreal winter (DJF) averaged for 15 years (1994-2008). The mean moisture flux divergence will be decomposed into stationary and transient terms and into four interaction terms, the large- and small-scale components of which will be displayed. The humidity-divergence PAV will be estimated following the mentioned above different approaches.

4.1 Boreal Summer (JJA)

4.1.1 Seasonal mean water vapour budget

The surface circulation in JJA can be described by 15-year average 1000 hPa winds and sea-level pressure, which in Fig. 4.1 are superimposed to seasonal mean water vapour budget terms. ITD is marked by surface wind confluence around 15°N in the southern part of the Saharan Low. The surface winds are illustrative for the low-levels moisture flux advection. All the terms of the budget at Sahara and South Africa are nearly zero. In boreal summer the African atmosphere is feeding with moisture from Mediterranean Sea, South Indian Ocean and indirectly from Northern Atlantic. Easterly atmospheric moisture flux over West Africa is consistent with the presence of AEJ. The South Atlantic influence is limited to the WAM region, where

the column moisture flux converges with easterly flow more southward than at the surface (around 8°N).

Figure 4.1a reveals Subtropical Highs over Atlantic and Indian oceans as main sources of evapotranspiration, with a more modest contribution from and equatorial forests. The areas with reduced evaporation along the west coast in Southern Atlantic are consistent with the low SST of Benguela cold current (10°S-30°S) and with the maximum intensity of the Atlantic cold tongue in August (Peyrillé at al. 2007). The northern limit of evapotranspiration over the continent is determined by the northernmost extension of the tropical rainfall belt (Fig. 4.1b). The time mean water vapour tendency is negligible (note the scale multiplied by 100 in Fig. 4.1c). Its sign reveals the northward excursion of the ITCZ during the boreal summer and decreasing atmosphere water vapour in Southern hemisphere. The strongest decrease is related with the rapidly cooling SST in equatorial Atlantic Ocean, whereas the band with largest accumulating moisture is just south of the ITD around 12°N, with a maximum located in Sudan near Khartoum. Given the weakness of this term, the main atmospheric water balance is between precipitation, evaporation and moisture flux divergence. The later (Fig. 4.1d) compensates the evaporation over the tropical oceans, while in the ITCZ and over east coast of Madagascar the convergence almost completely balances the precipitation, revealing its dominant role in rainfall generation. The maximum convergence near the Guinean shore, according to Thorncroft et al. (2011), has a frictional origin arising from winds deceleration as they move from the ocean to the continent.

In Fig. 4.2 JJA-averaged precipitation from CRCM5 (Fig. 4.2a) is compared with 1° GPCP1dd gridded rainfall (Fig. 4.2b) and CRU 0.5° (Climate Research Unit, at 0.5° spatial resolution) gridded observations over the land (Fig. 4.2d), which are interpolated to CRCM-horizontal grid. As GPCP1dd dataset is available from 1998 to

2008 year, the precipitation from CRCM5 and from CRU gridded analysis only for this period is presented in the figure. All the datasets show rainfall peaks in Guinea Highlands, Cameroon Mountains, Central African tropical forest and Ethiopian Highlands. The simulated rain belt in CRCM5 is narrower, resulting in a dry bias in Sahel around 13°N, in the north of the Gulf of Guinea and in Congo basin (0°-5°S) (Fig. 4.2c). At the same time, precipitation amounts in the Indian Ocean and Madagascar are with 2-10 mm/day higher than observed. The intensity in Guinea and Cameroon regions is overestimated with up to 15 mm/day compared to GPCP. The CRCM5-simulated quantities are similar to those obtained by Sylla et al. (2010a). As noted by Hernández-Díaz et al. (2012), the model-simulated precipitation may be more realistic than the gridded datasets for Madagascar: according to the Historical and Meteorological Data Center (HMDC) (http://docs.lib.noaa.gov/rescue/data_rescue_madagascar.html), most of the mountainous east coast of Madagascar, wet for much of the year, have an annual rainfall over 2000 mm, which is missed by the coarse mesh GPCP analysis. The probable reliability of the CRCM5-rainfall is confirmed by the reduced differences, when compared with a higher resolution dataset, such as CRU 0.5° precipitation (Fig. 4.2e).

The small-scale contribution, which corresponds to the PAV of CRCM5, was found to be very limited in the seasonal mean water budget terms. The small-scale features are concentrated along the coast and the steep topography (Fig. 4.3e-h). For the precipitation (Fig. 4.3f), small scales are coherent with the regions of maximum rainfall amounts over Guinea, Cameroon, Ethiopia and Madagascar that show the role of topographically forced convection. The precipitable water tendency (Fig. 4.3g) is weak, but its small scales in Sahel show an interesting signal: they are collocated with the southern fringe of the Saharan heat low around 13°N, exposing the role of the ITD and imbedded convective systems in the moisture transport.

The vertically integrated specific humidity and moisture fluxes calculated with CRCM5 and ERA-Interim data (Fig. 4.4a, b) show that climatological patterns are overall well reproduced by CRCM5. By comparing with Fig. 4.2c, it can be seen that the differences in precipitation are closely related to differences in precipitable water content (Fig. 4.4c): in the regions with model rainfall deficit/excess the vertically integrated specific humidity is lower/higher than in Reanalyses. Moisture flux across the Guinean coast in the Reanalysis (Fig. 4.4b) appears to be a crucial condition for enhanced rainfall generation in the north part of the Gulf of Guinea; thus dynamic, but also topographic coastal forcing contributes to the precipitation in this region.

Interestingly, we found that, according to CRCM5, precipitation higher than 2 mm/day in the WAM region is triggered when the water content in the atmosphere reaches values between 40-44 kg/m^2 (Fig. 4.4a). The same threshold, deduced from the GPCP precipitation and ERA-Interim vertically integrated specific humidity (Fig. 4.4b), is between 34 kg/m^2 and 40 kg/m^2.

4.1.2 Mean divergence due to stationary and transient eddies

The decomposition of the time-mean vertically integrated moisture fluxes and their divergence into stationary- and transient-eddy contribution (Eq. 10) is shown in Fig. 4.5. Sea-level pressure is outlined as well. The stationary-eddy contribution $\nabla \cdot \overline{[\mathbf{V}][q]}$ in the time-mean moisture divergence (Fig. 4.5b) arises from seasonal-mean circulation and seasonal mean moisture. The maximum convergence reflects the ascending branch of the Hadley meridional cell and fits well with the maximum intensity of the tropical rain belt, while the maximum divergence corresponds to descending branches of the Hadley cell and dry regions.

The transient-eddy contribution $\nabla \cdot [\overline{\mathbf{V}'q'}]$ (Fig. 4.5b) is somewhat weaker but not negligible. It represents the effect of mid-latitude synoptic activity, easterly waves and mesoscale convection. Its maximum convergence is found in Sahel, South African coastline and middle latitudes. In many areas its sign opposes that of the stationary-eddy component. For example, over the Sahel between 15°N and 20°N, transient-eddy convergence completely cancels stationary-eddy divergence, resulting in vanishingly small total moisture convergence in Sahel. Transient-eddy divergence between 10°N and 15°N reduces the convergence due to the stationary-eddy component; as a result the band of total moisture convergence (Fig. 4.5a) is narrower than that due to the stationary-eddy component. The decomposition of the vertically integrated moisture divergence into stationary- and transient-eddy components has served identifying a dipole structure in Sahel, which is not clear from the time-mean divergence pattern.

It is interesting to note the observed relationship between the stationary and transient components of the mean vertically integrated moisture divergence patterns and the layer-decomposed moisture flux divergence in the monsoon layer (1000-800 hPa) and AEJ-layer (800-500 hPa), presented in Fig. 4 in Bielli and Roca (2010). It would appear that the stationary-eddy moisture convergence between 0°-15°N over the continent is generated in the lower and middle atmosphere, while the transient-eddy moisture convergence in the SHL is related to the low-level dry convection. The latter is compensated by middle-level stationary divergence over the top of the SHL, situated at nearly 800 hPa. The northerly return flow at these levels (800-550 hPa) converges with AEJ at 10°N -15°N, partly resulting in downward motion and transient divergence at the surface. As discussed in Meynadier et al. (2010b) and Thorncroft et al. (2011), such structure leads to inhibited moist convection and explains the suppressed rainfall north of 13°N, compared to GPCP data (see Fig.

4.2b). This proposed explanation agrees with the main features of the SHL shallow circulation described by Zhang et al. (2008).

An additional decomposition of the two divergence components into their large and small scales (Fig. 4.6) shows a dominant large-scale contribution. Around 14°N latitudes, the most pronounced small-scale feature is the band of transient divergence in ITD.

4.1.3 Scale-interaction terms of the moisture flux divergence

In attempt to further reveal the processes responsible for the moisture flux divergence, the latter is decomposed as sum of four components arising from interactions between scale-decomposed wind and humidity fields. Figures 4.7 and 4.8 show these components for the stationary- and transient-eddy components of the vertically integrated moisture divergence in JJA. Figure 4.7 demonstrates that the mean divergence owing to the stationary eddies, arises primarily due to seasonal-mean large-scale wind interacting with seasonal-mean large-scale humidity; the component resulting from small-scale wind and large-scale humidity, however, also plays an important role. All the terms exhibit larger amplitudes over the main highlands, mountain chains or coastal gradients. The transient-eddy component shown in Fig. 4.8 is mostly dominated by interactions between large-scale components; all the terms arising from small-scale wind and/or small-scale humidity have overall very limited contribution, even if their amplitudes are locally comparable to those of the dominant term $[\overline{\mathbf{V}_L' q_L'}]$. With structures concentrated along the ITD, these terms can be considered as illustration of the interaction between large-scale AEW (represented as humidity and wind perturbations in AEJ) and MCS (referred to transient small scales in our decomposition), that is one of the main

subjects of investigation over Africa in the recent years (e.g. Kiladis and Weickmann 1997, Diedhiou et al. 1999, Berry and Thorncroft 2005).

Figure 4.9 displays the four scale-interaction terms of the total JJA moisture flux divergence. As for the stationary- and transient-eddy components, the dominant term of this decomposition is $\nabla \cdot \overline{\mathbf{V}_L q_L}$, which is expected given the dominant large-scale structure of atmospheric fields in the tropics. This term is treated also as resolved divergence R (Eq. 5b). The main small-scale contribution $\nabla \cdot \overline{\mathbf{V}_S q_L}$, related with large-scale humidity transported from small-scale winds over Africa, tends to reduce $\nabla \cdot \overline{\mathbf{V}_L q_L}$ nearly everywhere over the land except in East Madagascar. Maximum values are reached over the steep terrain and along the eastern African coast. The term involving self-interaction of small scales is very weak.

Figure 4.10 shows the two dominant scale-interaction terms, $\nabla \cdot \overline{\mathbf{V}_L q_L}$ and $\nabla \cdot \overline{\mathbf{V}_S q_L}$, decomposed into L and S scales. The large-scale wind and humidity interaction projects strongly in both large and small scales (Fig. 4.10a, b), whereas small-scale wind and large-scale moisture field projects mostly in small scales (Fig. 4.10c, d). This is coherent with the study of Bielli and Laprise (2006) over North America that showed that interaction between large and small scales projects dominantly into small scales. The correlation coefficient between large scales of these terms and their counterparts, calculated from the ERA-Interim Reanalysis, is 0.85 for $\nabla \cdot \overline{\mathbf{V}_L q_L}$ and 0.60 for $\nabla \cdot \overline{\mathbf{V}_S q_L}$. The other two terms involving small-scale humidity create weaker small-scale contribution and very limited large-scale projection (not shown). So, we can conclude that part of the small-scale mean divergence in Fig. 4.3 is created by large-scale humidity through its interaction with large- and small-scale winds. We note that almost everywhere these two components nearly cancel each other. Respectively, a small part of large-scale divergence at the same figure is due to small-scale wind and large-scale humidity.

As it was earlier discussed, the PAV conception assumes large scales in the regional model to be similar to those of the driving Reanalysis. The large scales of the mean atmospheric moisture divergence, computed by CRCM5 (Fig. 4.11a) and ERA-Interim data (Fig. 4.11b) exhibit high spatial correlation with value of 86%. While the divergence patterns are overall quite similar, the amplitudes differ up to 4-6 mm/day in Sahel, Guinean region, Gulf of Guinea, Ethiopia and along the Indian Ocean Coast (Fig. 4.11c). In part the disparities may be due to imperfection of the reanalysis fields, as well as to different spatial and time resolution of the model and the Reanalysis, mentioned in Chapter 2. So, it is not evident which of them represents more realistically large scales. We accept, however, ERA-Interim as reference, and subsequently it can be expected the added value of the moisture divergence in the indicated areas to be misrepresented. Elsewhere, especially in Atlantic Ocean, the PAV can be evaluated trustworthy from small-scale features generated in CRCM5-simulated fields.

As expected from the decomposition of the moisture flux divergence into four interaction terms, the sum of all terms that involve small scales, i.e. the unresolved moisture divergence U (Fig. 4.12b), is smaller than the resolved component R (Fig. 4.12a). The major contribution in the unresolved small scales (Fig. 4.12f) comes from $\nabla \cdot \overline{\mathbf{V}_S q_L}$, and to a lesser degree from interaction between large-scale wind and small-scale humidity, represented in Fig. 4.9. Unresolved large scales have limited contribution compared to that of the unresolved small scales and mainly arise also from the component $\nabla \cdot \overline{\mathbf{V}_S q_L}$. The fields of U_L and U_S are almost identical to those in Figs. 4.10c and 4.10d, consistently with the aforementioned negligible contribution of $\nabla \cdot \overline{\mathbf{V}_L q_S}$ and $\nabla \cdot \overline{\mathbf{V}_S q_S}$ to the large and small scales of the unresolved divergence. The small presence of U_L, which was hypothesized in Eqs. 9 and confirmed for African continent here, determines the quasi-equivalence between PAV_U and U_S, represented essentially by the term $\nabla \cdot \overline{\mathbf{V}_S q_L}$. The opposite small-scale projections of

R and U, according to Eqs. 6 and 7, lead to PAV_S being weaker than PAV_U. The latter is seen by comparing the small-scale divergence in Fig. 4.3h with the unresolved one in Fig. 4.12b. It is worth noting that the generation of unresolved large-scale moisture divergence suggests the idea that CRCM5's added value is not only in small scales, but also in large-scale mean divergence.

4.2 Boreal winter (DJF)

4.2.1 Seasonal mean water vapour budget

Water budget terms, as well as sea-level pressure in boreal winter are presented in Fig. 4.13. In austral summer the Azores High is installed over the northernmost part of the African continent, inducing the dry northeasterly Harmattan winds in low levels that propagate as far south as 10°N in West Africa and reach the equator in the centre of the continent, determining the position of ITD at these latitudes in DJF. The confluence of the fluxes originating from Indian and Atlantic Oceans forms the meridional South-African branch of the ITCZ (0°-10°S). The surface atmospheric circulation favours maximum moisture accumulation in Central South Africa and northeast of Madagascar, where the northwest monsoon converge with easterlies from the central Indian Ocean. Moisture flux convergence (Fig. 4.13d) is strongly correlated with precipitation (Fig. 4.13b), and the moisture flux divergence balances the evaporation (Fig. 4.13a) over the ocean. In austral summer the latter is weaker over the south-hemisphere water basins than in JJA, but great over the warm Indian Ocean, where the precipitation is also larger in this season. The precipitable water tendency (Fig. 4.13c) reflects southward shifting of the tropical rain maximum during the boreal winter, but it remains insignificant compared to other water vapour budget terms.

The spatial decomposition of the water budget terms confirms that in DJF, as in JJA, large scales (planetary and synoptic) dominate the water budget (Fig. 4.14a-d), whereas small-scale features are weak and related with topography, convection and synoptic activity (Fig. 4.14e-h). The small scales of precipitation modulate large-scale field over Madagascar, Mozambique, Southern DRC, Cameroon and Angola. Mean precipitable water tendency shows fine-scale structures in the South Hemisphere, both over the continent and the oceans, as well as in ITD. Small-scale contribution to mean moisture flux divergence in DJF is less than in austral winter.

DJF seasonal mean CRCM5 precipitation for 1998-2008 (Fig. 4.15a) is verified by comparison with that in the GPCP1dd (Fig. 4.15b) and CRU 0.5° (Fig. 4.15d) gridded observations. The simulated maximum rainfall located in Mozambique, Zambia, Gabon (8-12 mm/day) and in Madagascar (25-30 mm/day), coincides well with the observations. In spite of this, the model is considerably wetter in Northern and Eastern coast of Madagascar and in the Indian Ocean, and much dryer in the equatorial Atlantic and Central Africa (Fig. 4.15c). As argued by Hernández-Díaz et al. (2012), real precipitation may be underestimated in the gridded datasets for some regions such as the Gabon and Madagascar regions, since according to the Historical and Meteorological Data Center (HMDC) for Madagascar, lowlands along the southern and western coasts of Madagascar receive 400 to 800 mm of annual rainfall and central plateau receives 1000 to 1500 mm, which amounts are mostly collected between November and March. The east coast, as well as a small region in the northwest, have an annual rainfall over 2000 mm. The authors note that CRCM5 and TRMM reproduced this pattern while the coarser mesh GPCP analysis missed it. The apparent smaller bias with respect to higher-resolution precipitation in CRU 0.5° (Fig. 4.15e) also implies that reduced CRCM5-rainfall in northern Congo and along the northern border of Zimbabwe is likely realistic.

The disparity between the modelled and the observed precipitation may be related with some discrepancies in the precipitable water field and vertically integrated moisture flux in CRCM5 (Fig. 4.16a) and ERA-Interim (Fig. 4.16b). Over the Indian Ocean the moisture flow in the model turns to eastward and increases at 10°S, providing moisture in the oceanic regions north of Madagascar. On the contrary, reanalysis flow is directed towards the African continent. Moreover, in ERA-Interim the moisture flux from the Indian Ocean reaches the Atlantic equatorial coast of the continent, transporting humidity between 5°N and 5°S. In CRCM5, these latitudes are affected by much weaker humidity supply from the Indian Ocean, and consequently, by lower precipitable water content over the northern part of Democratic Republic of Congo (DRC) (Fig. 4.16c). Furthermore, in the northern part of the Gulf of Guinea (10°W -10°E; 0°-5°N) the model produces stronger flow, as well as weaker meridional flux convergence at 5N. As consequence, in these parts of the domain, the integrated moisture flux convergence from ERA-Interim is replaced by moisture divergence in CRCM5, as is seen in Figs. 2.2b and 2.2d, and as a consequence by suppressed precipitation. The column-integrated humidity flux reveals also the Indian Ocean as the main source of humidity for Southern Africa, and the North Atlantic for Northern Africa.

Total moisture advection coming from the Southern Atlantic is limited to most western coastal zones, while at the surface it penetrates up to Rift Valley as monsoon-like circulation (the wind streamlines in Fig. 4.13). Therefore, it can be concluded that the role of the South Atlantic as moisture source is confined in the low troposphere. We note that according to Fig. 4.15(a, c) and Fig. 4.16(a, b), precipitable water values of 36-40 kg/m^2 in CRCM5, and of 40-44 kg/m^2 in ERA-Interim/GPCP are observed in the regions with precipitation of 2 mm/day, situated in the ITD-zone between 10°W and 25°E.

4.2.2 Mean divergence due to stationary and transient eddies

The stationary- and transient-eddy components of the DJF-mean vertically integrated moisture flow and its divergence are shown in Fig. 4.17. As in JJA, stationary component prevails, particularly over the oceans. Higher synoptic activity in Mediterranean Sea during this season determines dominant role of the transient-eddy contribution in that region. The transient divergence has opposite sign, but weaker values almost everywhere, compared to stationary one, such that the stationary-eddy contribution represents the main part of the total divergence.

The low-pressure area over central equatorial Africa evolves from thermal reasons (not shown) and seems to have similar dynamic features to those of the SHL during boreal summer. Indeed, some additional examinations suggest transient convergence associated with low-level wind confluence, overlapped by stationary divergence above 800 hPa.

Large scales dominate both stationary- and transient-mean divergences (Fig. 4.18, second row), except over the topography and in the coastal zones, where small-scale contribution (Fig. 4.18, third row) is almost as important as the large-scale part.

4.2.3 Scale-interaction terms of the moisture flux divergence

Figure 4.19 shows that in DJF the contribution of each of the four scale-interaction terms in the stationary eddy divergence resembles their JJA-contribution (cf. Fig. 4.7). While mixed small- and large-scale terms are weaker during boreal winter, the main term $\nabla \cdot \overline{[V_L][q_L]}$ exhibits slightly enhanced amplitudes. The fine-scale structures are concentrated over the steep terrain and near the continent in the ocean, which is clearly seen from the pattern of the most important small-scale-

containing component $\nabla \cdot \overline{[\mathbf{V}_S][q_L]}$. Unlike to stationary eddy divergence, all four transient mean divergence components (Fig. 4.20) are smaller in the considered season. Moreover, it seems that the effects of the term $\nabla \cdot \overline{[\mathbf{V}'_L][q'_S]}$ weakly prevail over the effects involving small-scale winds, which is different regarding stationary mean divergence.

The total mean DJF moisture divergence resulting from interactions between large- and small-scale wind and humidity is shown in Fig. 4.21. As in boreal summer, the moisture divergence arises mainly by the terms $\nabla \cdot \overline{\mathbf{V}_L q_L}$ and $\nabla \cdot \overline{\mathbf{V}_S q_L}$. The contribution of the component involving small-scale wind and large-scale humidity is slightly weaker in austral summer with respect to their JJA extremes (Fig. 4.9). The topographic forcing acts stronger on small-scale winds than on small-scale humidity. Actually, there is small-scale forcing over the oceans too, well visible for one-year monthly averaged small-scale interaction terms (not shown), but it is cancelled during the time averaging and therefore is not seen in 15-year seasonal means.

The four interaction terms, decomposed additionally in L and S scales, reveal substantial contribution in small scales due to large-scale humidity interacting with both large- and small-scale winds. Large-scale divergence is almost fully produced by the interplay between large-scale winds and large-scale humidity (Fig. 4.22a). The main unresolved term producing large scales is $\nabla \cdot \overline{\mathbf{V}_S q_L}$. Inspection of the analogous decomposed terms, calculated with ERA-Interim data reveals lower spatial correlation for the large scales than in JJA: 80% for $(\nabla \cdot \overline{\mathbf{V}_L q_L})_L$ and 46% for $(\nabla \cdot \overline{\mathbf{V}_S q_L})_L$, The spatial correlation coefficient for the large scales of the total moisture divergence between CRCM5 and driving Reanalysis in DJF is about 0.79. These components, as well as the difference between them, are displayed in Fig. 4.23. Whereas the variables exhibit similar patterns, CRCM5 simulates weak divergence rather than strong convergence in Atlantic ITCZ, as well as increased convergence in

Madagascar and eastern part of Southern Africa, and reduced divergence in the Southern Atlantic and between 10°N and 15°N over the land. Taking the large-scale moisture divergence in ERA-Interim as a base despite its deficiencies, an element of uncertainty for the PAV in these regions might be deduced.

Figure 4.24 presents resolved (R) and unresolved (U) moisture divergence components and their projections into large- and small-scale components in boreal winter. Over complex topography the small scales of both R and U (Fig. 4.24e, f) have amplitudes up to 100-115 mm/day, representing roughly 2 to 4 times higher quantities than corresponding large-scale components (Fig. 4.24c, d). On the other hand, like for the boreal summer, the opposite fine-scale contribution results in PAV_U larger than PAV_S.

CHAPTER V

INTRASEASONAL CLIMATOLOGICAL VARIABILITY OF THE WATER VAPOUR BUDGET OVER AFRICA

In the following two sections we will look at the intraseasonal climatological variability of the total and of the scale-decomposed water vapour budget for JJA and DJF (1994-2008). The standard deviation of each of the four scale-interaction terms of the vertically integrated water-flux divergence will be calculated. The ability of the CRCM5 to provide valuable information on the temporal evolution of the hydrological cycle will be assessed using the variability of the unresolved component of the humidity divergence.

5.1 Boreal summer (JJA)

5.1.1 Time variability of the water budget terms

Temporal variability of the atmospheric water vapour budget is related to seasonal evolution and interannual changes in the mentioned above key thermodynamic factors in the continent. Small shifts in the ITCZ position during boreal summer can affect considerably the atmospheric water fields and local rates of evapotranspiration and precipitation, causing considerable consequences for the health and economics in the Sahelian region.

Figure 5.1a displays the transient-eddy climatological standard deviation σ_c (Eq. 12c), the interannual climatological standard deviation σ_{cia} (Eq. 12b) and the

intraseasonal climatological standard deviation σ_{cis} (Eq. 12a) of the atmospheric humidity divergence in JJA. The term σ_c is large in the areas with great seasonal mean convergence (Guinean coast, Cameroon, Ethiopia, eastern coast of Kenya and Madagascar) as well as poleward of ±30° latitudes, where is the maximum of the wind variability. In contrast, in areas with steady wind circulation and/or low column humidity, such as the northeastern periphery of the St. Helena anticyclone, arid and semi-arid regions of Sahara and Southern Africa, the variability of the JJA moisture flux divergence during the 15 studied years is lower than 8 mm/day.

Intraseasonal standard deviation (STD) is nearly identical to σ_c, with maximum magnitudes around 60-70 mm/day, i.e. three to six times larger than the amplitude of the correspondent seasonal mean moisture flux divergence. The maxima over the oceans are due to the passing low pressure systems, while the continental pattern in boreal summer reveals variability associated with variations in the intensity of the AEJ, TEJ and the monsoon flux (e.g., Sultan et al. 2003).

Bielli and Laprise (2007) have shown that interannual variability σ_{cia} of the divergence of atmospheric moisture flux over North America accounts for less than 5% of total standard deviation. We found that over Africa this contribution is also weak. Figure 5.1a suggests a very limited contribution of the interannual variability σ_{cia}. Averaged over the analyzed domain, its contribution is around 3% of the total standard deviation. The component σ_{cia} is coupled with the interannual fluctuations of SST, vegetation cover and soil moisture, which control year-to-year variations of the ITCZ position, monsoon circulation and humidity fluxes over the continent.

An examination of the other three water budget terms over Africa confirms that the intra-seasonal climatological standard deviation always dominates in the total one. That is why in the following only the intra-seasonal variability will be presented.

The atmospheric water cycle components, except evapotranspiration, are characterized by variability higher than their mean, with maximum values in the ITCZ, ITD and Indian Ocean and over the mid-latitude storm tracks (Fig. 5.2). For evaporation, the variability results generally from changes in the surface vegetation properties over the continent and is related to SST and wind fluctuations over the oceans. The maximum variability of precipitation (Fig. 5.2b) is collocated with the mean precipitation maxima, while the regions around 14°N and 5°S over the continent and along 3°N over the Atlantic Ocean are marked by steep STD gradients. Over Sahel the north extension of the STD band is limited by the northernmost penetration of the moist monsoon winds. Contrary to the case in North America, where the rainfall exhibits relatively small STD (Bresson and Laprise, 2011), in Africa this field demonstrates significant time fluctuations, comparable in fact to that of the moisture flux divergence (Fig. 5.2d), which is the most variable term. The water vapour tendency (Fig. 5.2c) shows strong temporal variability in spite of its negligible time-mean magnitudes. Maximum $\partial_t \overline{q}$ variability over the continent is consistent with the position of the highest seasonal means observed in ITD, i.e. north of the monsoon-generated peaks in precipitation and in $\nabla \cdot \overline{\mathbf{F}}$.

5.1.2 Variability of the scale-decomposed water budget terms

Figure 5.3 shows intraseasonal variance of the large-scale (Fig. 5.3a) and small-scale (Fig. 5.3b) components of the water vapour budget, and the covariance between large and small scales (Fig. 5.3c). Unlike the time-mean water cycle, the contribution of the small scales in the temporal variability dominates in nearly all budget terms but evapotranspiration; the intraseasonal variability of the latter is small and mainly in large scales.

Variance of the both large and small scales of precipitation is highest over the East Atlantic Ocean and Guinea Gulf Coast. The enhanced variability over the continent is observed in the areas characterized with 3-5 day and 6-9 day periodicity (corresponding to the AEJ activity at 5°N-10°N and 15°N-20°N, described by Diedhiou et al. 1999), 15-day cycle (WAM circulation, Sultan et al. 2003) and 25-60-day time scales (referred to Madden-Julian oscillation, Maloney and Shaman 2008). Small scales are the most variable in the zones with maximum mean precipitation. Their contribution between 5°N and 10°N is overall 3-4 times stronger than the large-scale variability, due to the important role of continental convection in their generation. The variability of the meso-scale precipitation is determined by the number and intensity of the squall lines (Redelsperger et al. 2002) and the organized convective systems between 10°-15°N (Mathon et al. 2002a and b).

In the southern subcontinent, a narrow band of enhanced variance of small-scale rainfall along the east coast (Fig. 5.3b, second panel) can be considered as illustration of the convection developed over the warm Mozambique and Agulhas currents, as described by Jury et al. (1993).

The water vapour tendency shows large small-scale variability near the east coast of the Tanzania, Kenya, Somalia and Madagascar, west from 15°W in the tropical Atlantic, along the shore of Yemen as well as in Central Sahel. The areas with minimum large- and small-scale variability, found between 20°N -30°N and 5°S-25°S latitudes, are more restricted for the small scales. The patterns of the large-scale fluctuations of $\partial_t \bar{q}$ and $\nabla \cdot \bar{\mathbf{F}}$ are very similar, and southward of 35°S they dominate over the corresponding small scales. Fine-scale moisture divergence proved to be the component with the greatest variability; it exhibits enhanced fluctuations in regions of strongest precipitation anomalies, with extremes in the WAM-region and near the NE coast of Madagascar.

The covariance between large and small scales of the precipitation, $\partial_t \bar{q}$ and $\nabla \cdot \bar{\mathbf{F}}$ as a whole is substantial (Fig. 5.3c), especially in the Atlantic Ocean near Guinea, where it contributes greatly to the regional PAV. In contrary, the Gulf of Guinea, Sahel, and mountain terrains of East Africa are marked by negative covariance, implying that small scales contribute to reduce the contribution of large scales there.

5.1.3 Temporal variability of the decomposed moisture flux divergence

The high variance in the small scales of the water budget suggests significant PAV for all its components but evaporation. Concerning variability of the non-linear water vapour divergence, an alternative approach can be applied for its added value assessment. In this approach PAV is associated with the unresolved variance σ_U^2, defined as the variance of the unresolved moisture divergence plus the covariance between the resolved and unresolved divergence terms (see Eq. 13b). Figures 5.4a and 5.4b represent the resolved and unresolved contributions to the intraseasonal variability. Unresolved intraseasonal variability overall is dominant, especially over the Indian Ocean, ITCZ and central Atlantic. The negative values are due to the covariance term that reduces σ_U^2 over the mountains, contributing to the PAV. Resolved variance σ_R^2 prevails over the high topography, while in the zones with minimum amplitudes nearly equal contribution of resolved and unresolved parts is observed. The variance patterns and magnitudes of the two terms are quite similar to these of the large- and small-scale variance defined by Eq. 13a (Fig. 5.4c, d), but with more fine-scale structures located over the mountains. Thus, the scale-interaction approach gives advantage to see the areas with dominating orographical origin of the variability. The differences $(\sigma_L^2 - \sigma_R^2)$ and $(\sigma_S^2 - \sigma_U^2)$, shown in (Fig. 5.4e, f), illustrate that over the mountains, in the ITCZ and poleward of 30° latitude, resolved

variability dominates over the σ^2_L. In the same regions unresolved contribution is weaker than its small-scale counterpart because of the reducing role of the covariance $\mathrm{cov}_{R,U}(\nabla \cdot \overline{\mathbf{F}})$ in σ^2_U, implying higher PAV in the moisture divergence variability in terms of small-scale contribution σ^2_S than in terms of small-scale interactions σ^2_U.

To examine the contribution of the different scales to generation of the moisture divergence variability, intraseasonal standard deviation of the four scale-interaction terms is represented in Fig. 5.5. While in the climatologically mean divergence the terms involving small scales are negligible over the oceans (Fig. 4.9), their STD are significant everywhere and comparable to that of the term with large-scale wind and humidity $\sigma_{cis}(\nabla \cdot \overline{\mathbf{V}_L q_L})$. The component $\sigma_{cis}(\nabla \cdot \overline{\mathbf{V}_L q_S})$ dominates overall in the domain and has maximum over the oceans, reaching 25-30 mm/day over the east coast of Madagascar. The other mixed-scale interaction term $\sigma_{cis}(\nabla \cdot \overline{\mathbf{V}_S q_L})$ possesses also significant variability in the Indian Ocean, but its contribution is most considerable in the ITCZ, with highest STD (50 mm/day) near the Guinean coast, where the specific humidity exhibits its maximum amount. For the same reason the term with large-scale humidity and synoptic-scale wind (Fig. 5,5a) is well represented too, only that its maximum (30-35 mm/day) is more in the ocean. The variability arising from self-interactions of the small-scale wind and specific humidity is in general weaker (Fig. 5,5d); a notable exception though is in the Sahel where its magnitude is similar to the 3 other contributions. We note the high similarity between its pattern and $\sigma^2_{cis}((\partial_t \overline{q})_S)$ (cf. Fig. 5.3), which could be interpreted as dominance of the q_S over $\mathbf{V}_S$ perturbations in variability generation. Furthermore the figure indicates more variability over the oceans for the terms involving small-scale moisture, and over both the oceans and continent for the terms with small-scale wind, confirming the synoptic origin of the small-scale moisture and topographical origin of the small-scale wind, as noted by Bresson and Laprise (2011) for North America.

It is of interest that over tropical North Africa the two terms containing large-scale humidity have maximum variability in the zone of tropical rainfall, south of the AEJ core (10°N), whereas the two divergence terms including small-scale humidity are more variables in the ITD latitudes (13°N), collocated with the northern vicinity of the jet. Thus, in Sahel the term $\sigma_{cis}(\nabla \cdot \overline{\mathbf{V}_L q_S})$ could be interpreted as variability created from interaction of the large-scale AEJ with the humidity embedded into the regional small-scale and mesoscale convective formations. The term $\sigma_{cis}(\nabla \cdot \overline{\mathbf{V}_S q_L})$ results from the large-scale humidity affected by local wind perturbations, while the component $\sigma_{cis}(\nabla \cdot \overline{\mathbf{V}_S q_S})$ represents variations generated only by the small scales.

In summary, the large small-scale variability in the water balance terms, excluding evapotranspiration, testifies to considerable PAV in boreal summer. Greatest PAV is concentrated in the ITCZ, ITD and in the Indian Ocean west of 55°E, between 0°-30°S. The variance of the small-scale moisture divergence is large also over the Central Atlantic. In these regions high resolution would be expected to improve the climate statistics. Unresolved variability arises from mixed scale-interaction terms and dominates the variance of the resolved moisture divergence.

5.2 Boreal winter (DJF)

The shifting of the ITCZ in the Southern Hemisphere during boreal winter sets enhanced atmospheric activity in Southern African subcontinent where higher surface water temperature in DJF favours tropical cyclogenesis and enhanced moisture supply, stronger convection and rainfall in the Eastern part of the Southern Africa (Jury and Pathack 1991, Jury et al. 1993). A tropical-temperate troughs and cut-off lows appears as dominating rain-producing synoptic type over South Africa, Madagascar and Southwest Indian Ocean in this season. The rainfall time-variability

in austral summer is characterized by multiple time scales, some of them on the order of 15-20 days, 2-3 years, 6 years, 10-12 years and 20 years (see review of Mason and Jury 1997).

5.2.1 Time variability of the water budget terms

The relationship between total seasonal, interannual and intra-seasonal STD of the vertically integrated humidity divergence for the 15 boreal winter seasons between 1994 and 2008 in this simulation is presented in Fig. 5.1b. Climatological seasonal variability σ_c is again dominated by intraseasonal standard deviation σ_{cis}. The both exhibit larger values than in JJA in the Southern Hemisphere, with maximum amplitudes of 60-65 mm/day at the northwestern coast of Madagascar. Large magnitudes are present also in Southern Indian Ocean, eastern coast of Southern Africa and along the track of the mid-latitude westerly disturbances. In the Northern Hemisphere, the zone with low STD over Sahara is larger, located more equatorward and with lower variability compared to boreal summer.

As in the boreal summer, the contribution of the interannual STD σ_{cia} is small and represents overall around 3.5% of the total domain averaged variability. Despite of this, its pattern allows to identify the SST-anomalies, the passing tropical storms in Indian Ocean and the moisture input from the tropical Atlantic between 5°S and 15°S (surface winds in Fig. 3.1), among the main sources of interannual variability. Changes in frequency, duration and strength of the key synoptic systems also contribute to the interannual fluctuation in the seasonal mean humidity divergence. Moreover, the coupling between warm Indian Ocean currents and atmospheric humidity transport in austral summer is stronger than in JJA season.

The seasonal STD of the precipitation, evapotranspiration, water vapour tendency and moisture flux divergence are shown in Fig. 5.6. Their variability is greater over the Indian Ocean than over the Atlantic Ocean, both in tropical and middle latitudes. As in JJA, standard deviation exceeds the seasonal mean for all terms excepting evaporation, that is the term with the lower variability. Compared to boreal summer, evapotranspiration STD (Fig. 5.6a) is larger over the oceans in Northern Hemisphere and over the continent in the Southern Hemisphere. The amplitudes of precipitation variability (Fig. 5.6b) are slightly lower than in JJA, but the maximum always occurs where the mean precipitation is higher. Over the continent, the variations in the ITCZ position and associated deep convection reflect in variations in the local rainfall amounts. According to Jury at al. (1993) and Crimp et al. (1998), convective clouds and rainfall distribution along the coastline of Mozambique and South Africa are affected by fluctuations in the strength and SST of the Agulhas current (27°S-40°S) and Mozambique current. Rainfall variability in central Indian Ocean arises from anomalies in accumulated precipitable water and in moisture divergence, as suggests the comparison of patterns between the different terms. North Atlantic and Mediterranean Sea precipitations are influenced by increased frontal activity during the boreal winter.

The STD patterns of the water vapour tendency and moisture flux divergence are fairly correlated (Fig. 5.6c, d), revealing key role of the humidity transport in intraseasonal deviation of precipitable water. Enhanced variability over Southern East Africa and Southern Indian Ocean suggests a connection with the tropical-temperate troughs, appearing as major mechanism of meridional moisture transport in this area (Todd et al. 2004). Higher variability over the Atlantic in Southern Hemisphere in DJF is due to larger amounts of moisture, embedded in the trade-wind circulation over warmer surface water. Quasi-permanent northeasterly winds and low humidity results in low STD in Sahara.

5.2.2 Variability of the scale-decomposed water budget terms

Figure 5.7 presents the large-scale (a) and small-scale (b) contribution in the intraseasonal variability of the water vapour budget, as well as the covariance between the large and small scales (c). It can be seen that for all the terms the DJF variability over the continent in southern/northern hemisphere is increased/weaken compared to that in JJA. Large scales dominate the variance of evaporation, whereas the weak small-scale presence is mainly along the coastline and the ITCZ. For all other water budget terms the variability of the small-scale components prevails in the total transient variance. Seasonal fluctuations in precipitation, both for large and small scales, are strongly related with ITCZ position, SST and atmospheric activity over the oceans. Their maximum in the east of Madagascar agrees well with the larger rainfall in the region of tropical cyclogenesis at 5°-15°S, 55°-70°E as identified by Jury and Pathack (1991). The authors have detected also zonal propagating transient convective systems with period of 15-20 days in the 10°-20°S band, which coincides with the high variability of the small-scale precipitation in Fig. 5.7(b, second panel). Convective forcing leads to prevailing of the small-scale variations over the continent and in Indian Ocean. The negative values in northeastern corner of the domain are due to large negative covariance between large and small scales.

In boreal winter, as in the boreal summer, the climatological variances of the water vapour tendency $\partial_t \overline{q}$ and moisture flux divergence $\nabla \cdot \overline{\mathbf{F}}$ exhibit analogous large-scale patterns, with greater magnitudes for the moisture divergence. In this season, the regions with low synoptic-scale seasonal perturbations in moisture divergence and in specific humidity tendency over Sahara are larger and shifted equatorward compared to the boreal summer. The small-scale contribution dominates everywhere in both fields and is largest in the South Indian Ocean, in the Atlantic westward of 10°W and in the temperate latitudes of Southern Hemisphere. Fine-scale

moisture divergence exhibits greater variations than in JJA nearly everywhere in Southern Hemisphere. The main maximum in the Indian Ocean is moved to south and is notably expanded between 10°S and 40°S, compared to austral winter, but the peak is always over Madagascar.

Positive covariance between large- and small-scale precipitation, moisture divergence and precipitable water tendency, notably in Indian Ocean and south of 30°S (Fig. 5.7c), indicates joint evolution of the synoptic systems and the embedded in them small-scale convection. Areas with high small-scale variability are surrounded by strips of negative covariance.

5.2.3 Temporal variability of the decomposed moisture flux divergence

Figures 5.8a and 5.8b display the resolved and unresolved contributions of the water vapour divergence into the intra-seasonal variability. The maxima are situated in the southern hemisphere, consistently with ITCZ location in DJF. Unresolved variance σ_U^2 dominates in both summer and winter hemispheres, except over the high topography, where the variance of the resolved divergence tends to be stronger. Over the regions with low variability, σ_R^2 and σ_U^2 have almost same contribution. We note that compared to JJA, both unresolved and resolved variances are increased over the continent south of the equator, but the fine-scale features in their patterns are less present in this season. On the contrary, over Sahara the small structures appear more clearly than in boreal summer. This implies that the stationary topographic forcing dominates where the other sources of anomalies, such as convection and large-scale activity, are reduced. In general, its contribution in the generation of transient variability remains limited. The situation in boreal winter over Sahara and South Africa (cf. Fig. 5.4) supports this assumption. As for the PAV in the moisture flux

variability, it is slightly better represented by the variance of the small-scale part σ_S^2 than of the unresolved divergence σ_U^2.

Figure 5.9 illustrates the DJF standard deviation of the interaction terms of the moisture divergence. Among the components contributing in unresolved variability, $\sigma_{cis}(\nabla \cdot \overline{\mathbf{V}_L q_S})$ and $\sigma_{cis}(\nabla \cdot \overline{\mathbf{V}_S q_L})$ are dominating. The resolved component (Fig. 5.9a) also exhibits significant magnitude, especially in the areas with typically disturbances in large-scale circulation and over the topography. In the temperate latitudes and in the Indian Ocean it amplifies the divergence anomalies, caused by the large-scale winds transporting small-scale humidity. Divergence variability in the Indian Ocean evolves in general from interactions involving large-scale wind and/or humidity, with domination of the $\sigma_{cis}(\nabla \cdot \overline{\mathbf{V}_S q_L})$ over and northeast of Madagascar. We recall that this region coincides with the track-zone of the tropical depressions, as mentioned in Jury and Pathack (1991), which explains its augmented intraseasonal variability. Thus, enhanced cyclogenesis makes this component dominant for Indian Ocean, contrary to the leading role of $\sigma_{cis}(\nabla \cdot \overline{\mathbf{V}_L q_S})$ during the austral winter. It is interesting to look at the fine-scale structures in the ocean south of Mozambique Channel, present in the components with small-scale wind. They might be related to convection generated by convergent moisture flows along the tropical-temperate troughs, as the region is one of preferred locations for their formation (Van den Heever et al. 1997).

In ITCZ the variability arises essentially from the contribution of $\sigma_{cis}(\nabla \cdot \overline{\mathbf{V}_S q_L})$. A pattern comparison shows this term as the most closely related with the rainfall variability displayed in Fig. 5.6, suggesting that tropical convection is fundamentally controlled by small-scale wind perturbations combining with the large-scale humidity field. Increased variability in the Atlantic Ocean comes essentially from the mixed-scale parts, with dominating interaction of the large-scale

wind and small-scale humidity. The influence of the orographic features is the least on the interactions between $\mathbf{V}_L$ and q_S. Also, it appears that a relationship exists between the low STD at 10°-35°S near the coast and the small-scale wind (Fig. 5.9c, d), as well as between the equatorial Atlantic minimum and the large-scale circulation (Fig. 5.9a, b).

It can be generalized that in DJF the PAV over Africa is stronger over the Southern Hemisphere, where it is increased in respect to JJA. On the contrary, in the Northern Hemisphere it is lower compared to boreal summer. The small-scale variability results from convective and synoptic activity both over the ocean and the continent. Topographical forcing also generates transient variability, but with limited contribution.

CONCLUSIONS

Africa is one of the continents most affected by climate extremes. The adaptation of its population and economy to climate changes requires different scenarios based on researches of the humidity transport and rainfall variability to be examined. The present study describes the summer and winter climatology of the atmospheric water cycle over Africa from 1994 to 2008, as simulated by the fifth-generation Canadian Regional Climate Model (CRCM5), driven by ERA-Interim Reanalysis data. The purpose of the thesis was firstly, to test the CRCM5's skill in producing the main features of the regional circulation and atmospheric water budget over Africa. Secondly, it aimed to assess the potential added value (PAV) of the model concerning seasonal mean and time variability of the water budget terms.

The basic approach was to decompose each atmospheric field into large scales, resolved by both the model and the driving Reanalysis, and small scales unresolved by the Reanalysis. The divergence of the vertically integrated horizontal moisture flux was alternatively represented as sum of four interaction terms obtained from the spatially decomposed wind and humidity. These terms were consequently recomposed into resolved and unresolved divergence terms. The seasonal mean divergence was also decomposed into stationary- and transient-eddy contributions, highlighting the role of the main weather systems in the African continent. The PAV was associated with the seasonal mean small-scale fields and with the unresolved divergence, and their variances. PAV assessment was based on the importance of the small-scale contribution relative to that of the large scales. The relevance of the simulated large scales was checked for the precipitation and moisture flux convergence, and it was confirmed that CRCM5 reproduces reasonably the large-scale structures of the driving Reanalyses and of the GPCP analysis of observed

precipitation. Climatological statistics of the simulated balance of the water vapour was linked to the characteristics of the atmospheric circulation, such as reproduced by the model. Some systematic errors in the CRCM5 simulation were also detected, such as insufficient northward penetration of the West African Monsoon (WAM) flux and associated rain band, and wider, southward-displaced African Easterly Jet (AEJ) in boreal summer. Both the summer and winter seasons exhibited overestimated precipitation in the tropical mountains and in the Indian Ocean. These discrepancies seem to originate from the simulated higher temperatures and deeper low-pressure systems over the Sahel and Congo.

In Chapter 4 we described the seasonal-mean water vapour budget over Africa. Results revealed a main balance, taking place between evapotranspiration, precipitation and vertically integrated moisture flux divergence. The rainfall amounts over the Indian Ocean, Madagascar, Cameroon highlands, and in JJA near the Guinea Coast, were overestimated, whereas a dry bias was simulated over the Gulf of Guinea, the northern part of Democratic Republic of Congo and in Sahel during the boreal summer. The applied spatial decomposition showed a large-scale domination in the seasonal-mean water budget. The small-scale contribution (respectively PAV), most present in the moisture divergence, was found to be very limited and related to topographic features. Precipitable water tendency, despite of its very small time-mean magnitude, seems to be the variable to which small-scale structures were most connected with the Inter-Tropical Discontinuity (ITD) position in Sahel. Further it was demonstrated that time-mean vertically integrated moisture divergence was controlled by its stationary component, especially over the ocean basins and Inter-Tropical Convergence Zone (ITCZ). Transient-eddy mean divergence was present on the whole in ITD and in temperate latitudes, associated with the larger number of the passing transient synoptic and convective systems there. A substantial fine-scale presence was noted in the southern edge of the Saharan Heat Low (SHL), in both stationary and transient-eddy divergence terms.

Our analysis, focused on the four scale-interaction terms of the seasonal mean humidity flux divergence, indicated dominance of the component related to large scales of both wind and humidity (i.e. resolved moisture divergence). Small scales were usually located over the steep terrain and along the shore, affecting predominantly the interaction terms involving large-scale humidity. It was found that the PAV associated to directly decomposed small scales of the mean moisture divergence (i.e. PAV_S) was weaker, compared to that associated to unresolved term (i.e. PAV_U). The latter exhibited strong topographic forcing and resulted mainly from non-linear interactions between q_L and V_S. This fact supports the conclusion of Bielli and Roca (2010), obtained for the active monsoon period of 2006, about the generation of small-scale divergence mainly by small-scale and meso-scale dynamics rather than by small-scale humidity. In our results this also appears to be the case for a whole continent and for both summer and winter seasons.

In Africa the interplay between the wind and humidity of synoptic scales appears able to produce moisture divergence at both large and small scales, while the large- and small-scale mixed terms generally produce small scales. The main small-scale term producing relatively significant synoptic scales was $\nabla \cdot \overline{V_S q_L}$. It was therefore concluded that a great part of the small-scale mean divergence is generated by large-scale humidity interacting with large- and small-scale winds. CRCM5 added also some value in the large scales of the moisture divergence via the term $\nabla \cdot \overline{V_S q_L}$.

The simulated seasonal variability of the atmospheric hydrological cycle, examined in Chapter 5, demonstrated a strong dependence on the ITCZ position, SST, tropical cyclogenesis in the Indian Ocean and synoptic-scale wave activity in the tropical midlevel atmosphere (such as AEW) and in the temperate latitudes. It was found that the climatological standard deviation exceeds the seasonal average for all terms of water vapour budget. The total variability was dominated by the

intraseasonal variance, whereas the interannual component accounted for around 3% of the total domain-averaged variability.

Over North America, Bresson and Laprise (2011) have noted during the winter significant, but overall smaller contribution of the small-scale variance compared to that of the large-scales, for all water budget terms except evaporation. It is worth noting that over Africa the small-scale variability overall dominated in both summer and winter hemispheres, which makes the African water cycle differ from that in the middle latitudes. For each hemisphere during its summer season, the variability of the small-scale water budget terms was enhanced over the continent, where it reinforced the large-scale variations controlled by the seasonal position of the ITCZ. In the winter hemisphere, the large variability of the small scales was concentrated over the oceans. Large small-scale contribution suggests significant PAV, located essentially in the ITCZ (near the Guinean Coast in JJA) and in the Indian Ocean (around Madagascar in DJF), and slightly lower PAV in mid-latitudes and over the Central Atlantic Ocean. High PAV over the Indian Ocean and the Central Atlantic in the Southern Hemisphere was noted in the both seasons, but was more important in the austral summer. Analysed areas with maximum variability implied that the small-scale transient variability have arisen from both convective and synoptic activities. Synoptic contribution prevailed over the oceans, and the convective forcing was dominant over the continent and in the summer hemisphere. The role of the topography in the generation of transient variability was limited because of its stationary nature. Its contribution emerged in the interaction terms of the moisture divergence and dominated the areas with low variability, typically observed in winter, when the thermal convection and the large-scale activity are reduced.

The fine-scale moisture divergence was the water budget component with highest variability. Unlike the seasonal-mean, it was dominated by the unresolved component, which pattern was analogous to that of the small-scale variability.

Nevertheless, the unresolved variance was slightly weaker in magnitude and represented finer structures of topographic origin. The resolved and unresolved components had comparable contribution in the regions with low temporal anomalies, while the variability of the resolved divergence was stronger over sharp topography. The PAV in the variability of the moisture flux divergence in winter hemisphere was located over the oceans and was much larger during the austral than during the boreal winter. In summer hemisphere, PAV was increased in ITCZ, as well as in the Central Atlantic Ocean throughout southern hemisphere summer.

The applied spatial scale decomposition of the wind and humidity allowed to associate each geographical region with a given dominating scale-interaction process, and to hypothesize the origin of the small-scale wind and humidity in the region. Whereas the mean interaction terms involving small scales were negligible over the oceans, their variability in these areas was quite significant. The inspection of the standard deviations of the four moisture divergence terms showed that the small-scale variability was governed by the components with mixed large and small scales of the wind and the humidity. In both seasons the term $\sigma_{cis}(\nabla \cdot \overline{\mathbf{V}_L q_S})$ exhibited oceanic maxima near the shore in the Indian Ocean, far from the coast in the Southern Atlantic and south of 30°S; the component $\sigma_{cis}(\nabla \cdot \overline{\mathbf{V}_S q_L})$ was dominating in ITCZ. Over the South Indian Ocean the main contribution in the variability arose from the interplay between the large-scale wind and the small-scale moisture in JJA, and between the small-scale wind and large-scale humidity in DJF, consistently with the enhanced tropical cyclogenesis in austral summer (we remind that according the employed spatial decomposition, atmospheric systems with sizes between 450 km and 900 km, such as the tropical storms, are partly represented into both large and small scales). The divergence generated by self-interactions of small-scale wind and humidity had very weak variability.

The results indicated also that intra-seasonal standard deviation of the moisture divergence containing large-scale moisture or small-scale wind was most influenced by the topography. Enhanced variability over the oceans for the terms involving small-scale moisture, and over both the oceans and continent for the terms with small-scale wind, confirms the predominant synoptic origin of the small-scale moisture and topographical origin of the small-scale wind over Africa, similarly to the case over North America (Bresson and Laprise 2011).

In summary, CRCM5 succeeded in representing the main features of the atmospheric water cycle over Africa. The seasonal-mean water budget and its variability were in good correspondence with the simulated thermodynamic properties of the African climate. The differences with the equivalent fields of ERA-Interim driving reanalysis result from some shortcomings of the tropical circulation in the model. The spatially decomposed components of the vertically integrated moisture divergence identified the function of the WAM, SHL and Indian Ocean. The role of the synoptic-scale wave disturbances and Mesoscale Convective Systems (MCS), which appear as principal large- and small-scale features in ITD, was clearly detected in the spatially decomposed components of the time-mean transient-eddy divergence. The PAV in the variability of precipitation, moisture divergence and specific humidity tendency was difficult to verify objectively. Nevertheless, further improvements in CRCM5 dynamics and scale-interaction investigations are necessary to better understand the mechanisms determining relationship between the moisture divergence and the main features of the circulation over the tropical Africa. The dependence of the PAV on the different time and horizontal resolution and on the choice of the number and values of pressure levels in the ERA-Interim driving Reanalysis and in the CRCM5 simulation can be another subject of future investigations.

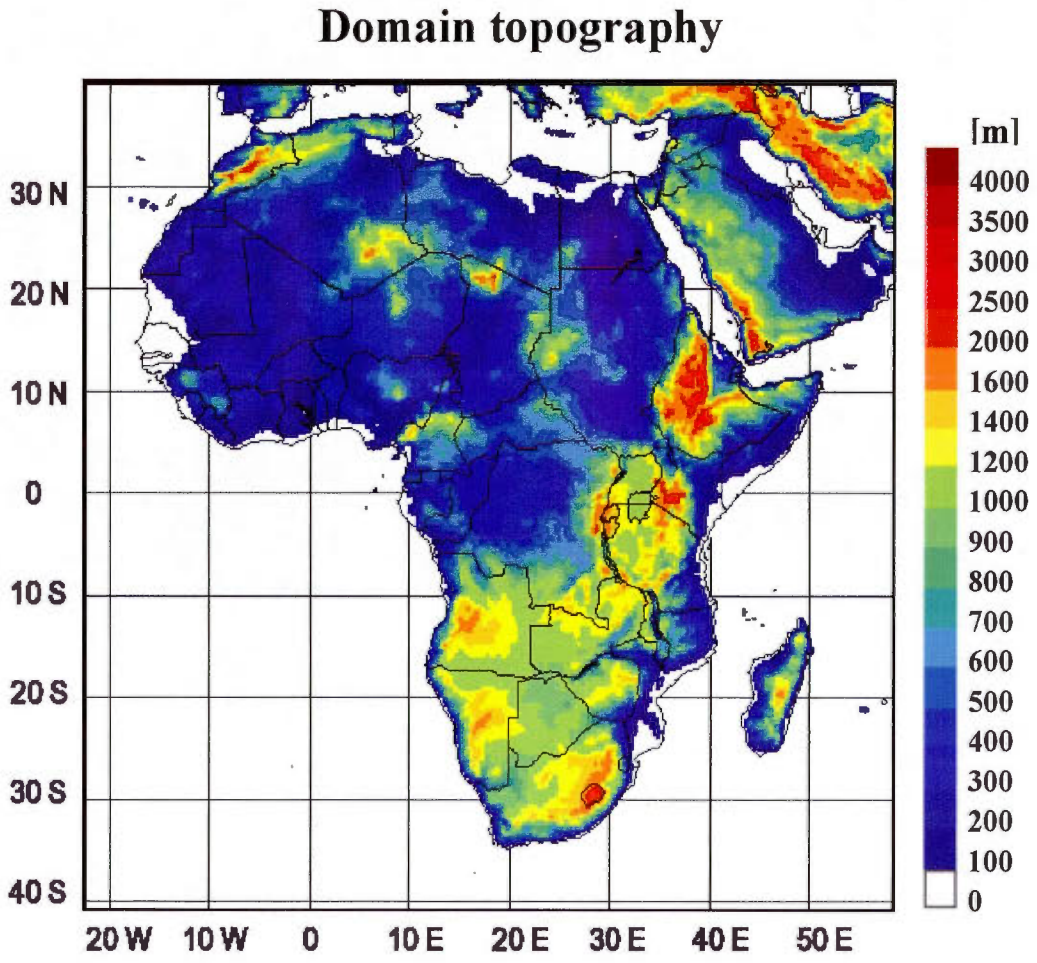

Fig. 2.1 Topographic height over the domain used for diagnostics (m)

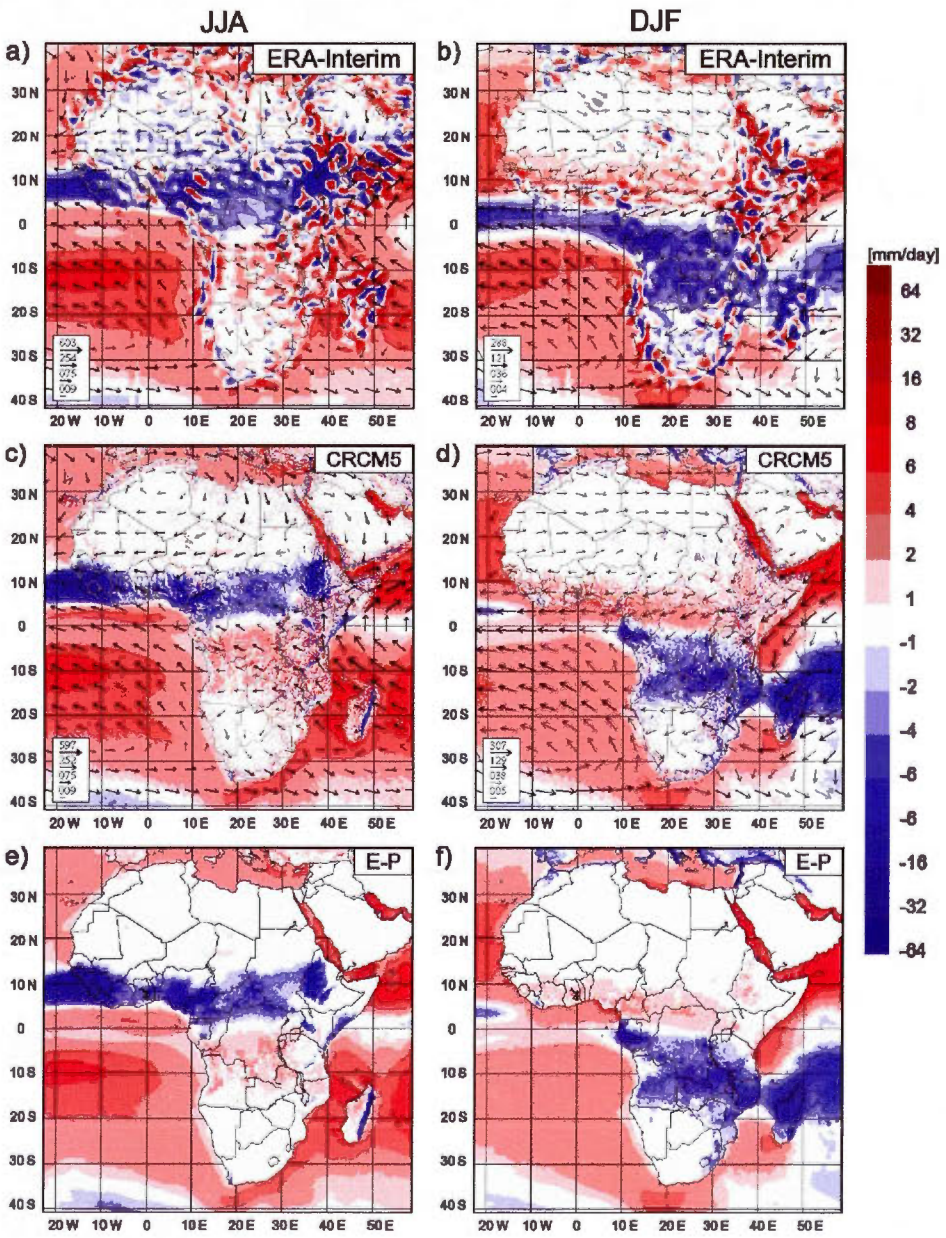

Fig. 2.2 Seasonal mean (1994-2008) for JJA (left column) and DJF (right column) of the vertically integrated moisture flux (arrows, kg m^{-1} s^{-1}) and its divergence (colour scale), calculated from ERA-Interim reanalysis (a, b) and the CRCM5-simulation (c, d), as well as the difference between the CRCM5-simulated evaporation E and precipitation P (e, f), used as proxy of the vertically integrated moisture flux divergence in the model.

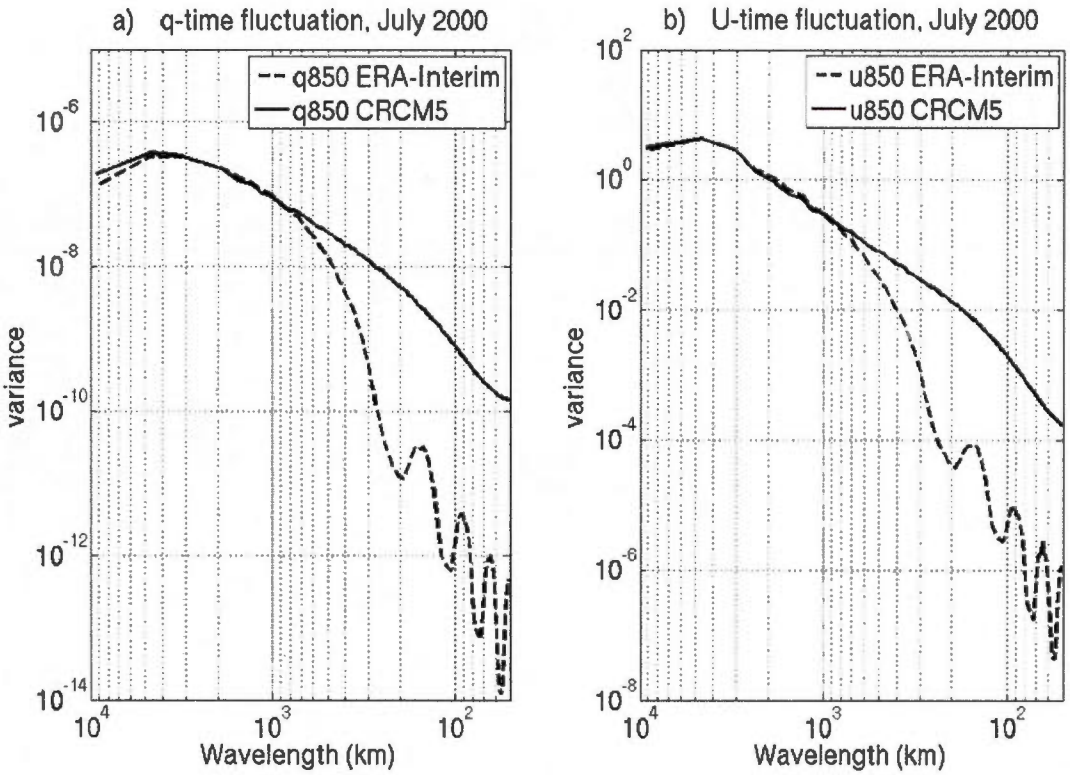

Fig. 2.3 Spectra of the time fluctuation of the specific humidity and zonal wind at 850 hPa for the month of July 2000, from CRCM5 and ERA-Interim. The oscillations below 200 km in ERA-Interim spectra arise from interpolation of the Reanalysis fields with horizontal resolution of 220 km on CRCM5 grid with horizontal resolution of 25 km.

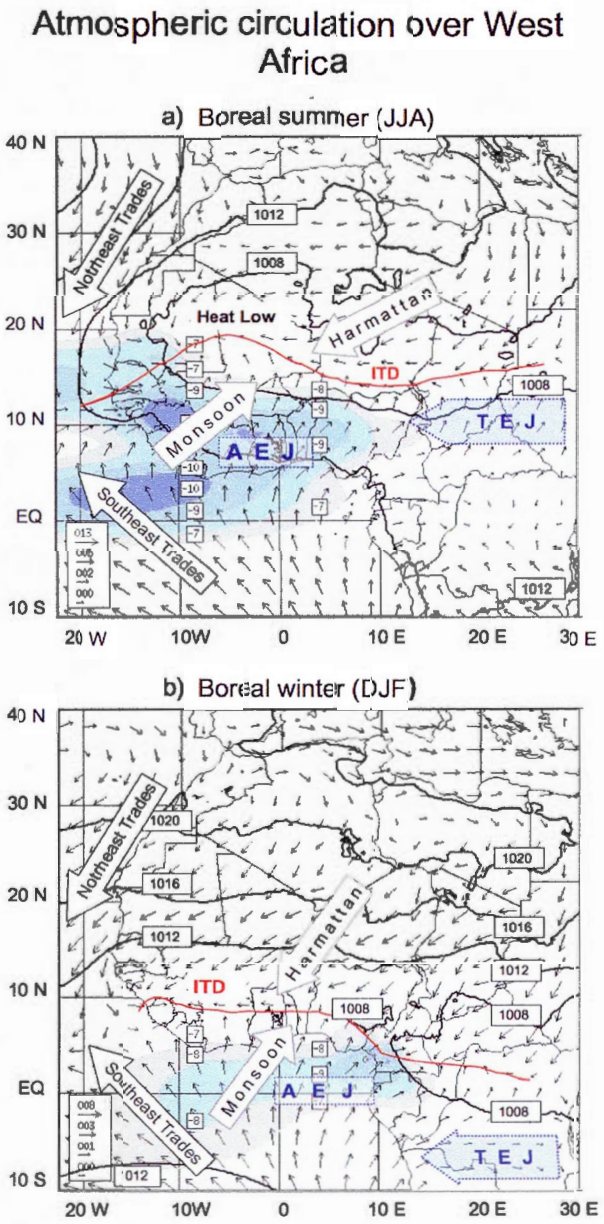

Fig. 3.1 West African monsoon circulation, as simulated by CRCM5: seasonal mean (1994-2008) sea-level pressure (hPa) (black contour) and 1000 hPa-winds (ms^{-1}) for JJA (a) and DJF (b). The confluence between the monsoon flux and Harmattan wind defines Inter-Tropical Discontinuity (ITD). Isoline 1008 hPa in boreal summer marks Saharan Heat Low (SHL). The medium-level African Easterly Jet (AEJ) is represented by the maximum of zonal wind at 600 hPa (in colours). The blue arrow illustrates the position of the Tropical Easterly Jet (TEJ) between 150-200 hPa.

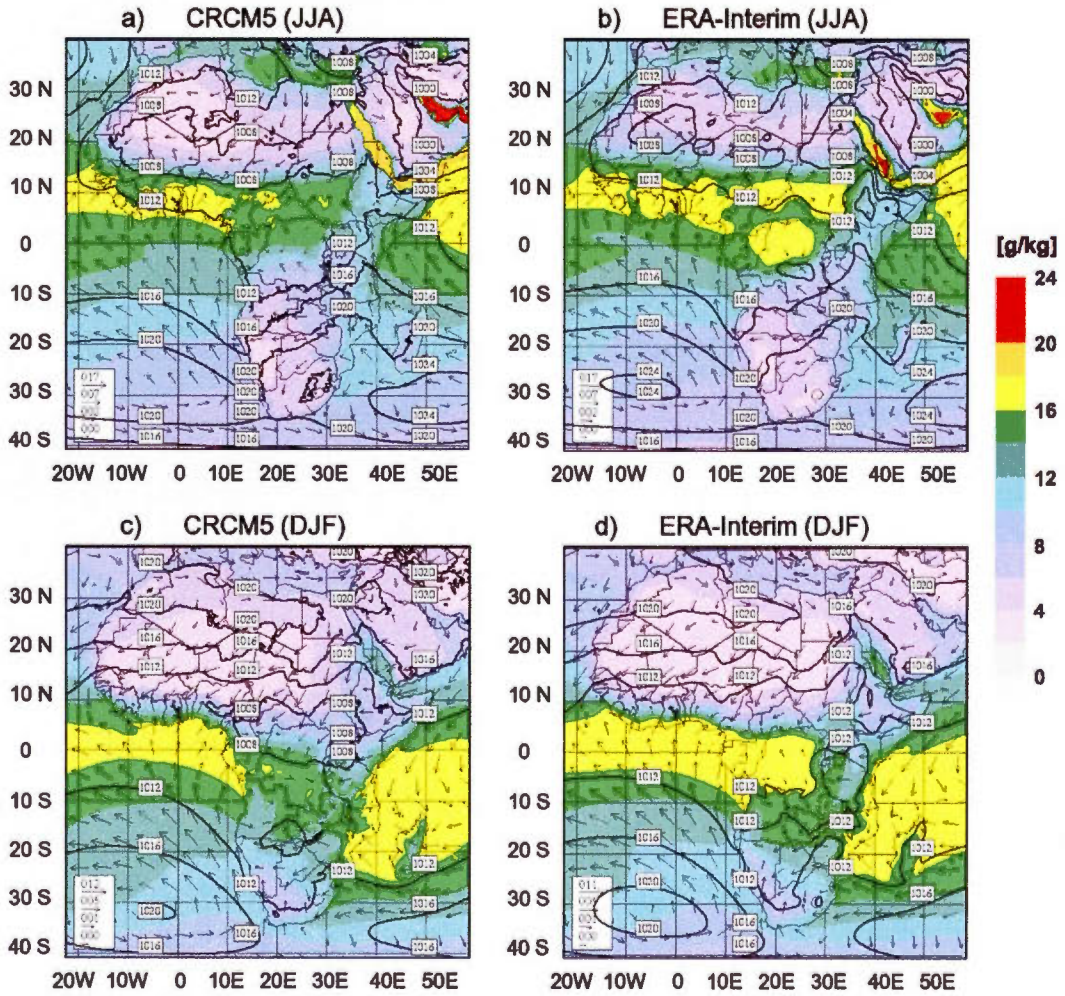

Fig. 3.2 JJA (top) and DJF (bottom) seasonal mean (1994-2008) specific humidity (shaded) and wind vectors (m s^{-1}) at 1000 hPa, and sea level pressure (contour interval 4 hPa) from CRCM5 (a, c) and ERA-Interim (b, d). The confluence between southwesterly and northeasterly winds in JJA marks the location of the Inter-tropical Discontinuity (ITD) around 13°N in CRCM5 (a) and 20°N in ERA-Interim (b).

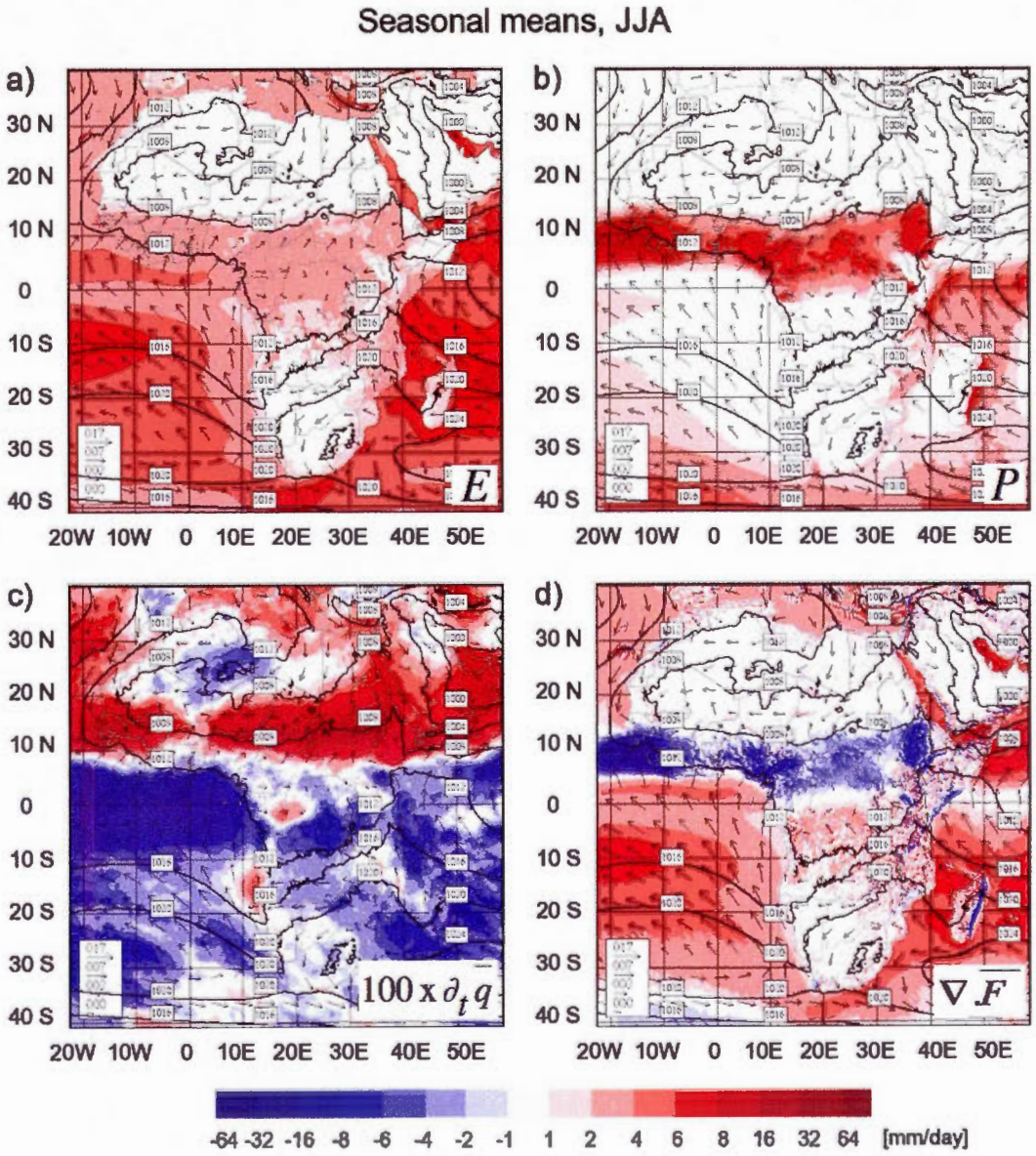

Fig. 4.1 Seasonal mean water vapour budget for JJA (1994-2008) calculated from the CRCM5 simulation: evapotranspiration (a), precipitation (b), vertically integrated water vapour tendency $\partial_t \overline{q}$ (c) and divergence of the vertically integrated moisture flux $\nabla \bullet \overline{\mathbf{F}}$ (d). The sea-level pressure (interval of 4 hPa) and the 1000 hPa-wind vectors (m s^{-1}) are superimposed.

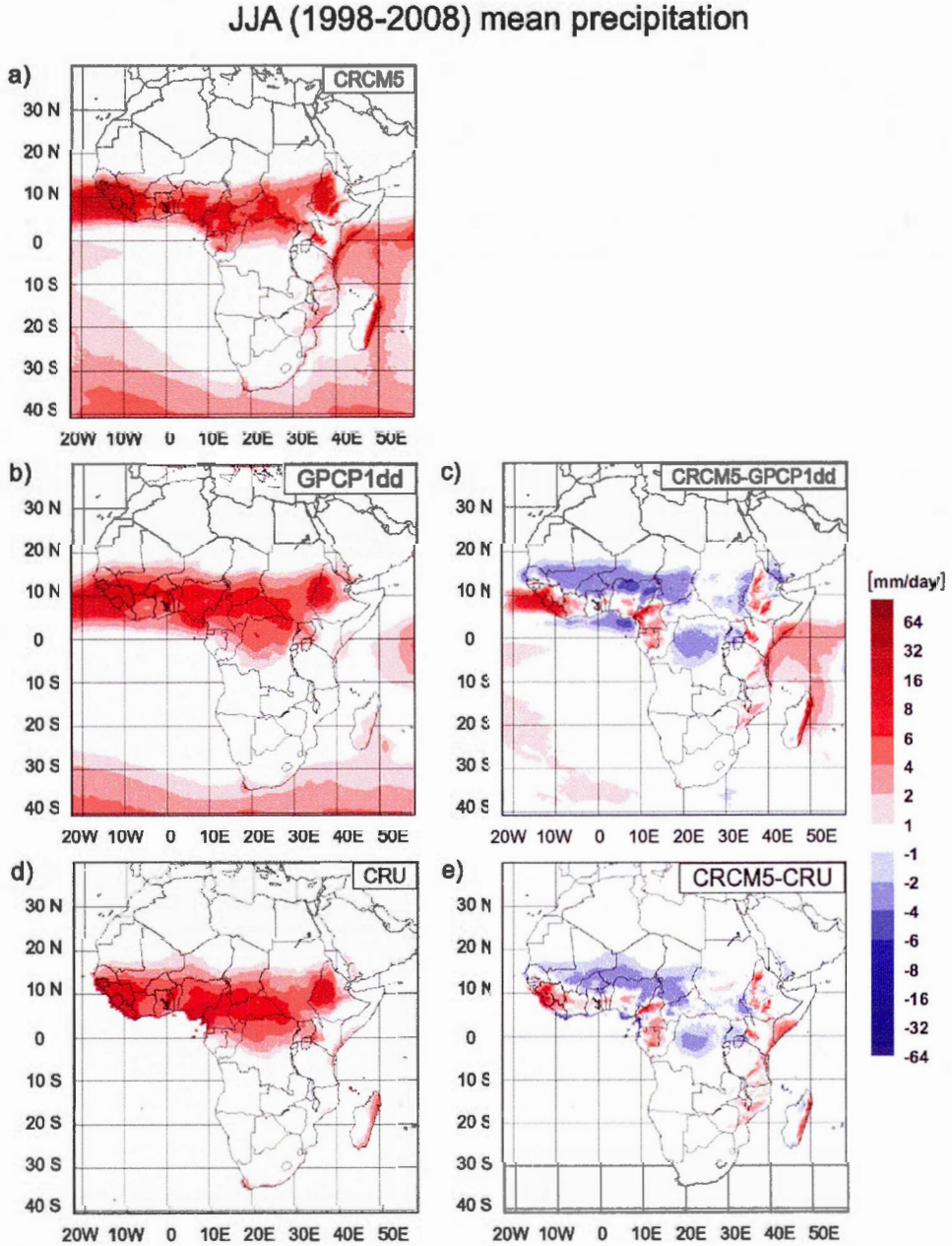

Fig. 4.2 Seasonal mean precipitation for JJA (1998-2008) from CRCM5 (a), GPCP1dd (b) and CRU (d), as well as the difference between CRCM5 and GPCP1dd (c) and CRCM5 and CRU (e).

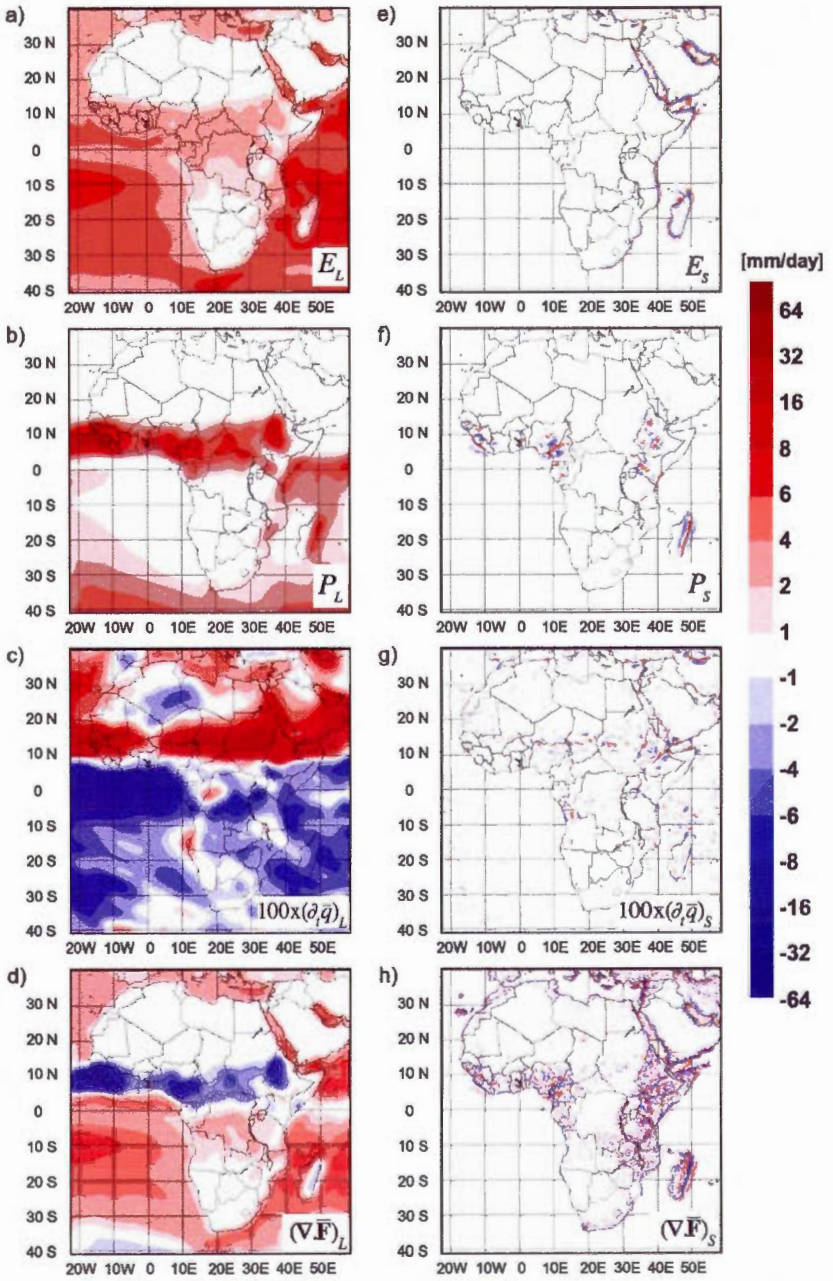

Fig. 4.3 Decomposed seasonal mean (JJA, 1994-2008) evapotranspiration (E), precipitation (P), vertically integrated water vapour tendency ($\partial_t \bar{q}$) and divergence of the vertically integrated moisture flux ($\nabla \bullet \bar{\mathbf{F}}$): large scales (a-d) and small scales (e-h).

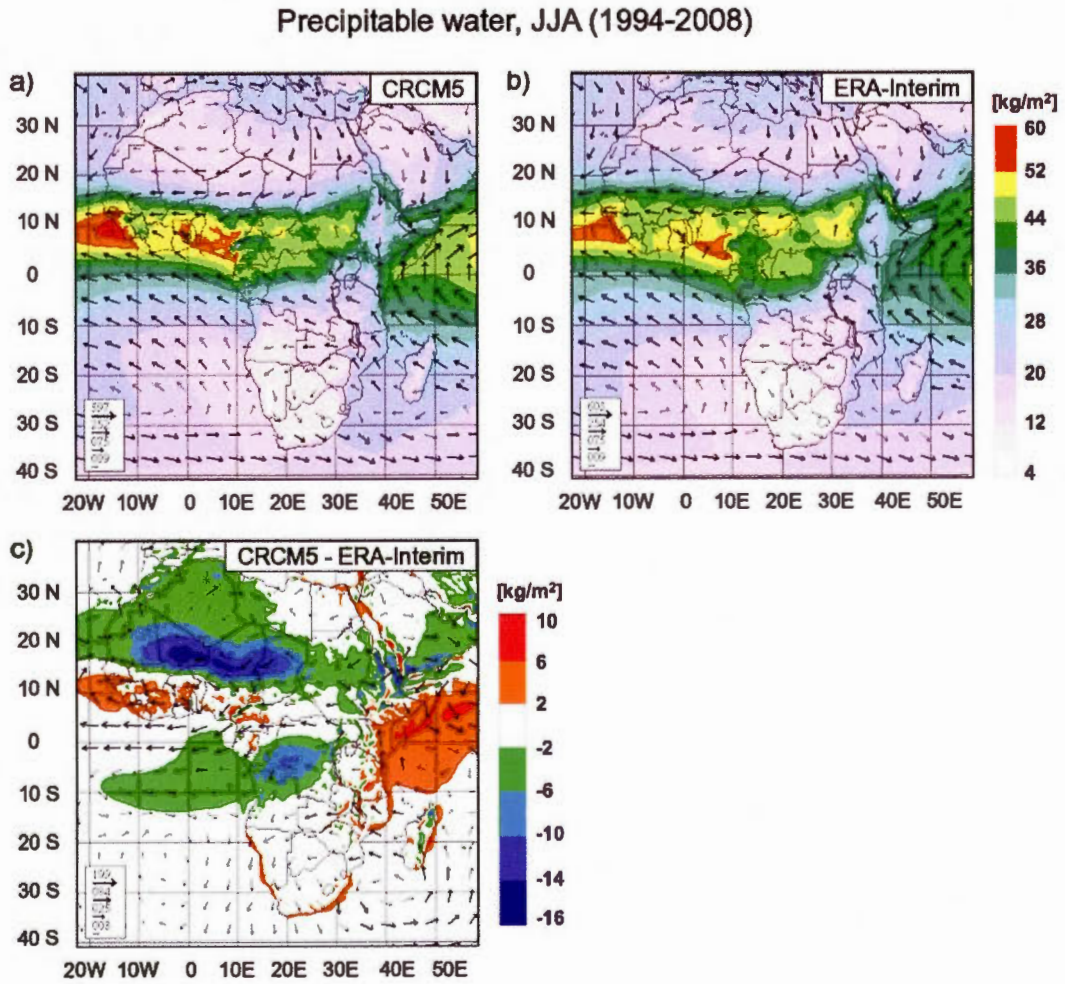

Fig. 4.4 Vertically integrated specific humidity (precipitable water, in colours) for JJA (1994-2008) from CRCM5 (a) and ERA-Interim driving reanalysis (b), with superimposed vertically integrated moisture fluxes (arrows, kg $m^{-1}s^{-1}$), and the difference between CRCM5 and ERA-Interim (c).

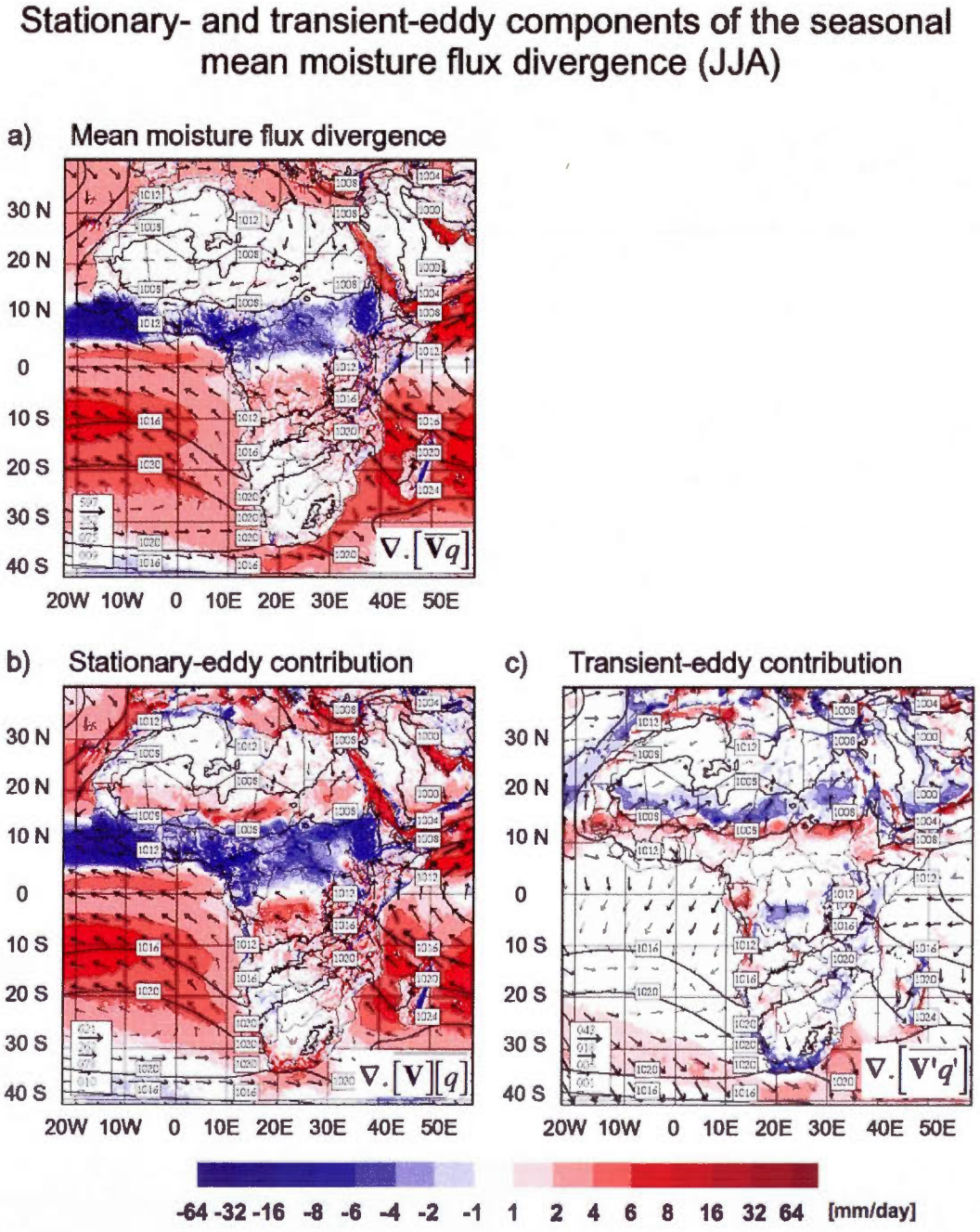

Fig. 4.5 Seasonal mean (a) vertically integrated moisture flux (arrows, kg m^{-1} s^{-1}) and its divergence (colours), and their component due to (b) stationary and (c) transient eddies. The sea-level pressure (hPa, thick lines) is also traced (JJA, 1994-2008).

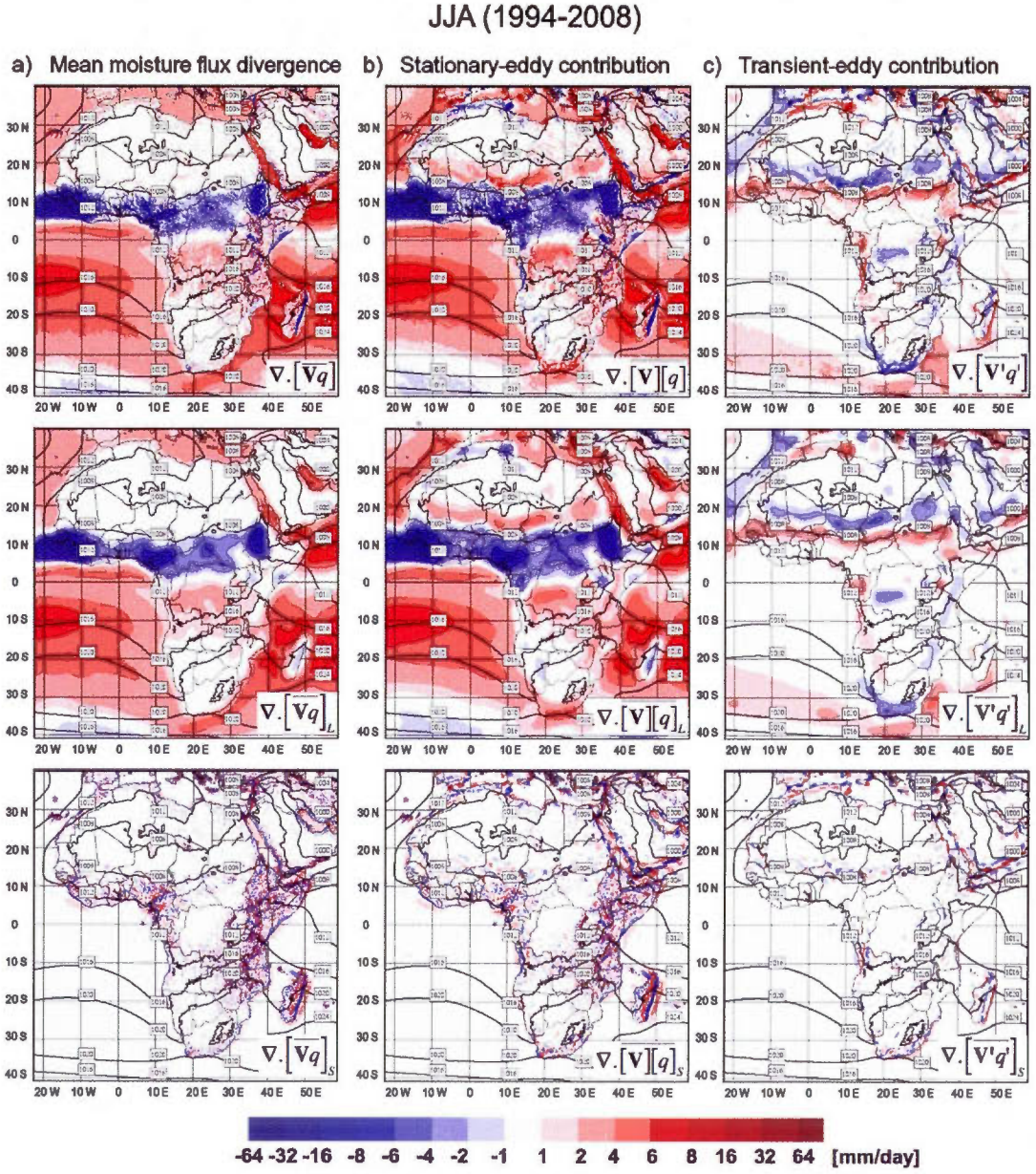

Fig. 4.6 Total (first row), large-scale (second row) and small-scale (third row) component of the JJA-mean divergence of the vertically integrated moisture flux (a), its stationary-eddy contribution (b) and transient-eddy contribution (c). The sea-level pressure (hPa, thick lines) is the same as in previous figures.

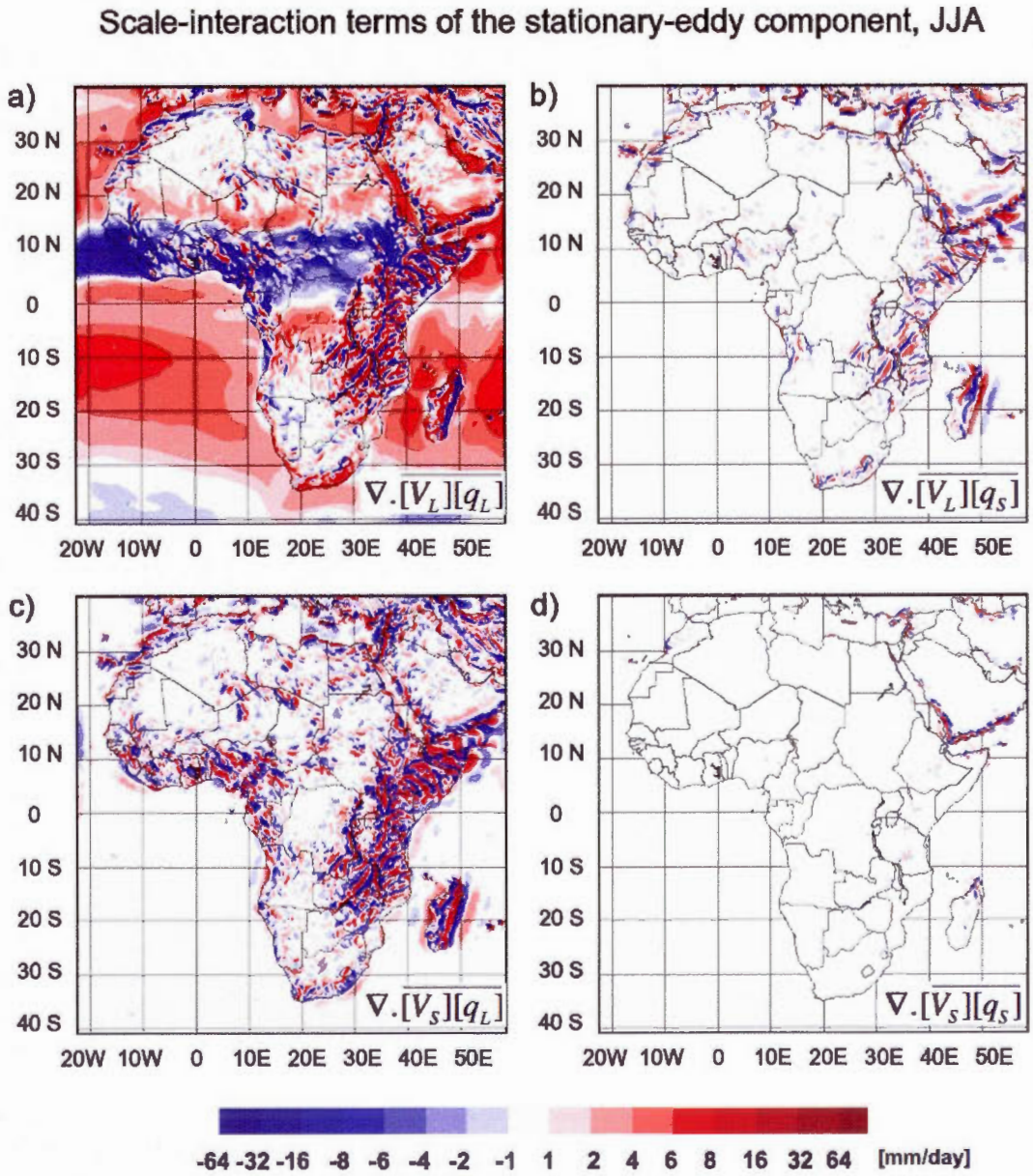

Fig. 4.7 Stationary-eddy component of the mean vertically integrated moisture divergence (JJA, 1994-2008), decomposed into four terms, representing interaction between (a) large-scale wind and large-scale humidity, (b) large-scale wind and small-scale humidity, (c) small-scale wind and large-scale humidity and (d) small-scale wind and small-scale humidity.

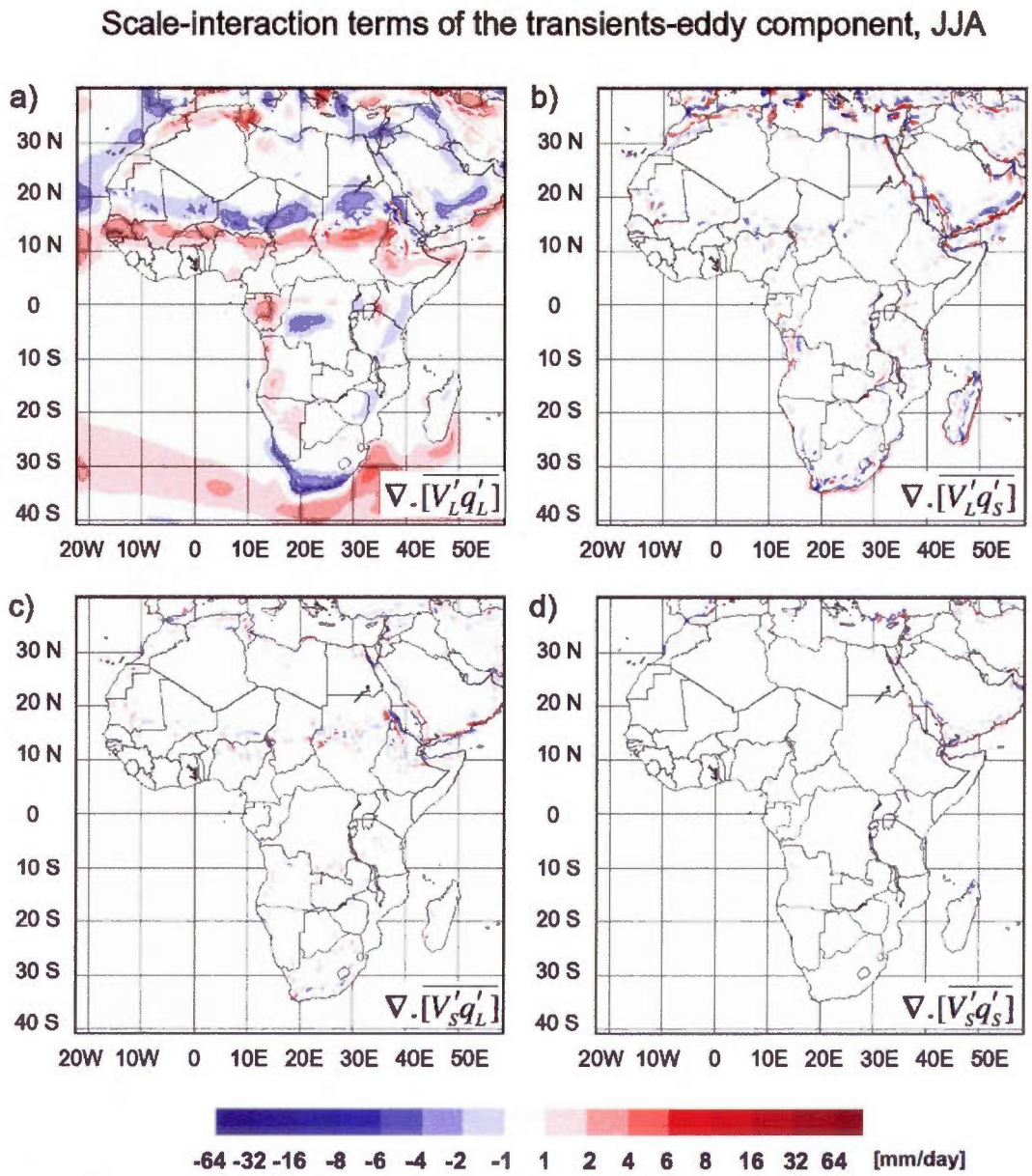

Fig. 4.8 Transient-eddy component of the mean vertically integrated moisture divergence (JJA, 1994-2008), decomposed into four terms, representing interaction between (a) large-scale wind and large-scale humidity, (b) large-scale wind and small-scale humidity, (c) small-scale wind and large-scale humidity and (d) small-scale wind and small-scale humidity.

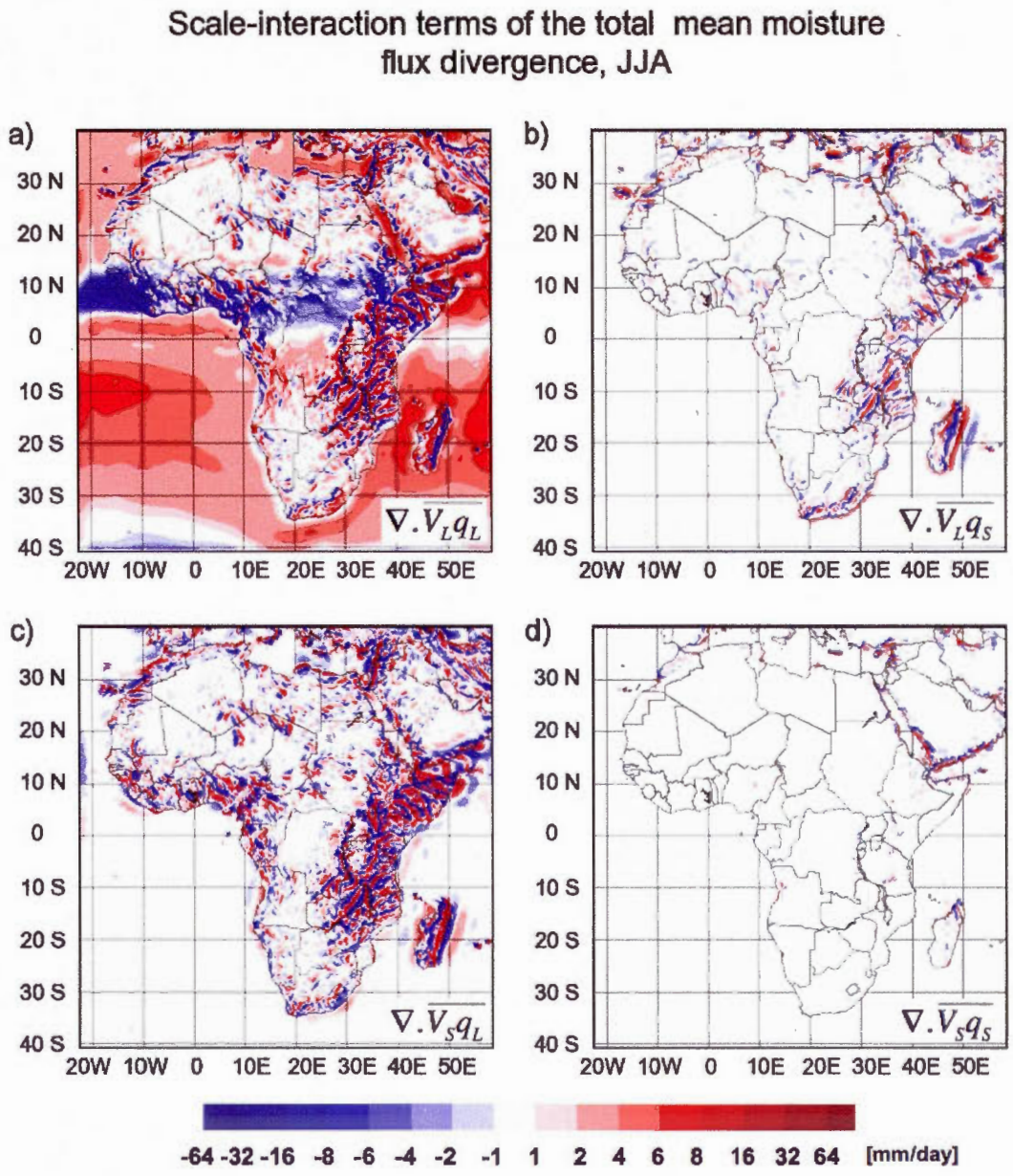

Fig. 4.9 Mean vertically integrated moisture divergence (JJA, 1994-2008), decomposed into four terms, representing interaction between (a) large-scale wind and large-scale humidity, (b) large-scale wind and small-scale humidity, (c) small-scale wind and large-scale humidity and (d) small-scale wind and small-scale humidity.

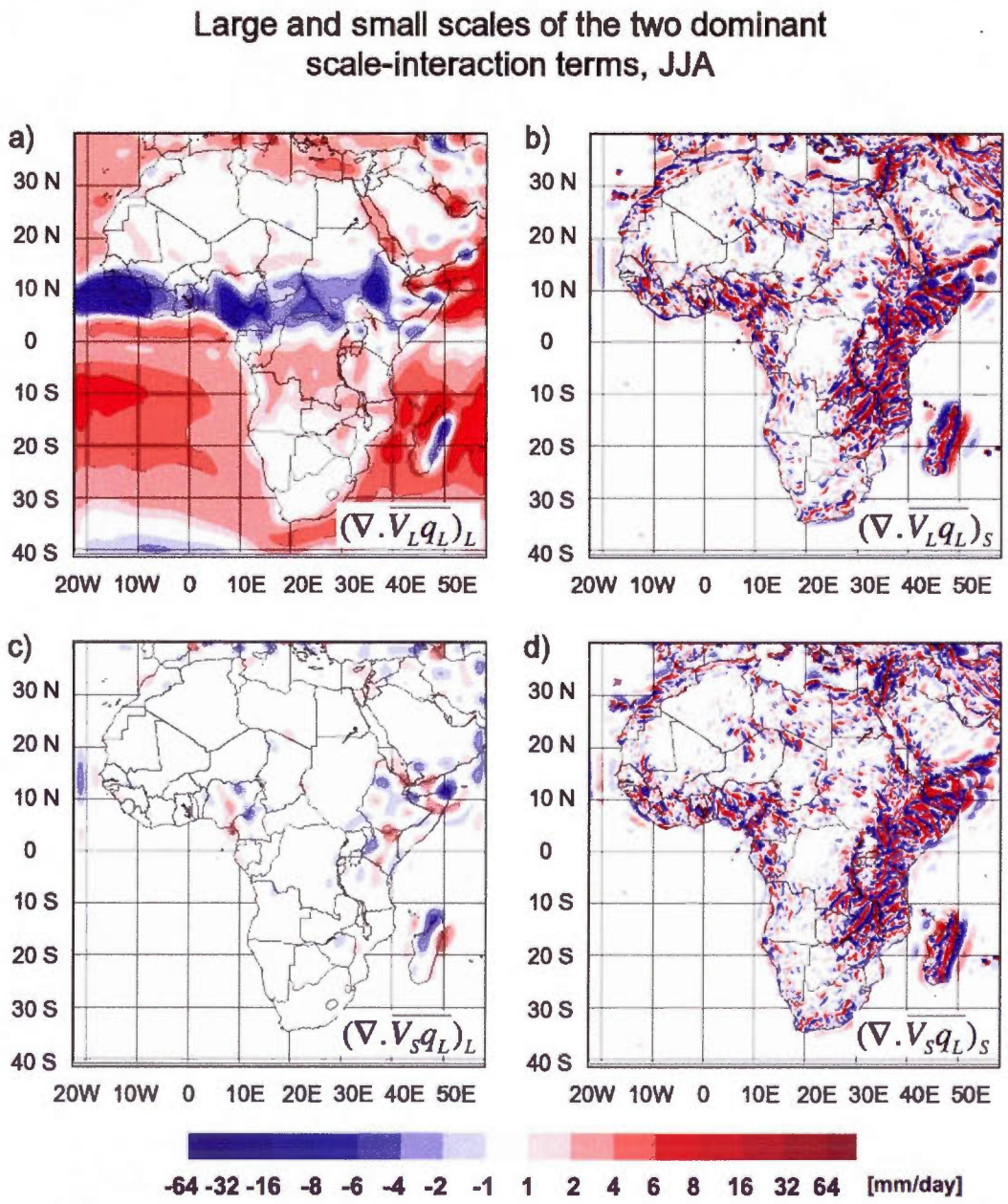

Fig. 4.10 Large (a, c) and small (b, d) scales of the two dominant terms $\nabla \bullet \overline{\mathbf{V}_L q_L}$ and $\nabla \bullet \overline{\mathbf{V}_S q_L}$ of the moisture divergence, (JJA 1994-2008).

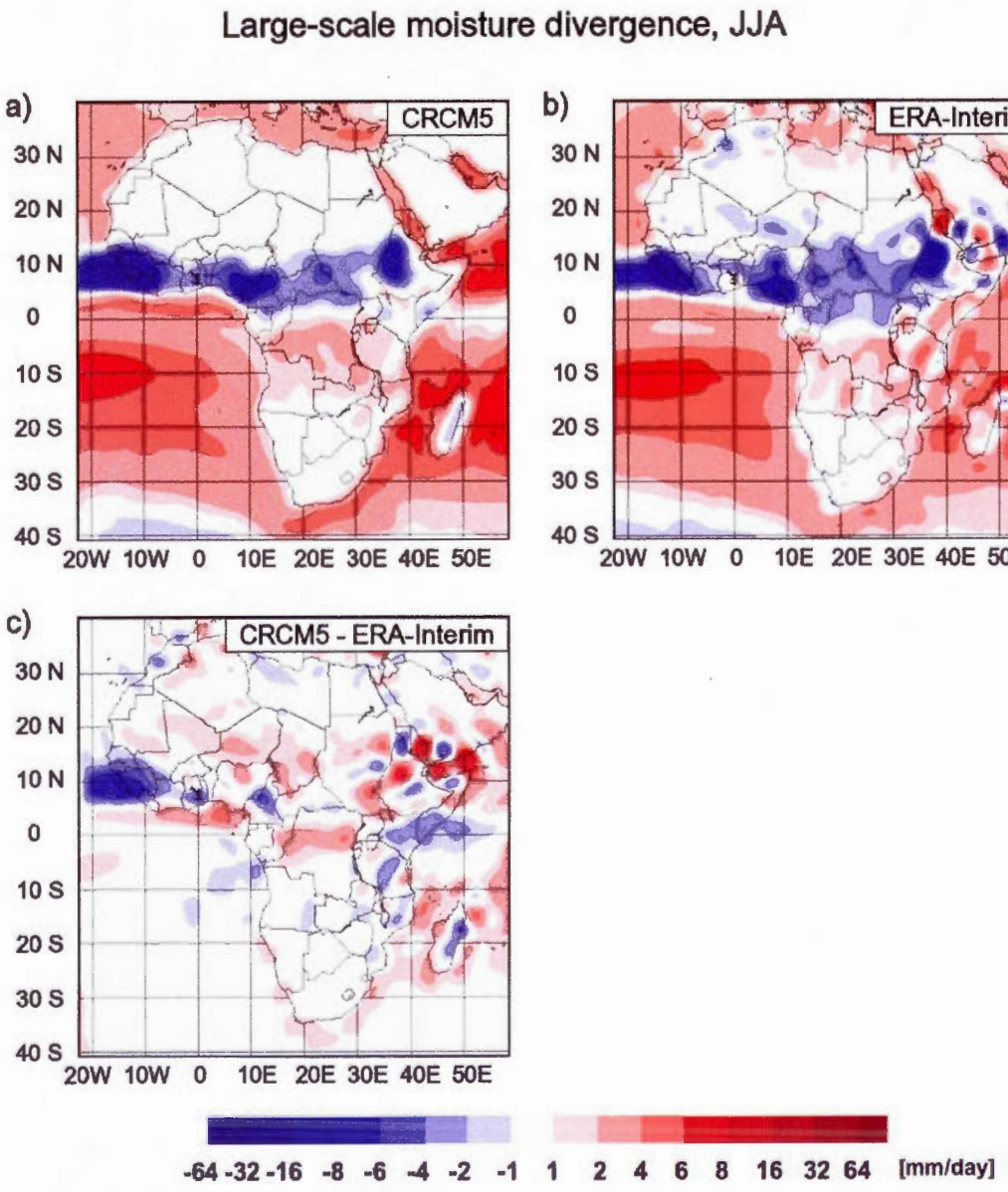

Fig. 4.11 Large scales of the mean moisture flux divergence (JJA, 1994-2008) calculated from the CRCM5 simulation (a) and ERA-Interim Reanalysis data (b), and the difference between them (c).

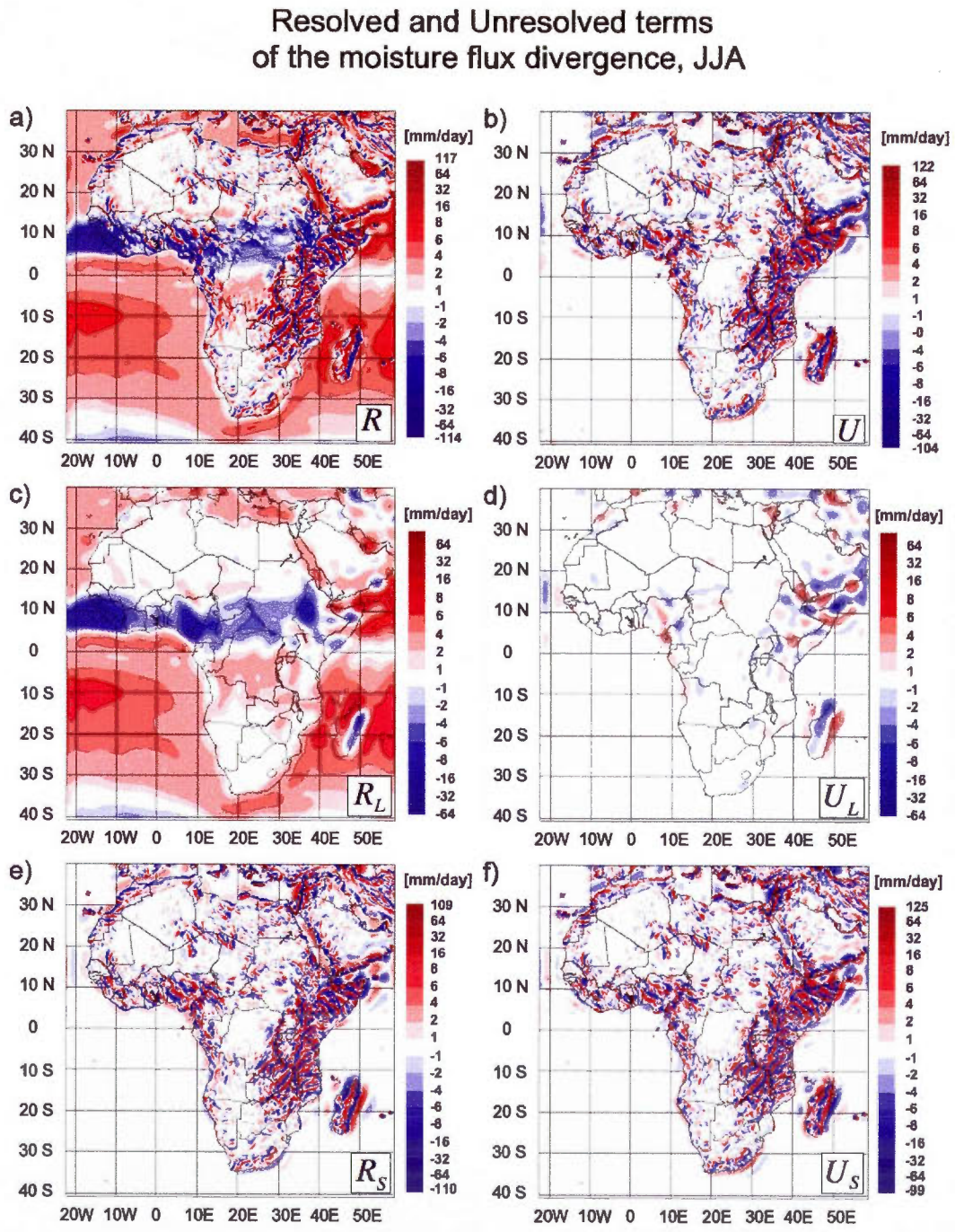

Fig. 4.12 Resolved R (a) and unresolved U (b) components of the seasonal-mean divergence of the integrated moisture flux and respectively their decomposition into large scales (c and d) and small scales (e and f), JJA (1994-2008).

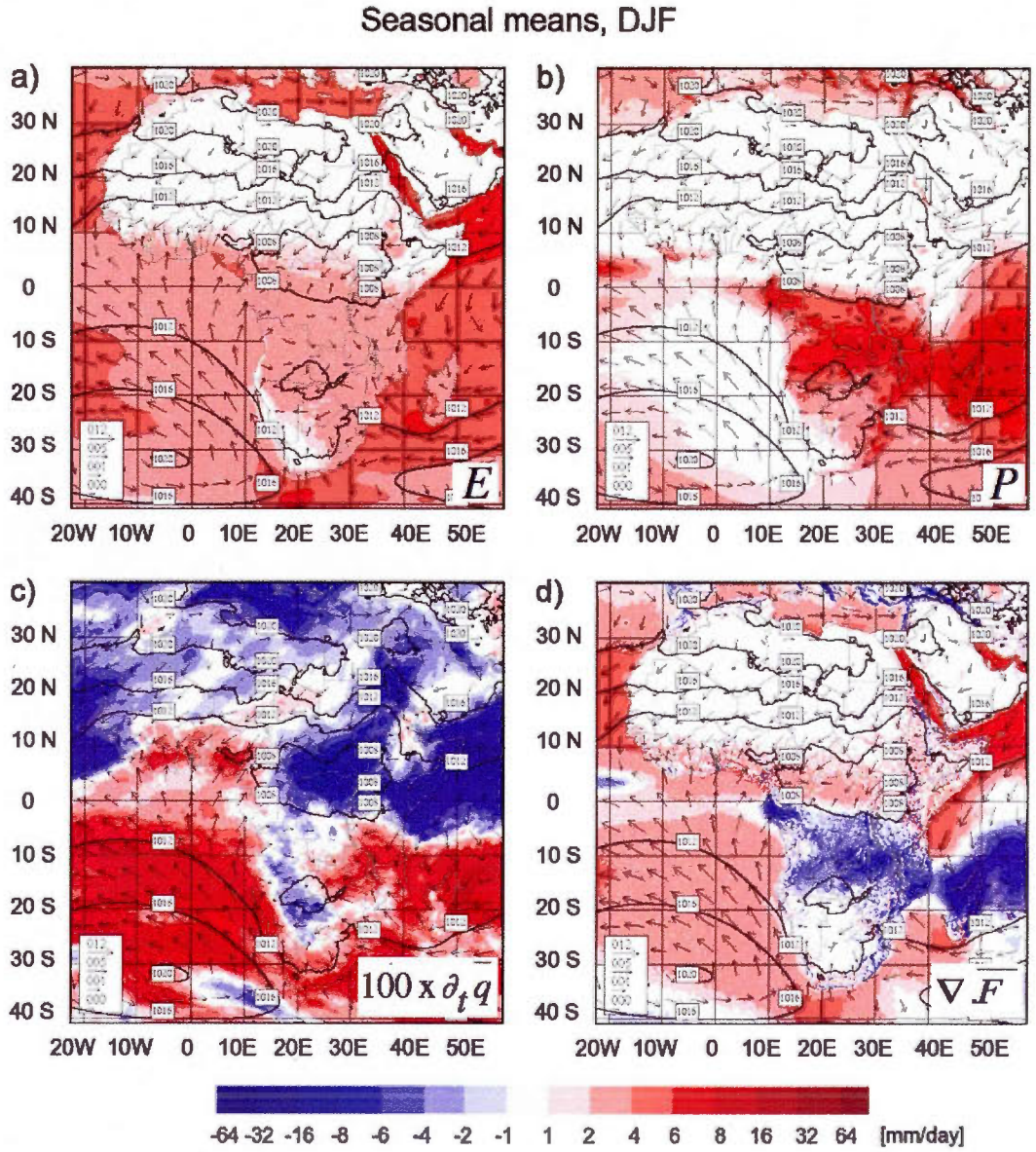

Fig. 4.13 Seasonal mean water vapour budget for DJF (1994-2008) calculated from the CRCM5 simulation: evapotranspiration (a), precipitation (b), vertically integrated water vapour tendency $\partial_t \overline{q}$ (c) and divergence of the vertically integrated moisture flux $\nabla \bullet \overline{\mathbf{F}}$ (d). The sea-level pressure (interval of 4 hPa) and the 1000 hPa-wind vectors (m s^{-1}) are superimposed.

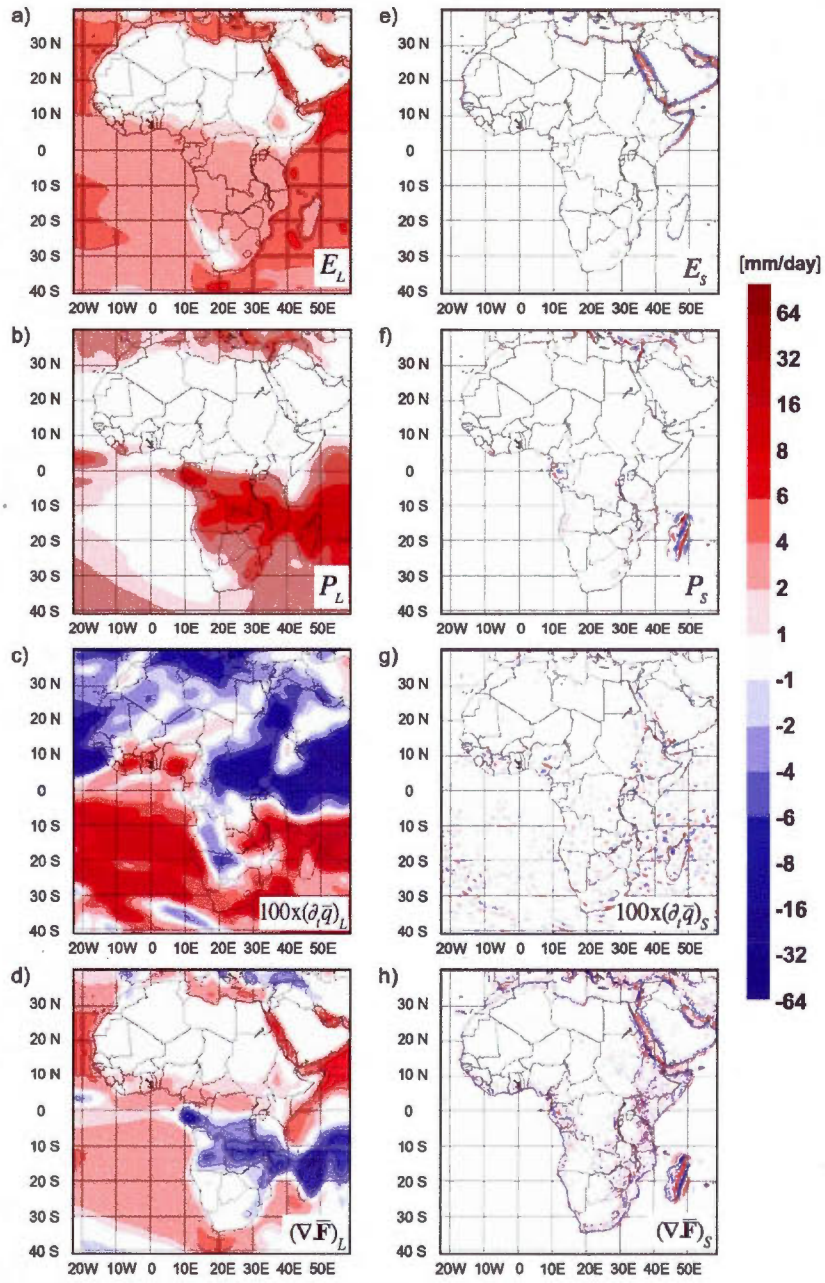

Fig. 4.14 Decomposed seasonal mean (DJF, 1994-2008) evapotranspiration (E), precipitation (P), vertically integrated water vapour tendency ($\partial_t \bar{q}$) and divergence of the vertically integrated moisture flux ($\nabla \bullet \bar{\mathbf{F}}$): large scales (a-d) and small scales (e-h).

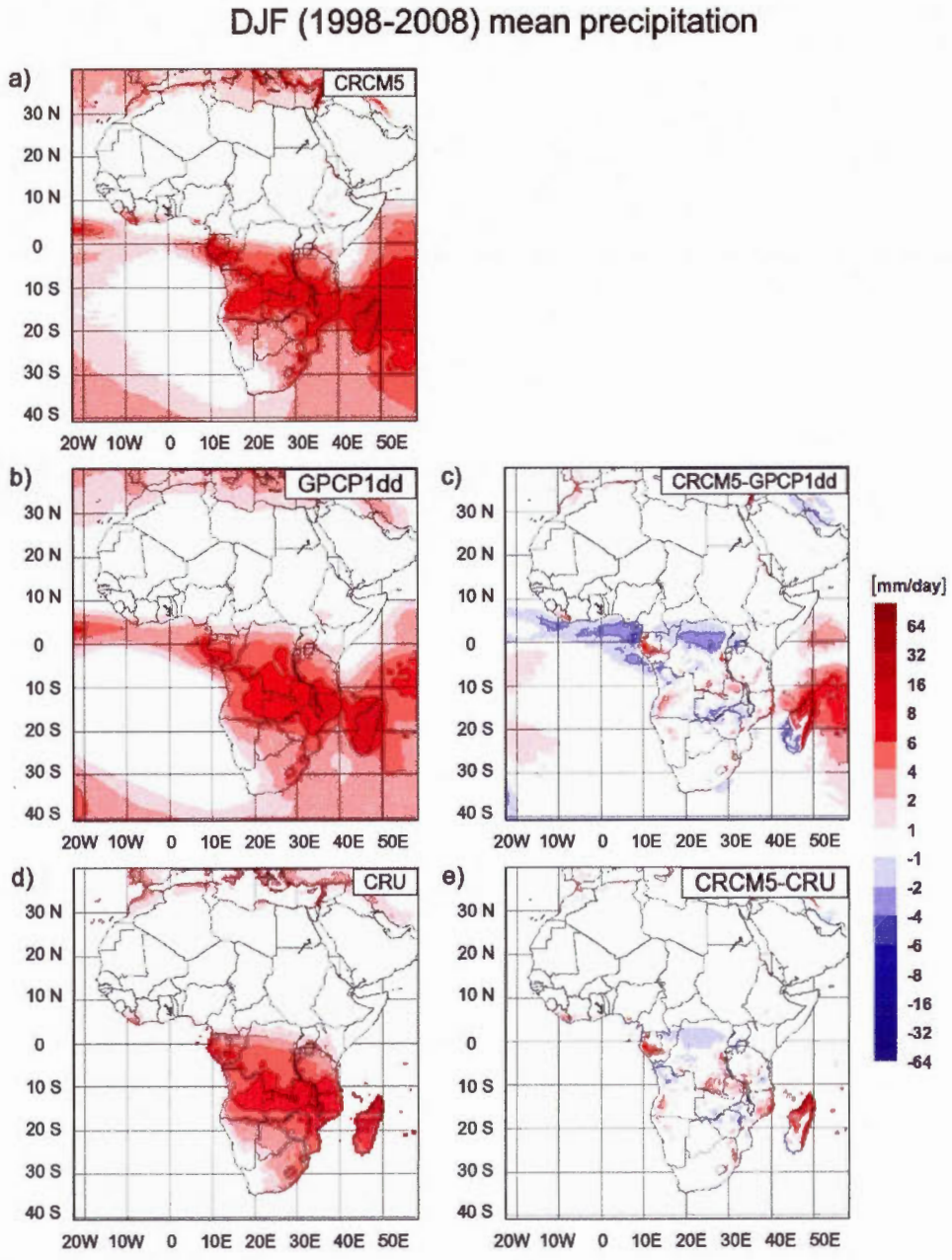

Fig. 4.15 Seasonal mean precipitation for DJF (1998-2008) from CRCM5 (a), GPCP1dd (b) and CRU (d), as well as the difference between CRCM5 and GPCP1dd (c) and CRCM5 and CRU (e).

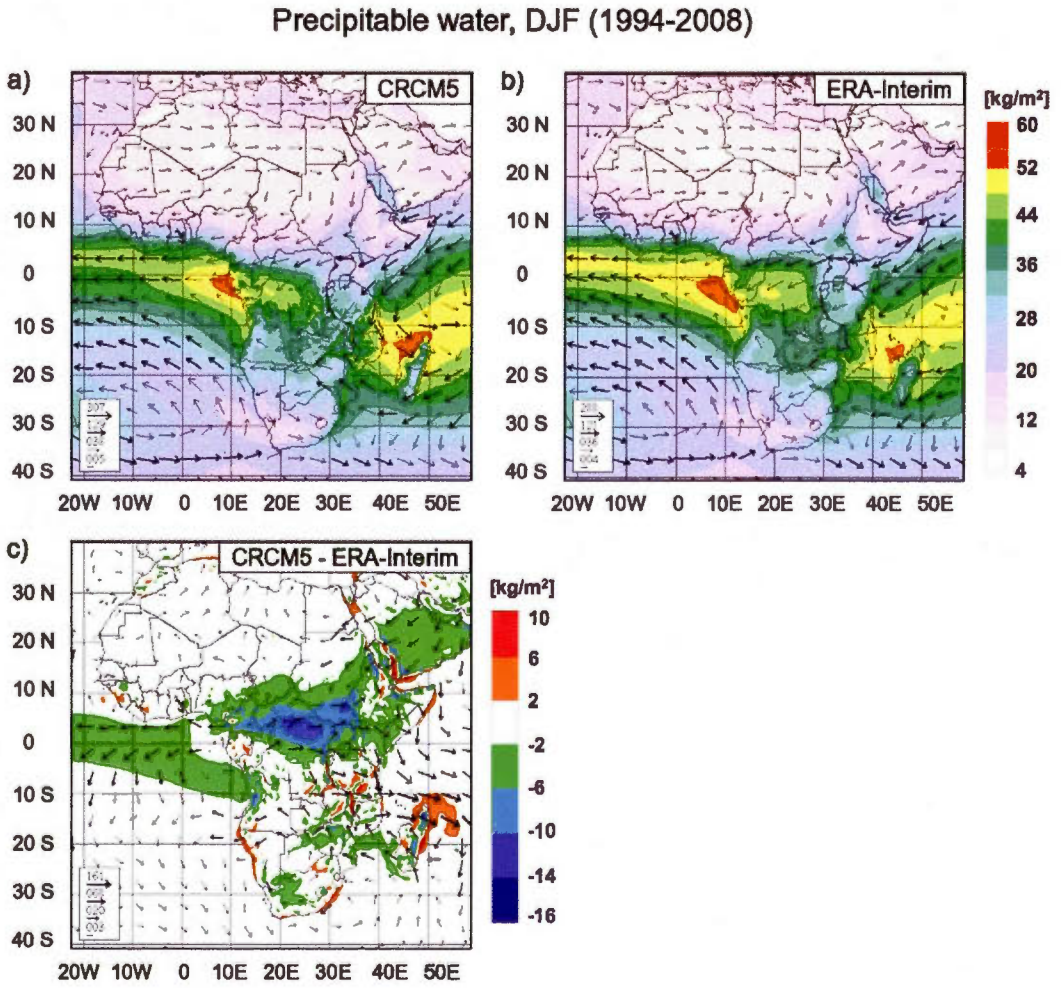

Fig. 4.16 Vertically integrated specific humidity (precipitable water, in colours) for DJF (1994-2008) from CRCM5 (a) and ERA-Interim driving reanalysis (b), with superimposed vertically integrated moisture fluxes (arrows, kg $m^{-1}s^{-1}$), and the difference between CRCM5 and ERA-Interim (c).

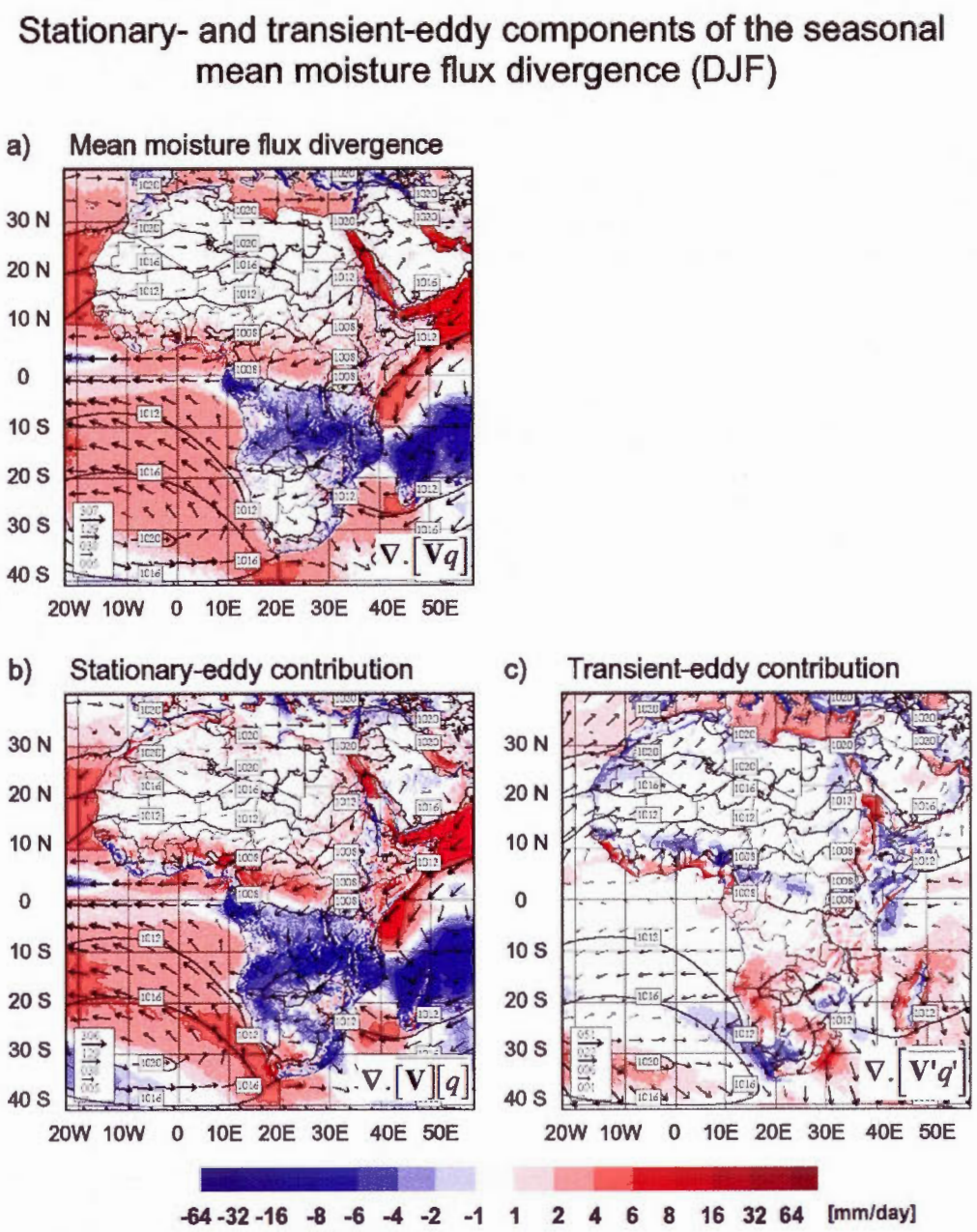

Fig. 4.17 Seasonal mean (a) vertically integrated moisture flux (arrows, kg m^{-1} $s^{-1)}$ and its divergence (colours), and their component due to (b) stationary and (c) transient eddies. The sea-level pressure (hPa, thick lines) is also traced (DJF, 1994-2008).

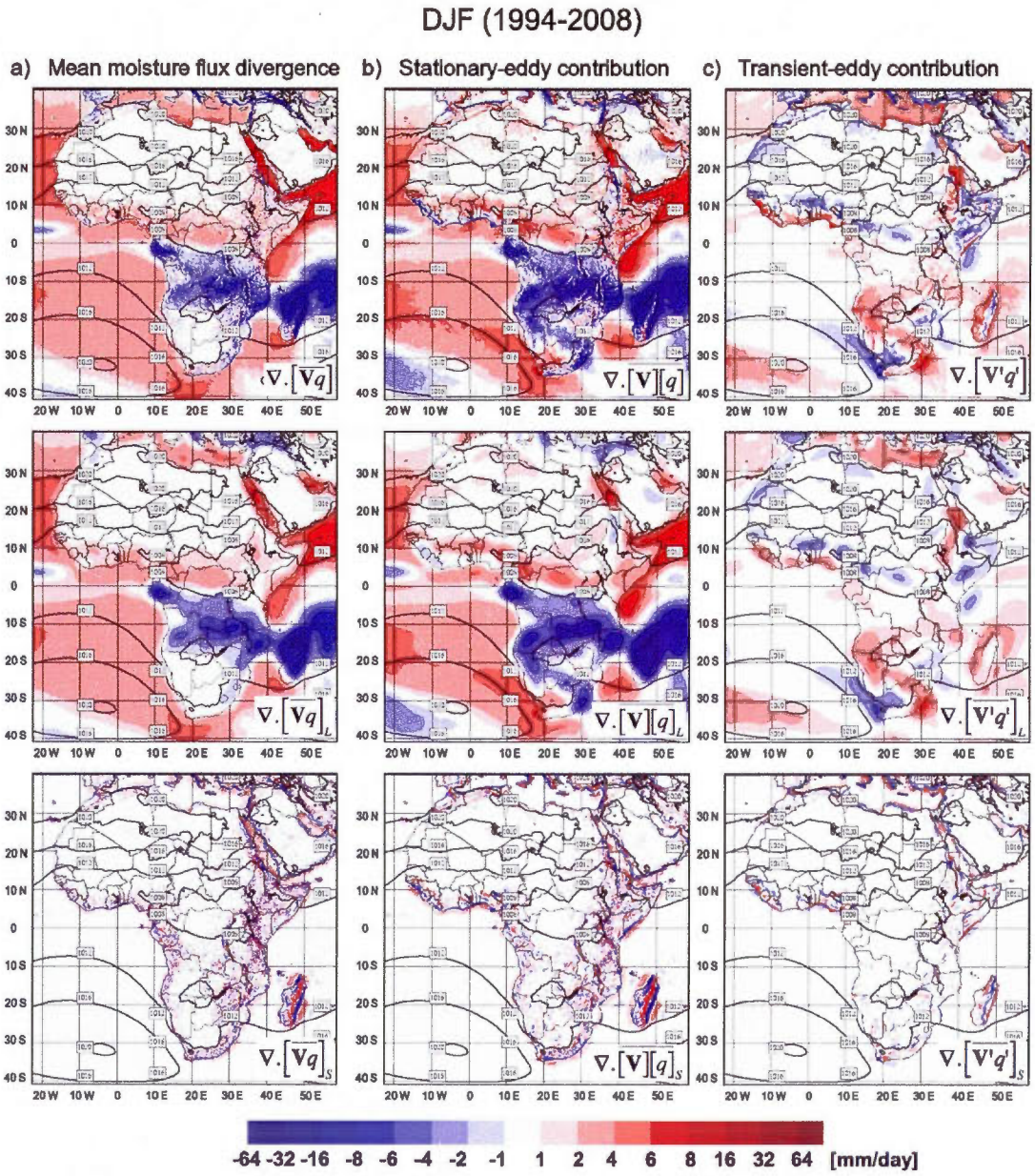

Fig. 4.18 Total (first row), large-scale (second row) and small-scale (third row) component of the DJF-mean divergence of the vertically integrated moisture flux (a), its stationary-eddy contribution (b) and transient-eddy contribution (c). The sea-level pressure (hPa, thick lines) is the same as in previous figures.

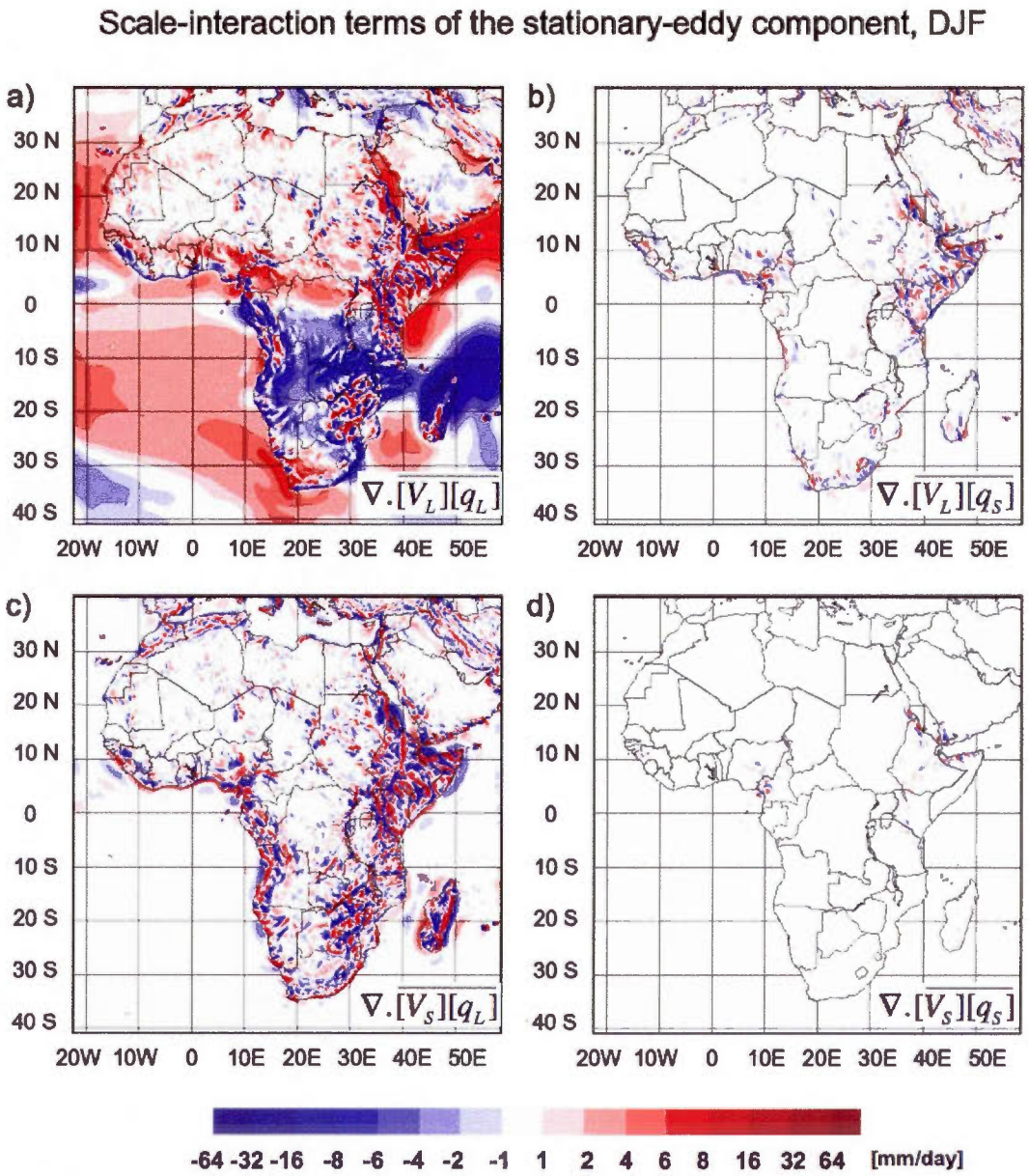

Fig. 4.19 Stationary-eddy component of the mean vertically integrated moisture divergence (DJF, 1994-2008), decomposed into four terms, representing interaction between (a) large-scale wind and large-scale humidity, (b) large-scale wind and small-scale humidity, (c) small-scale wind and large-scale humidity and (d) small-scale wind and small-scale humidity.

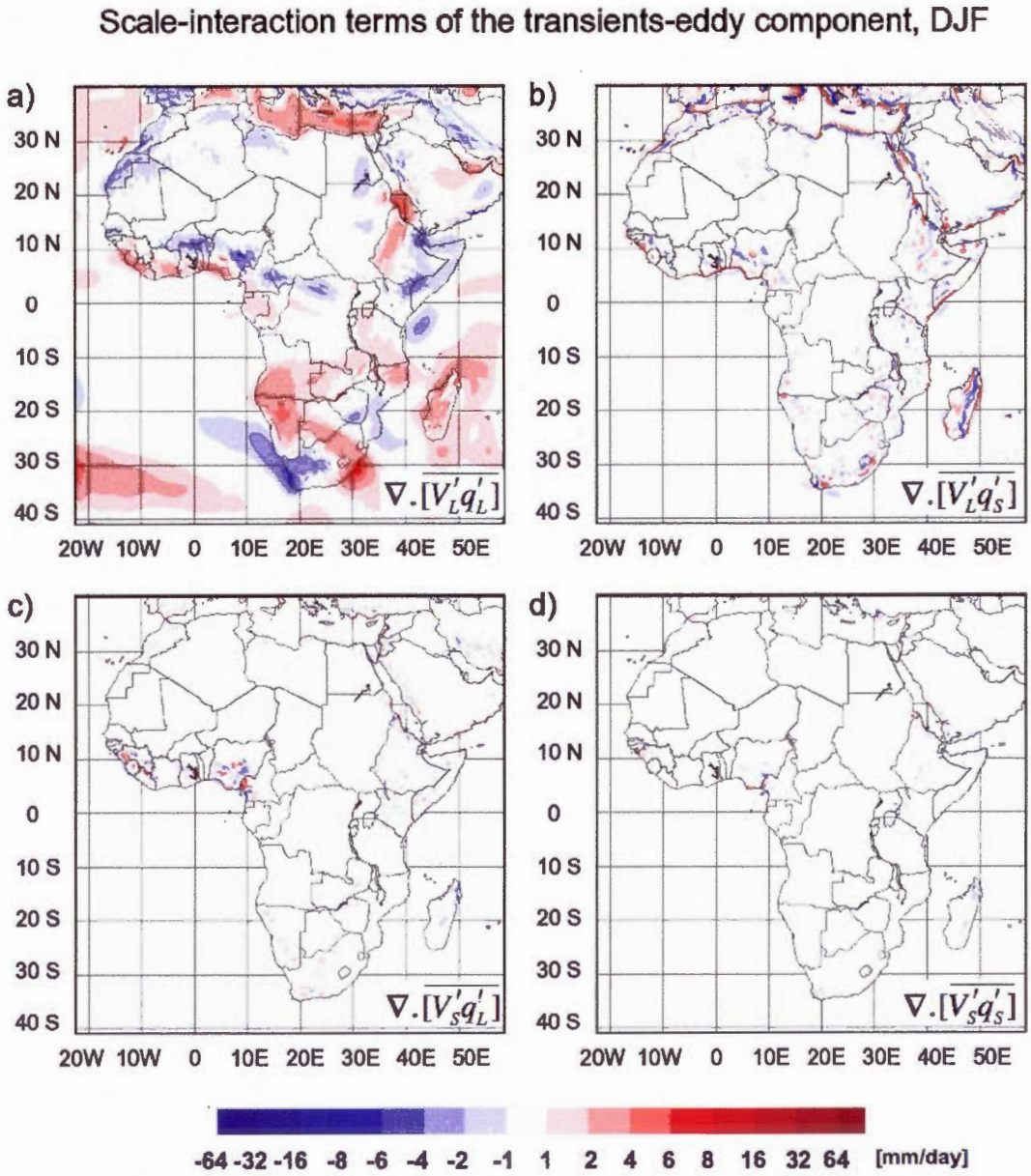

Fig. 4.20 Transient-eddy component of the mean vertically integrated moisture divergence (DJF, 1994-2008), decomposed into four terms, representing interaction between (a) large-scale wind and large-scale humidity, (b) large-scale wind and small-scale humidity, (c) small-scale wind and large-scale humidity and (d) small-scale wind and small-scale humidity.

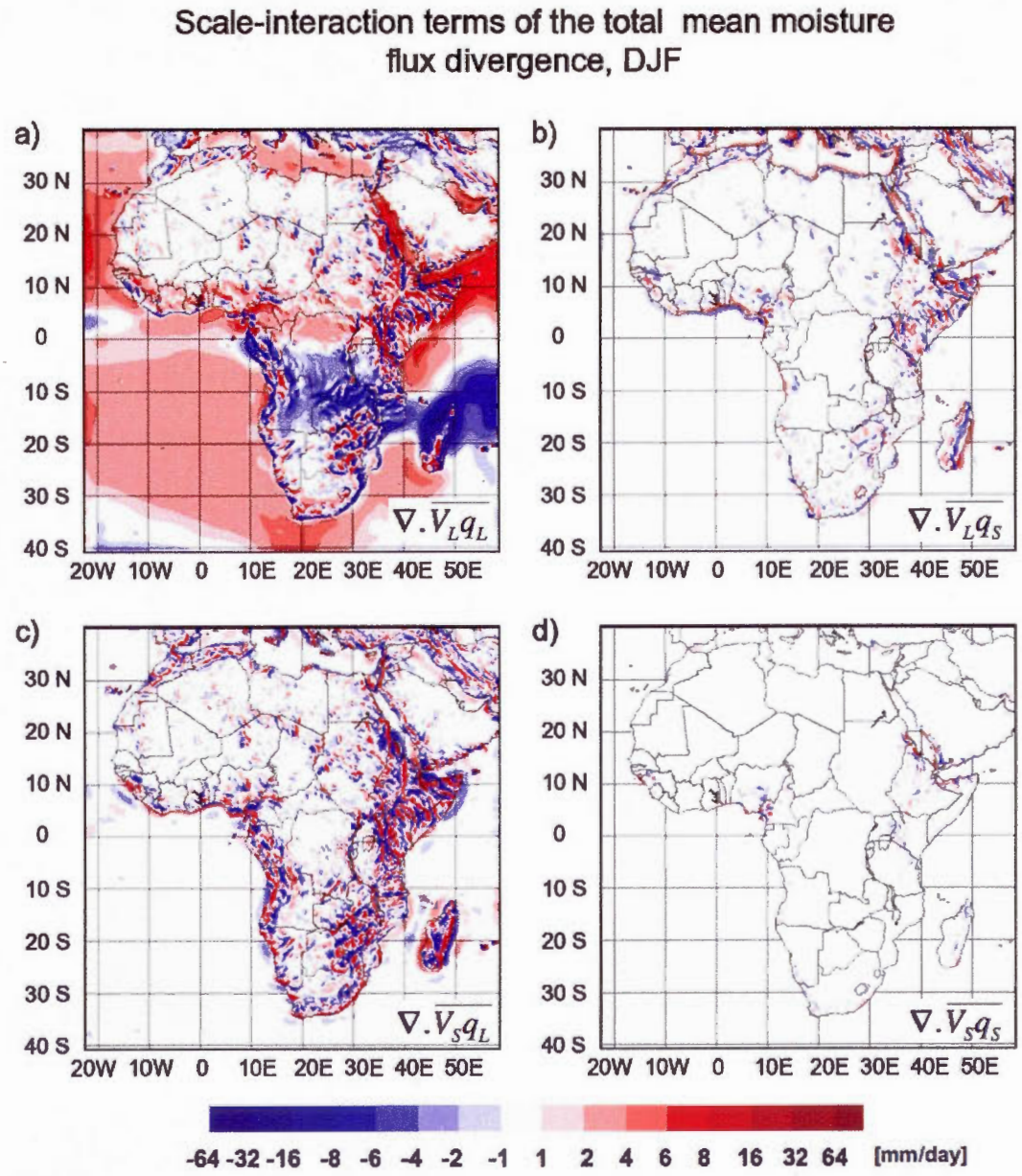

Fig. 4.21 Mean vertically integrated moisture divergence (DJF, 1994-2008), decomposed into four terms, representing interaction between (a) large-scale wind and large-scale humidity, (b) large-scale wind and small-scale humidity, (c) small-scale wind and large-scale humidity and (d) small-scale wind and small-scale humidity.

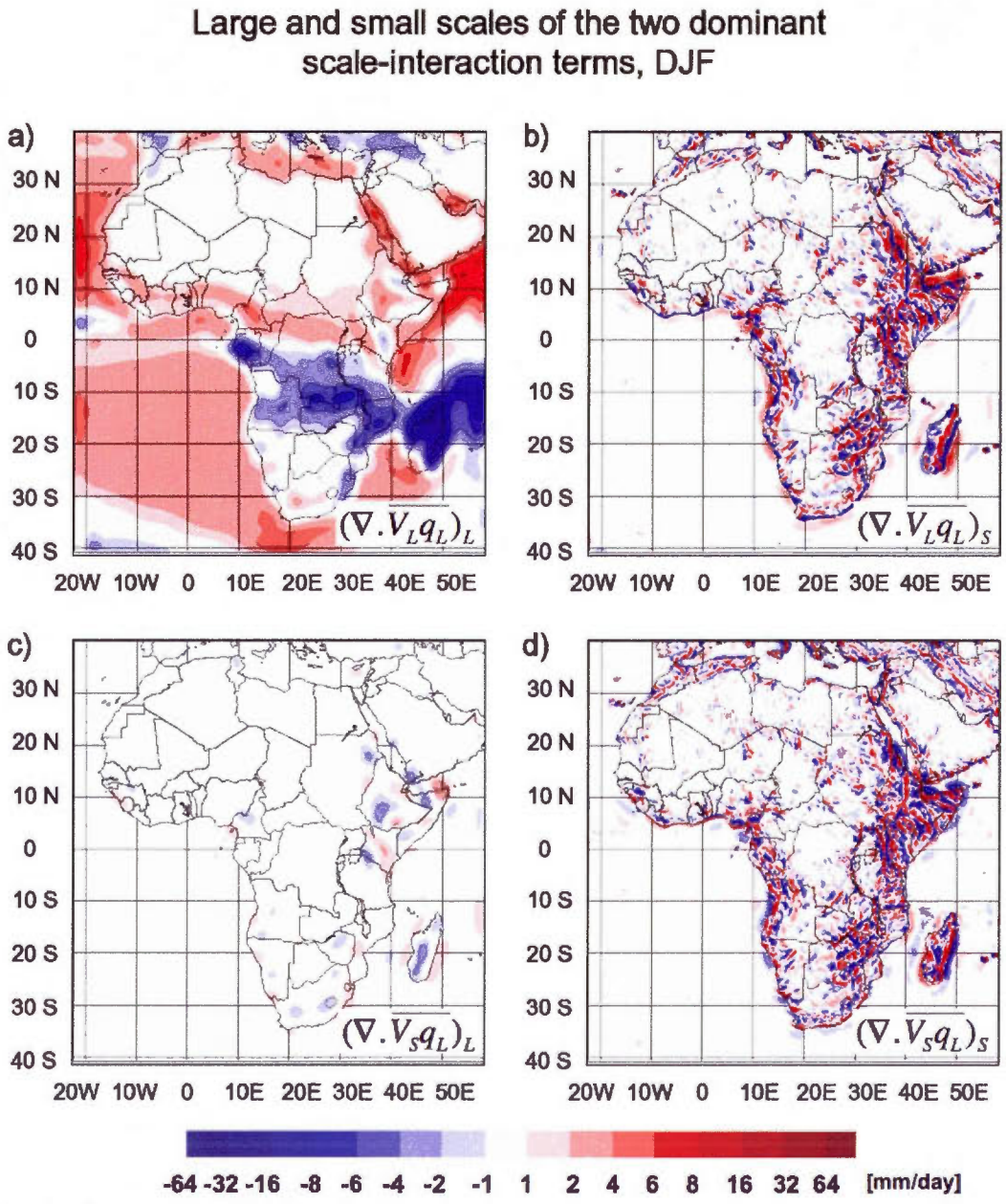

Fig. 4.22 Large (a, c) and small (b, d) scales of the two dominant terms $\nabla \bullet \overline{\mathbf{V}_L q_L}$ and $\nabla \bullet \overline{\mathbf{V}_S q_L}$ of the moisture divergence, (DJF 1994-2008).

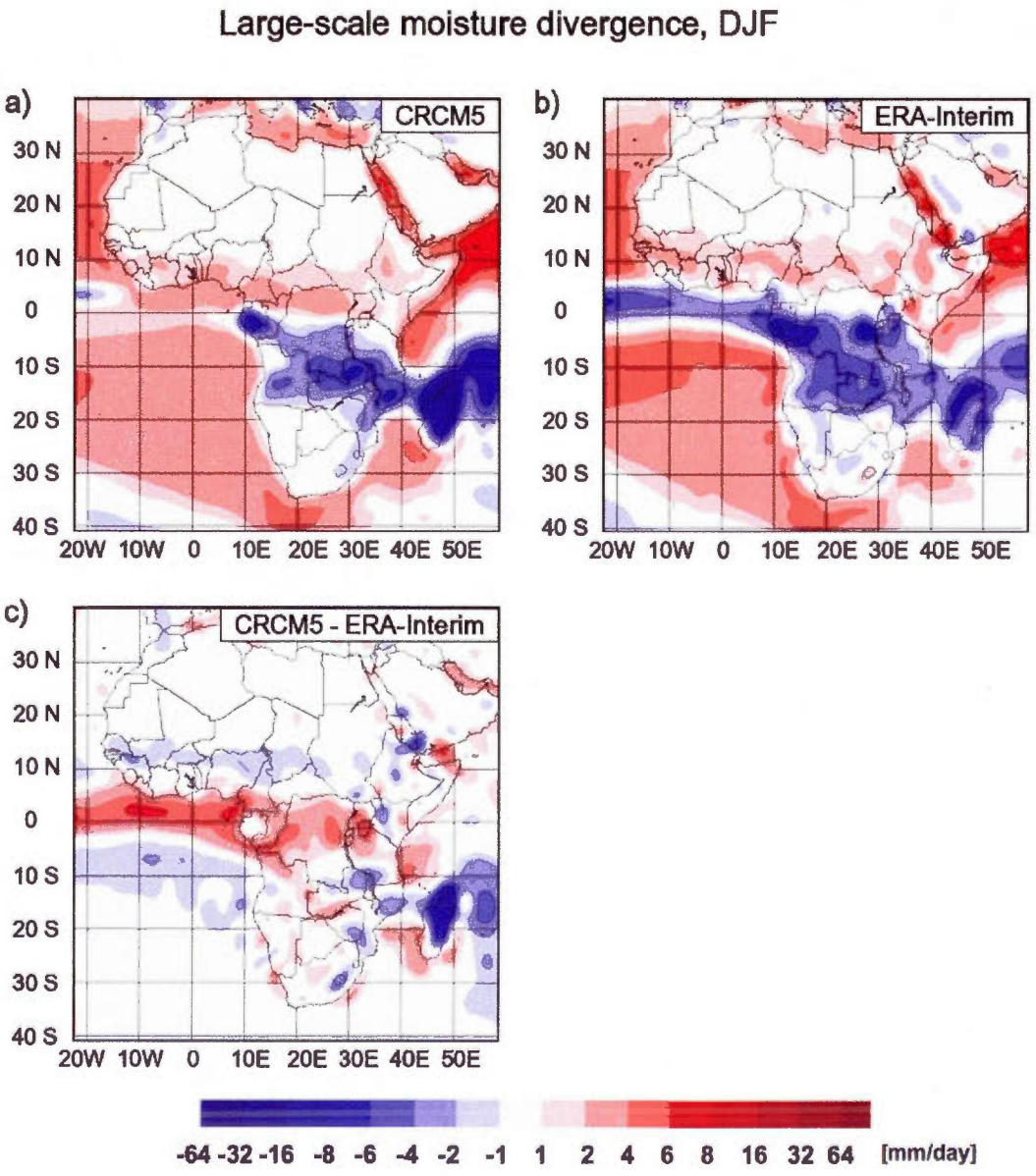

Fig. 4.23 Large scales of the mean moisture flux divergence (DJF, 1994-2008) calculated from the CRCM5 simulation (a) and ERA-Interim Reanalysis data (b), and the difference between them (c).

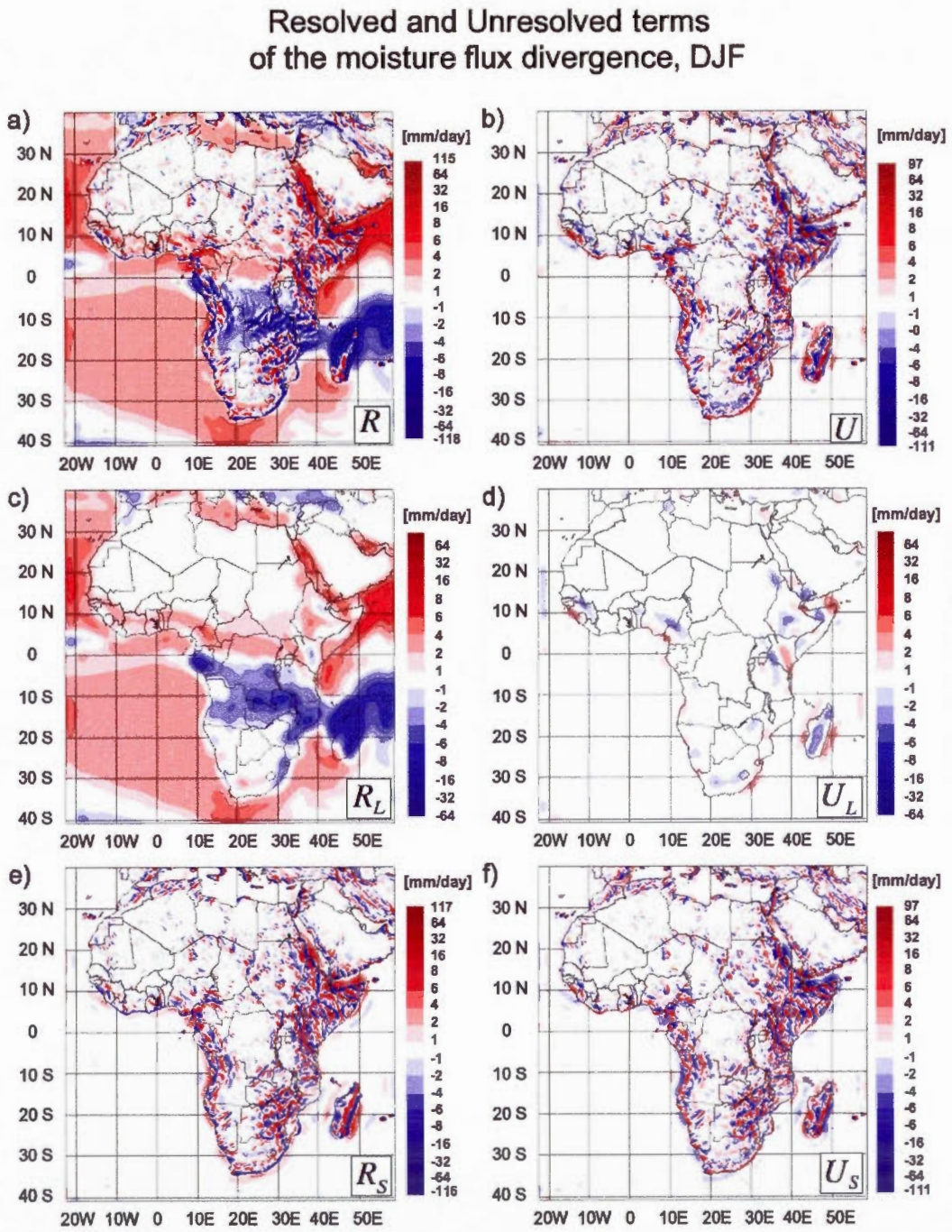

Fig 4.24 Resolved R (a) and unresolved U (b) components of the seasonal-mean divergence of the integrated moisture flux and respectively their decomposition into large scales (c and d) and small scales (e and f), DJF (1994-2008).

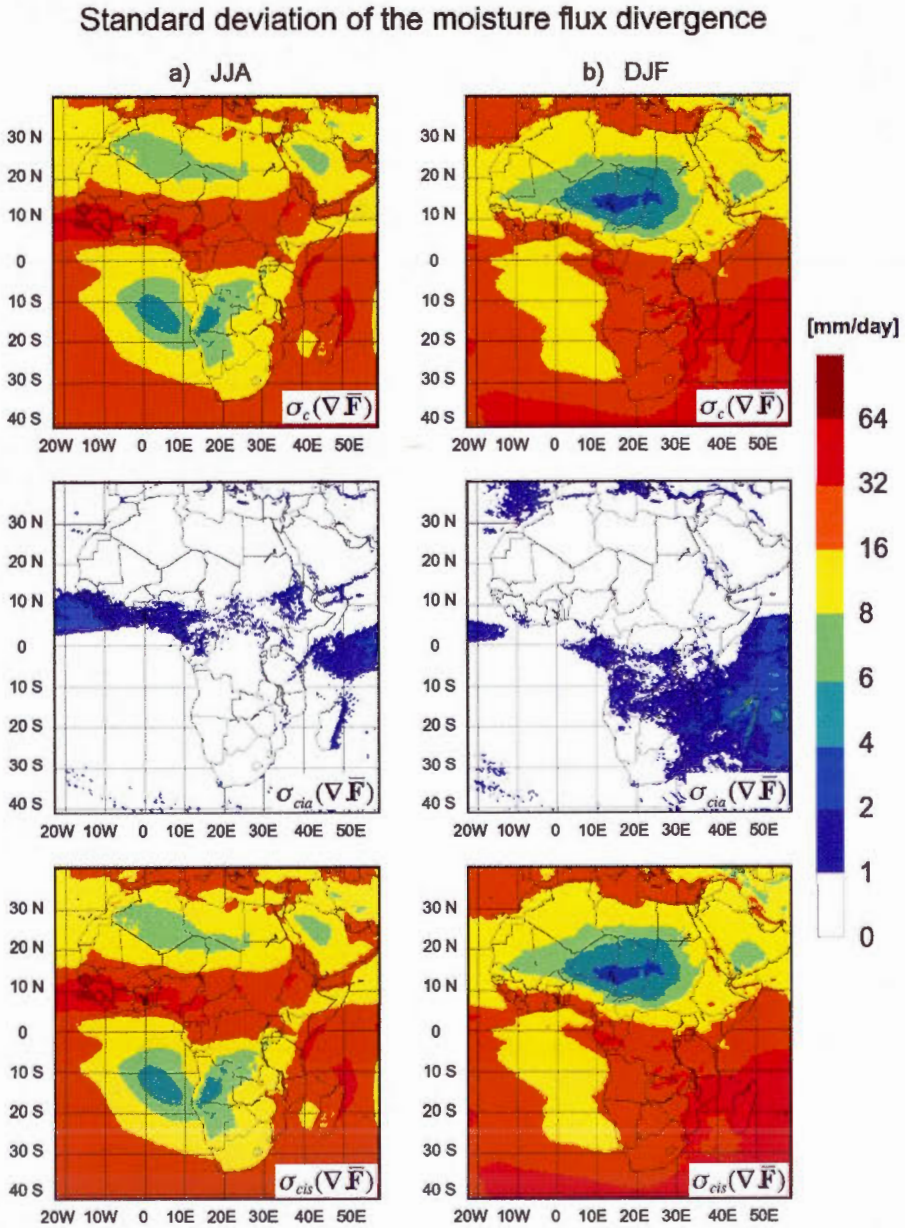

Fig. 5.1 Seasonal climatological standard deviation σ_c^2, interannual standard deviation σ_{cia}^2 and intra-seasonal standard deviation σ_{cis}^2 of transient perturbations for JJA (a) and DJF (b) 1994-2008, as simulated by CRCM5.

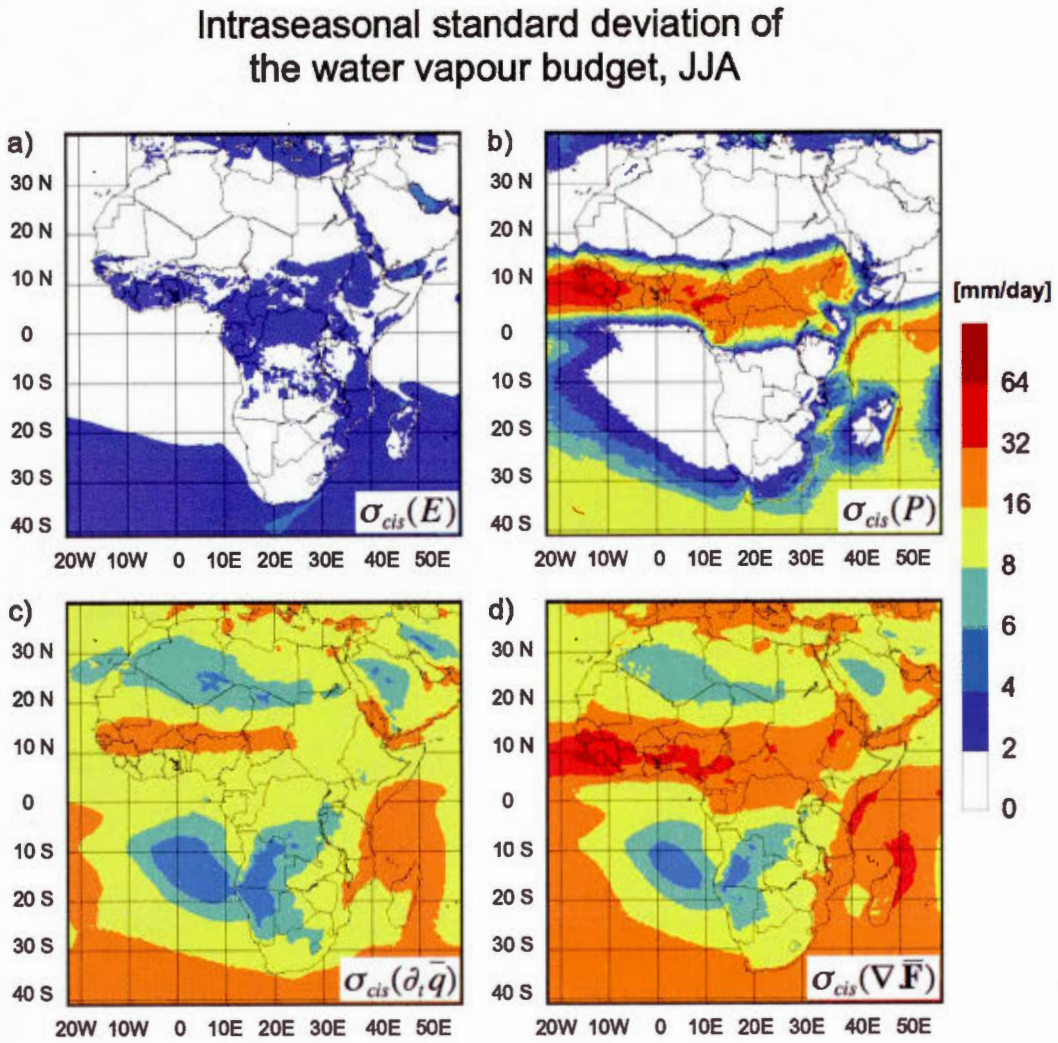

Fig. 5.2 Intraseasonal standard deviation of evapotranspiration (a), precipitation (b), vertically integrated water vapour tendency $\partial_t \bar{q}$ (c) and vertically integrated moisture flux divergence $\nabla \bullet \bar{\mathbf{F}}$ (d) for JJA 1994-2008.

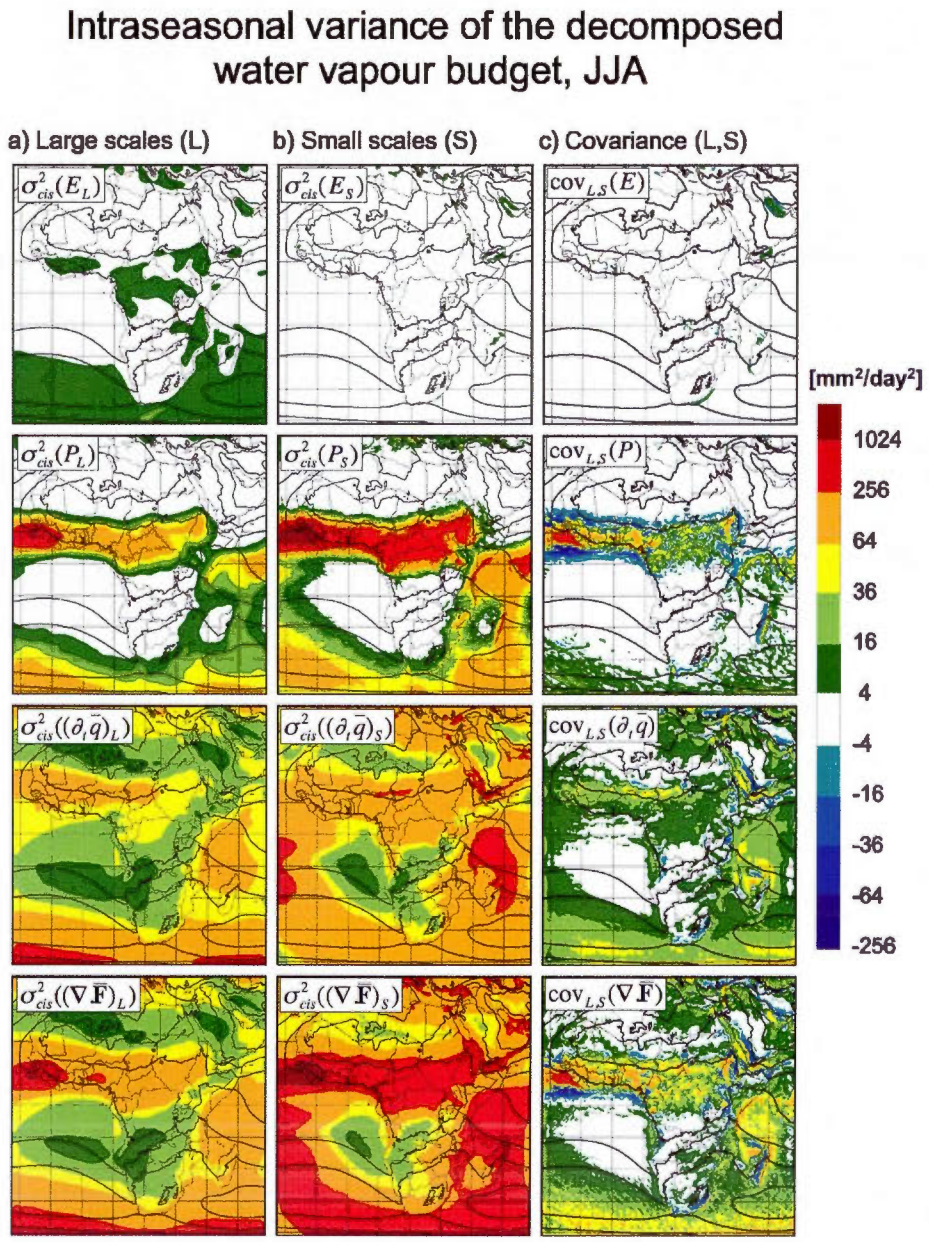

Fig. 5.3 Intraseasonal variance ($mm^2\ day^{-2}$) of the large scales (a) and small scales (b) of evapotranspiration E (first row), precipitation P (second row), precipitable water tendency $\partial_t \bar{q}$ (third row) and vertically integrated moisture flux divergence $\nabla \bullet \bar{\mathbf{F}}$ (bottom row), and the covariance between them (c), for JJA 1994-2008. Solid black lines represent sea-level pressure (the pressure values are as in the previous figures).

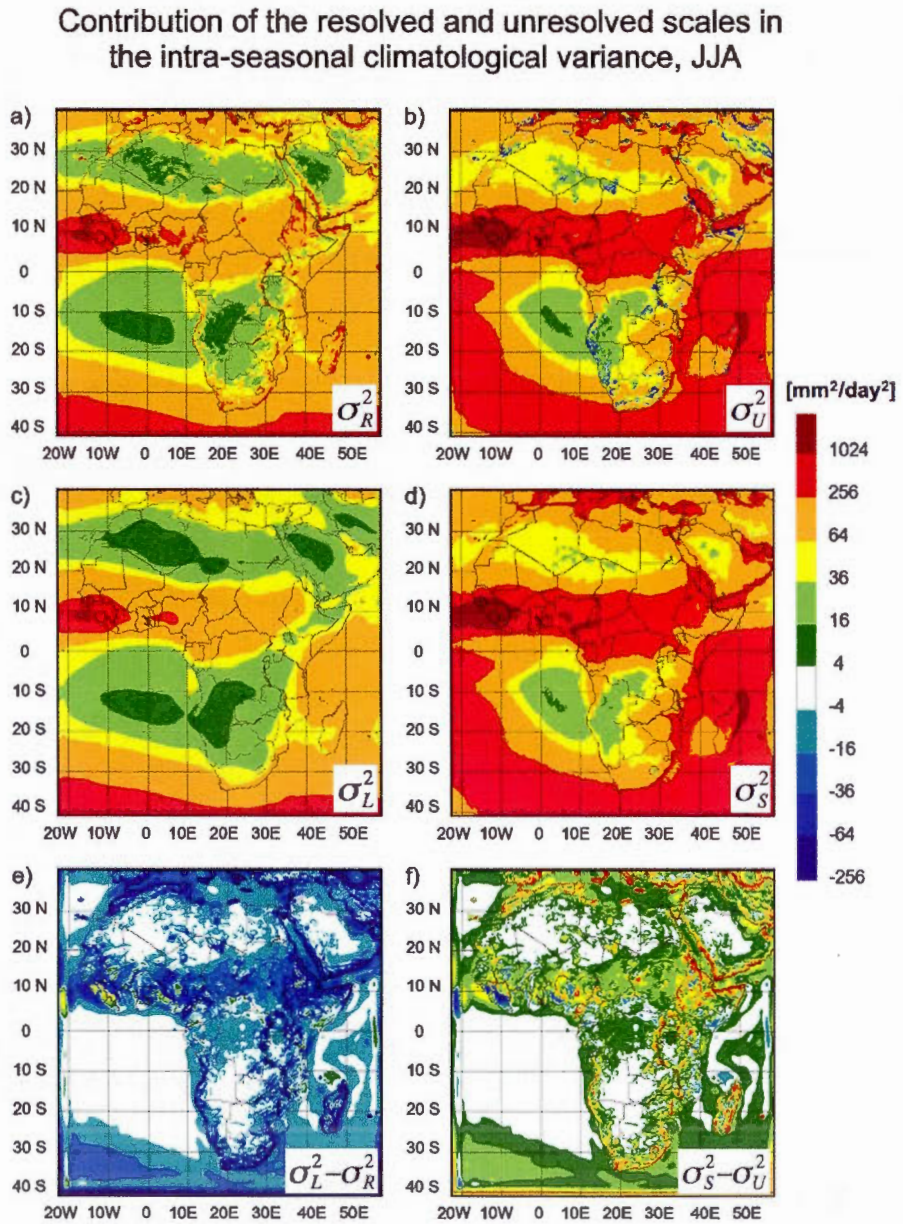

Fig. 5.4 Intra-seasonal climatological variance (JJA, 1994-2008) of the resolved scales σ_R^2 (a) and the contribution $\sigma_U^2 = \sigma_{cis}^2((\nabla \bullet \overline{\mathbf{F}})_U) + \mathrm{cov}_{R,U}(\nabla \bullet \overline{\mathbf{F}})$ from the unresolved scales (b), as well as the variance of the large scales σ_L^2 (c) of the divergence of the vertically integrated moisture flux and the contribution from the small scales $\sigma_S^2 = \sigma_{cis}^2((\nabla \bullet \overline{\mathbf{F}})_S) + \mathrm{cov}_{L,S}(\nabla \bullet \overline{\mathbf{F}})$ (d). Panels (e) and (f) represent respectively the difference between (a) and (c) and between (b) and (d).

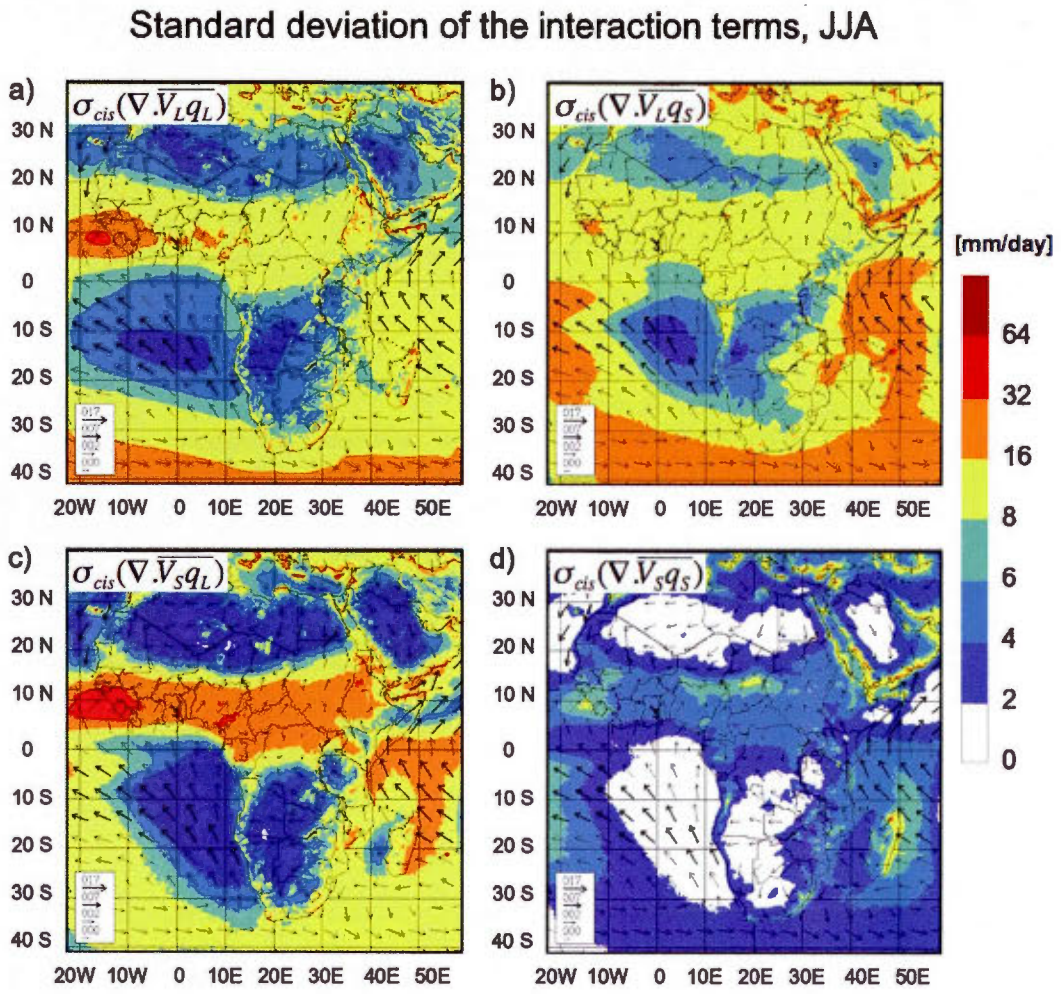

Fig. 5.5 Intra-seasonal climatological standard deviation of the four interaction terms of the vertically integrated atmospheric water flux divergence, with superimposed 1000 hPa-wind vectors (m s^{-1}), for JJA 1994-2008: variability due to the interaction between (a) large-scale wind and large-scale humidity, (b) large-scale wind and small-scale humidity, (c) small-scale wind and large-scale humidity and (d) small-scale wind and small-scale humidity.

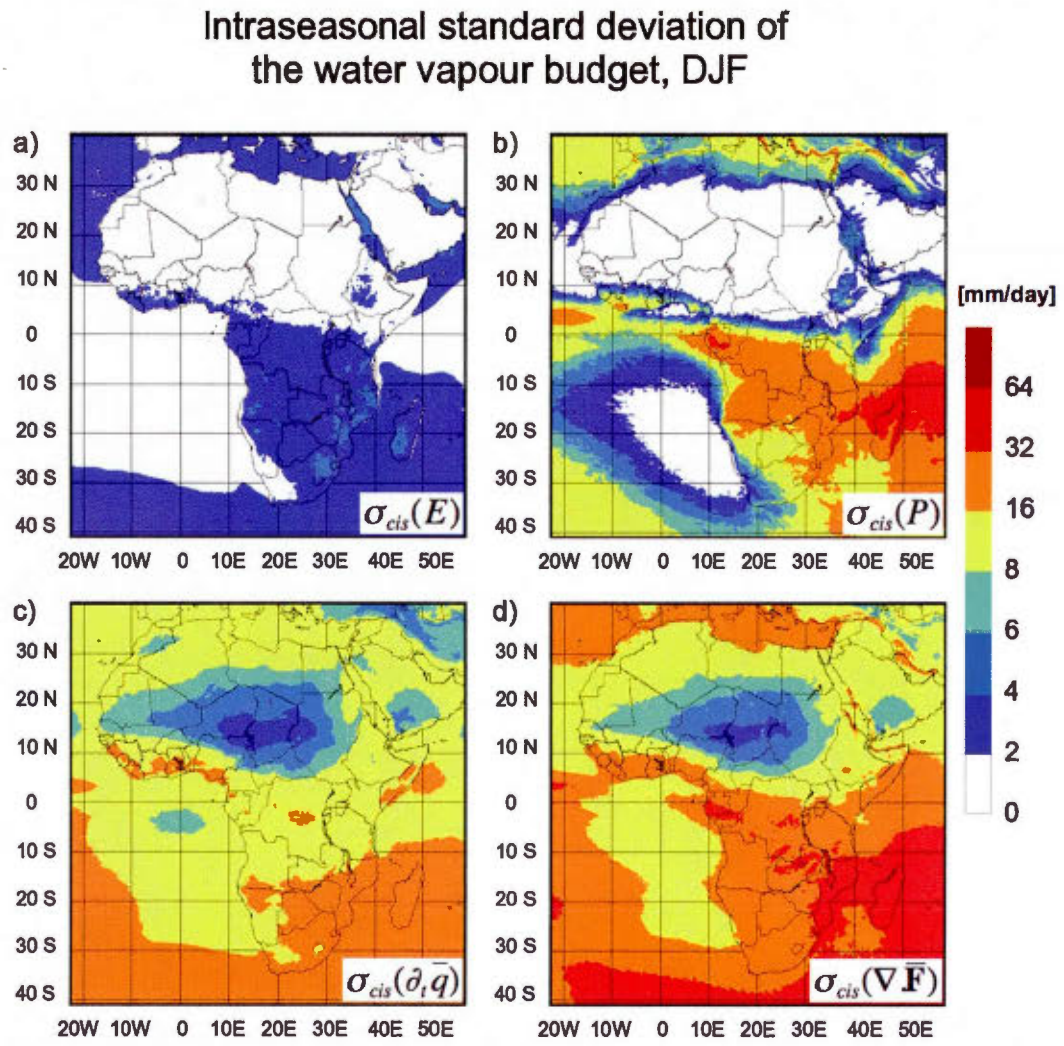

Fig. 5.6 Intraseasonal standard deviation of evapotranspiration (a), precipitation (b), vertically integrated water vapour tendency $\partial_t \bar{q}$ (c) and vertically integrated moisture flux divergence $\nabla \bullet \bar{\mathbf{F}}$ (d) for DJF 1994-2008

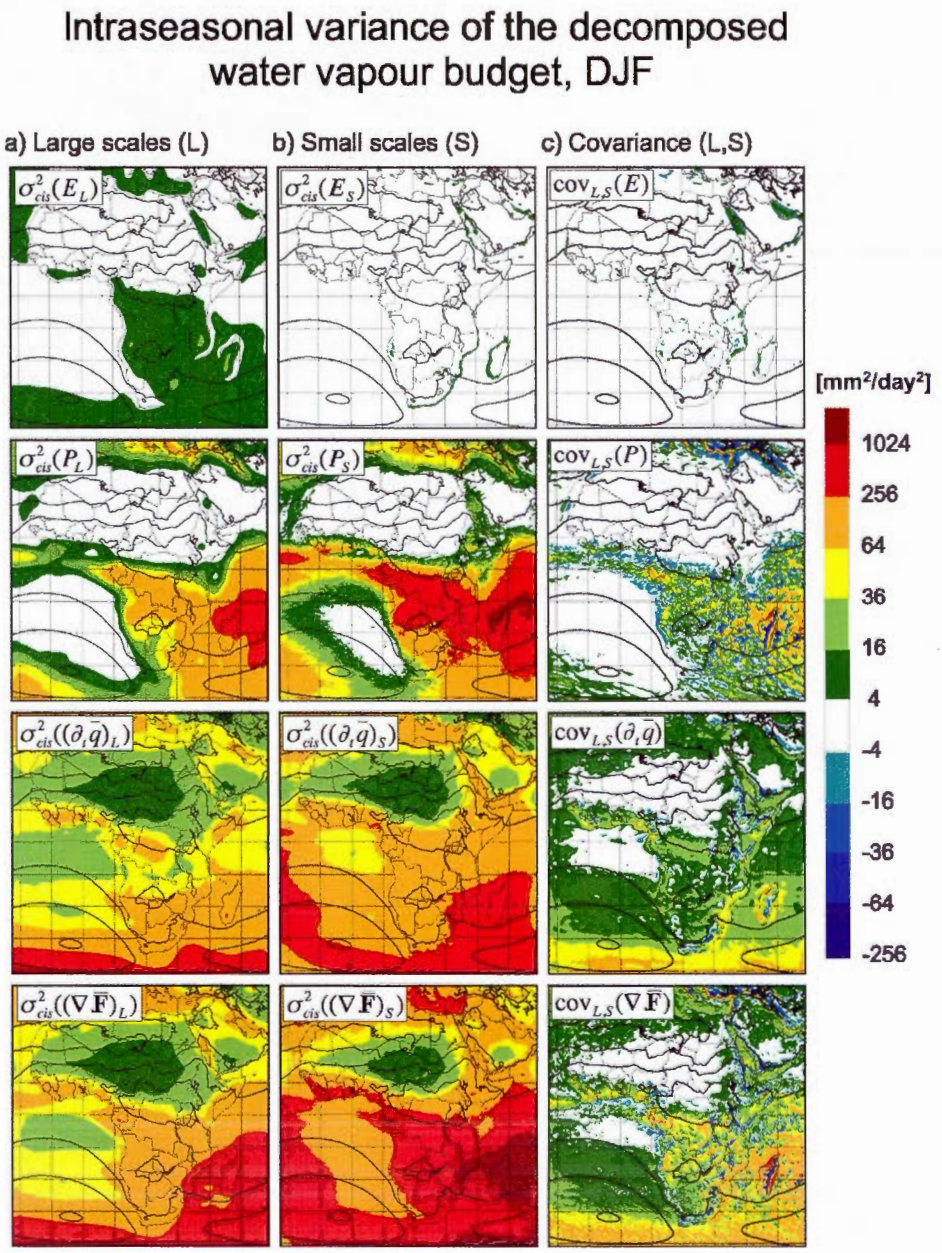

Fig. 5.7 Intraseasonal variance ($mm^2\ day^{-2}$) of the large scales (a) and small scales (b) of evapotranspiration E (first row), precipitation P (second row), precipitable water tendency $\partial_t \bar{q}$ (third row) and vertically integrated moisture flux divergence $\nabla \bullet \bar{\mathbf{F}}$ (bottom row), and the covariance between them (c), for DJF 1994-2008. Solid black lines represent sea-level pressure (the pressure values are as in the previous figures).

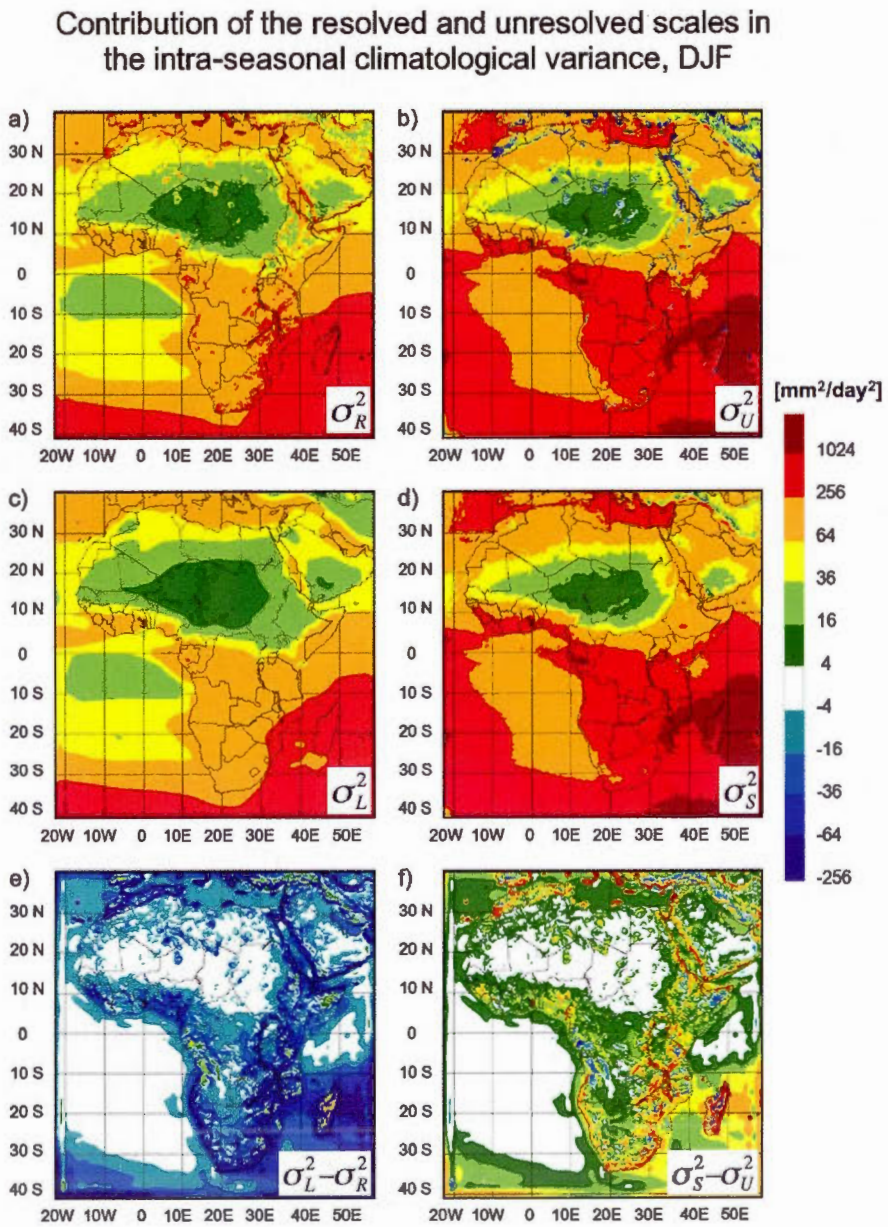

Fig. 5.8 Intra-seasonal climatological variance (DJF, 1994-2008) of the resolved scales σ_R^2 (a) and the contribution $\sigma_U^2 = \sigma_{cis}^2((\nabla \bullet \overline{\mathbf{F}})_U) + \mathrm{cov}_{R,U}(\nabla \bullet \overline{\mathbf{F}})$ from the unresolved scales (b), as well as the variance of the large scales σ_L^2 (c) of the divergence of the vertically integrated moisture flux and the contribution from the small scales $\sigma_S^2 = \sigma_{cis}^2((\nabla \bullet \overline{\mathbf{F}})_S) + \mathrm{cov}_{L,S}(\nabla \bullet \overline{\mathbf{F}})$ (d). Panels (e) and (f) represent respectively the difference between (a) and (c) and between (b) and (d).

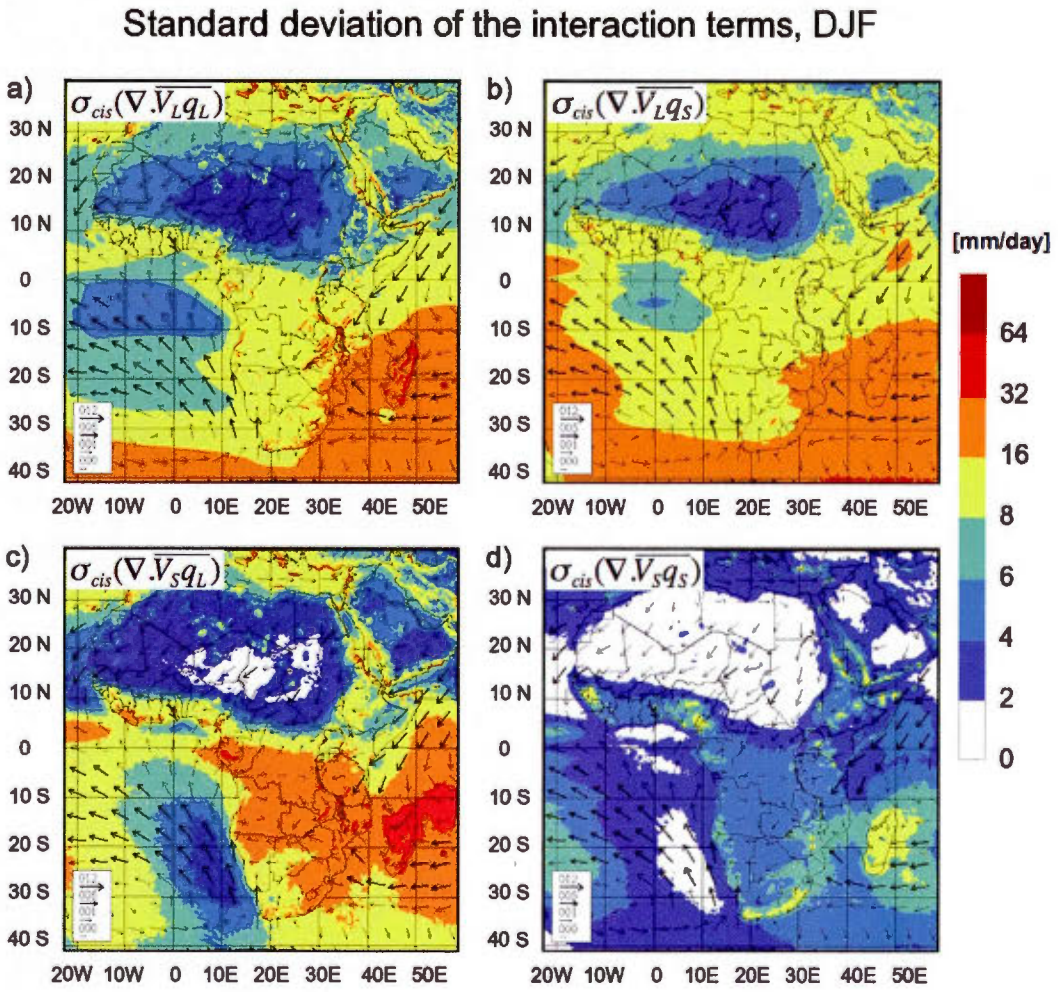

Fig. 5.9. Intra-seasonal climatological standard deviation of the four interaction terms of the vertically integrated atmospheric water flux divergence, with superimposed 1000 hPa-wind vectors (m s^{-1}), for DJF 1994-2008: variability due to (a) large-scale wind and large-scale humidity, (b) large-scale wind and small-scale humidity, (c) small-scale wind and large-scale humidity and (d) small-scale wind and small-scale humidity.

RÉFÉRENCES

Alexandru, A., R. de Elia, R. Laprise, L. Separovic et S. Biner. 2009. Sensitivity study of regional climate model simulations to large-scale nudging parameters. *Monthly Weather Review,* 137:1666–1686.

Berry, G.J. et C. Thorncroft. 2005. Case study of an intense African easterly wave. *Monthly Weather Review,* 133:752–766.

Bielli, S. et R. Laprise. 2006. A methodology for the regional-scale decomposed atmospheric water budget: application to a simulation of the Canadian Regional Climate Model nested by NCEP–NCAR reanalyses over North America. *Monthly Weather Review,* 134:854–873.

Bielli, S. et R. Laprise. 2007. Time mean and variability of the scale decomposed atmospheric water budget in a 25-year simulation of the Canadian Regional Climate Model over North America. *Climate Dynamics,* 29:763–777.

Bielli, S. et R. Roca. 2010. Scale decomposition of atmospheric water budget over West Africa during the monsoon 2006 from NCEP/GFS analyses. *Climate Dynamics,* 35:143-157, doi: 10.1007/s00382-009-0597-5

Boer, G.J. 1982. Diagnostic equations in isobaric coordinates. *Monthly Weather Review,* 110:1801–1820

Boko, M., I. Niang, A. Nyong, C. Vogel, A. Githeko, M. Medany, B. Osman-Elasha, R. Tabo et P. Yanda. 2007. IPCC Fourth Assessment Report: Climate Change 2007, Working Group II: Impacts, Adaptation and Vulnerability, Chapter 9: Africa. Cambridge University Press, Cambridge UK, 433-467.

Breson, R. et R. Laprise. 2011. Scale-decomposed atmospheric water budget over North America as simulated by the Canadian Regional Climate Model for current and future climates. *Climate Dynamics,* 36:365-384, doi: 10.1007/s00382-009-0695-4.

Burpee, R. W. 1972. The origin and structure of easterly waves in the lower troposphere of North Africa. *Journal of Atmospheric Sciences,* 29:77–90.

Cadet, D. L. et N. O. Nnoli. 1987. Water vapor transport over Africa and the Atlantic Ocean during summer 1979. *Quarterly Journal of the Royal Meteorological Society,* 113:581–602.

Castro, C. L., R. A. Pielke Sr. et G. Leoncini, 2005. Dynamical downscaling: Assessment of value retained and added using the Regional Atmospheric Modeling System (RAMS), *Journal of Geophysical Research,* 110, D05108, doi:10.1029/2004JD004721.

Chauvin, F., J. F. Royer et H. Douville. 2005. Interannual variability and predictability of African easterly waves in a GCM. *Climate Dynamics,* 24:523-544. doi: 10.10007/s00382-004-0507-9.

Colin, J., M. Déqué, R. Radu et S. Somot. 2010. Sensitivity study of heavy precipitation in Limited Area Model climate simulations: influence of the size of the domain and the use of the spectral nudging technique. *Tellus*, 62A:591–604.

Cook, K. 2000. The South Indian Convergence Zone and Interannual Rainfall Variability over Southern Africa. *Journal of Climate,* 13:3789–3804, doi: http://dx.doi.org/10.1175/1520-0442(2000)013<3789:TSICZA>2.0.CO;2.

Côté, J., J. G. Desmarais, S. Gravel, A. Méthot, A. Patoine, M. Roch et A. Staniforth. 1998a. The operational CMC-MRB global environmental multiscale (GEM) model. Part I: Design considerations and formulation. *Monthly Weather Review,* 126:1373-1395.

Côté, J., J. G. Desmarais, S. Gravel, A. Méthot, A. Patoine, M. Roch et A. Staniforth. 1998b. The operational CMC-MRB global environmental multiscale (GEM) model. Part II: Results. *Monthly Weather Review,* 126:1397-1418.

Crimp, S. J., J. R. E. Lutjeharms et S. J. Mason. 1998. Sensitivity of a tropical-temperate trough to sea-surface temperature anomalies in the Agulhas retroflection region. *Water SA*, 24(2):93-101.

Davies, H.C. 1976. A lateral boundary formulation for multi-level prediction models. *Quarterly Journal of the Royal Meteorological Society*, 102: 405-418.

Dee, D. P., S. M. Uppala, A. J. Simmons, P. Berrisford, P. Poli, S. Kobayashi, U. Andrae, M. A. Balmaseda, G. Balsamo, P. Bauer, P. Bechtold, A. C. M. Beljaars, L. van de Berg, J. Bidlot, N. Bormann, C. Delsol, R. Dragani, M. Fuentes, A. J. Geer, L. Haimberger, S. B. Healy, H. Hersbach, E. V. Hólm, L. Isaksen, P. Kållberg, M. Köhler, M. Matricardi, A. P. McNally, B. M. Monge-Sanz, J.-J. Morcrette, B.-K. Park, C. Peubey, P. de Rosnay, C. Tavolato, J.-N. Thépaut et F. Vitar. 2011. The ERA-Interim reanalysis: configuration and performance of the data assimilation system. *Quarterly Journal of the Royal Meteorological Society,* 137:553-828, doi:10.1002/qj.828.

Denis, B., J.Cote et R. Laprise. 2002. Spectral decomposition of twodimensional atmospheric fields on limited-area domains using the discrete cosine transforms (DCT). *Monthly Weather Review,* 130:1812-1829.

Desbois, M., T. Kayiranga, B. Gnamien, S. Guessous et L. Picon. 1988. Characterization of some elements of the Sahelian climate and their interannual variations for July 1983, 1984 and 1985 from the analysis of Meteosat ISCCP data. *Journal of Climate,* 1:867–904, doi:10.1175/1520-0442(1988)001\0867:COSEOT[2.0.CO;2.

Diedhiou, A., S. Janicot, A. Viltard, P. de Felice et H. Laurent. 1999. Easterly wave regimes and associated convection over West Africa and tropical Atlantic: results from NCEP/NCAR and ECMWF reanalysis. *Climate Dynamics*, 15:795–822.

Di Luca, A., R. de Elia, R. Laprise. 2012a. Potential for added value in precipitation simulated by high-resolution nested Regional Climate Models and observations. *Climate Dynamics,* 38:1229–1247, doi:10.1007/s00382-011-1068-3.

Di Luca, A., R. de Elia, R. Laprise. 2011b. Potential for added value in RCM-simulated surface temperature. *Climate Dynamics,* doi:10.1007/s00382-012-1384-2.

Drobinski, P., B. Sultan et S. Janicot. 2005. Role of the Hoggar massif in the West Africa monsoon onset. *Geophysical Research Letters*, 32, doi:10.1029/2004GL020710.

Feser, F. et H. von Storch. 2005. A spatial two-dimensional discrete filter for limited-area-model evaluation purposes. *Monthly Weather Review,* 133:1774–1786.

Feser, F. 2006. Enhanced detectability of added value in limited-area model results separated into different spatial scales. *Monthly Weather Review,* 134:2180–2190.

Feser, F., B. Rockel, H. von Storch, J. Winterfeldt et M. Zahn. 2011. Regional Climate Models Add Value to Global Model Data: A Review and Selected Examples. *Bulletin of the American Meteorological Society,* 92:1181–1192, doi:10.1175/2011BAMS3061.1.

Giorgi, F. et M.R. Marinucci. 1996. An investigation of the sensitivity of simulated precipitation to model resolution and its implications for climate studies. *Monthly Weather Review,* 124:148–16.

Giorgi, F., C. Jones et G. R. Asrar. 2009. Addressing climate information needs at the regional level: the CORDEX framework. *WMO Bulletin*, vol.58(3), 175-183.

Grasso, L. D. 2000. The differentiation between grid spacing and resolution and their application to numerical modeling. *Bulletin of the American Meteorological Society*, 81:579-580.

Hall, N. M. J., G. N. Kiladis, C. D. Thorncroft. 2006. Three-Dimensional Structure and Dynamics of African Easterly Waves. Part II: Dynamical Modes. *Journal of Atmospheric Sciences,* 63:2231–2245.

Hernández-Diaz, L., R. Laprise, L. Sushama, A. Martynov, K. Winger et B. Dugas. 2012. Climate simulation over CORDEX Africa domain using the fifth-generation

Canadian Regional Climate Model (CRCM5). *Climate Dynamics* doi: 10.1007/s00382-012-1387-z.

Janicot, S. 1992. Spatio-temporal variability of West African rainfall. Part II : Associated surface and air masses characteristics. *Journal of Climate,* 5:499-511.

Jones, C., P. Samuelsson, U. Willén, G. Nikulin et A. Ullerstig. 2009. Simulating Precipitation over Africa with a new version of RCA. *Mistra-SWECIA Newsletter,* 1:09, June 2009, pages 14-18.

Jury, M. R. et B. Pathack. 1991. A study of climate and weather variability over the tropical southwest Indian Ocean. *Meteorology and Atmospheric Physics*, 47:37–48.

Jury, M. R., H. R. Valentine et J. R. E. Lutjeharms. 1993. Influence of the Agulhas Current on Summer Rainfall along the Southeast Coast of South Africa. *Journal of Applied Meteorology*, 32:1282–1287, doi:http://dx.doi.org/10.1175/1520-0450(1993)032<1282:IOTACO>2.0.CO;2.

Kain, J.S. et J.M. Fritsch. 1990. A one-dimensional entraining/detraining plume model and application in convective parameterization. *Journal of Atmospheric Sciences,* 47: 2784-2802.

Kiladis, G. N., C. D. Thorncroft et N. M. J. Hall. 2006. Three-dimensional structure and dynamics of African easterlywaves. Part I: Observations. *Journal of Atmospheric Sciences,* 63:2231–2245.

Kiladis, G.N., et K.M. Weickmann. 1997. Horizontal structure and seasonality of large-scale circulations associated with submonthly tropical convection. *Monthly Weather Review,* 125:1997-2013.

Laprise, R. 2003. Resolved scales and nonlinear interactions in limited-area models. *Journal of Atmospheric Sciences,* 60:768-779.

Laprise, R. 2008. Regional climate modelling. *Journal of Computational Physics*, 227:3641–3666.

Lawford, R. G., J. Roads, D. P. Lettenmaier et P. Arkin. 2007. GEWEX contributions to large-scale hydrometeorology. *Journal of Hydrometeorology,* 8:629–641.

Le Barbé, L. et T. Lebel. 1997. Rainfall climatology of the HAPEX-Sahel region during the years 1950-1990. *Journal of Hydrology,* 188-189:43–73.

Lebel, T., J. D. Taupin et N. D'Amato. 1997. Rainfall monitoring during HAPEX-Sahel. 1. General rainfall conditions and climatology. *Journal of Hydrology,* 188-189:74-96.

Leduc, M., R. Laprise, M. Moretti-Poisson et J.-P. Morin. 2011. Sensitivity to domain size of mid-latitude summer simulations with a regional climate model. *Climate Dynamics,* 37:343-356, doi: 10.1007/s00382-011-1008-2.

Li, J. et H.W. Barker. 2005. A radiation algorithm with correlated-k distribution. Part I: local thermal equilibrium. *Journal of Atmospheric Sciences,* 62:296-309.

Maddox, R. A. 1980. Meoscale Convective Complexes. *Bulletin of the American Meteorological Society,* 61:1374–1387, doi: http://dx.doi.org/10.1175/1520-0477(1980)061<1374:MCC>2.0.CO;2.

Maloney, E. D. et J. Shaman. 2008. Intraseasonal variability of the West African monsoon and Atlantic ITCZ. *Journal of Climate,* 21:2898–2918.

Mason, S. et M. Jury. 1997. Climatic variability and change over southern Africa: A reflection on underlying processes. *Progress in Physical Geography*, 21:23–50.

Mathon, V., A. Diedhiou et H. Laurent. 2002a. Relationship between easterly waves and mesoscale convective systems over the Sahel. *Geophysical Research Letters*, 29:57:1-4.

Mathon, V., H. Laurent, et T. Lebel. 2002b. Mesoscale Convective System Rainfall in the Sahel. *Journal of Applied Meteorology*, 41:1081–1092. doi: http://dx.doi.org/10.1175/1520-0450(2002)041<1081:MCSRIT>2.0.CO;2.

McHugh, M. J. et J. C. Rogers. 2001. North Atlantic Oscillation influence on precipitation variability around the Southeast African Convergence Zone, *Journal of Climate,* 14:3631-3642.

Mekonnen, A. et W. B. Rossow. 2011. The interaction between deep convection and easterly waves over tropical North Africa: A weather state perspective. *Journal of Climate,* 24:4276-4294.

Meynadier, R., O. Bock, F. Guichard, A. Boone, P. Roucou et J.-L. Redelsperger. 2010a. West African Monsoon water cycle: 1. A hybrid water budget data set, *Journal of Geophysical Research,* 115:D19106, doi:10.1029/2010JD013917.

Meynadier, R., O. Bock, S. Gervois, F. Guichard, J.-L. Redelsperger, A. Agustí-Panareda et A. Beljaars. 2010b. West African Monsoon water cycle: 2. Assessment of numerical weather prediction water budgets, *Journal of Geophysical Research*, 115:D19107, doi: 10.1029/2010JD013919.

Mohino, E., S. Janicot, H. Douville et L. Li. 2012. Impact of summer MJO on West Africa using nudged climate simulations. *Climate Dynamics.* 38:2319-2334. doi: 10.1007/s00382-011-1206-y.

Nicholson, S. E. et J. P. Grist. 2003. The seasonal evolution of atmospheric circulation over West Africa and Equatorial Africa. *Journal of Climate*, 16:1013-1030.

Palmer, T. N. 1986. Influence of the Atlantic, Pacific and Indian oceans on Sahel rainfall. *Nature*, 322:251-253.

Peixoto, J. et A. Oort. 1992. Physics of climate. American Institute of Physics, USA, p.520.

Peugeot, C., F. Guichard, O. Bock, D. Bouniol, M. Chong, A. Boone, B. Cappelaere, M. Gosset, L. Besson, Y. Lemaître, L. Séguis, A. Zannou, S. Galle et J.-L. Redelsperger. 2011. Mesoscale water cycle within the West African Monsoon, *Atmospheric Science Letters*, 12:45–50, doi:10.1002/asl.309.

Peyrillé, P., J.-P. Lafore et J.-L. Redelsperger. 2007. An idealized two-dimensional framework to study the West African monsoon. Part I: Validation and key controlling factors. *Journal of Atmospheric Sciences*, 64:2765-2782.

Peyrillé, P. et J.-P. Lafore. 2007. An idealized two-dimensional framework to study the West African monsoon. Part II: Forcing by large-scale advections and the diurnal cycle. *Journal of Atmospheric Sciences*, 64:2783-2803.

Pielke, R. A. 1991. A recommended specifie definition of "resolution". *Bulletin of the American Meteorological Society*, 12:1914.

Prömmel, K., B. Geyer, J. M. Jones et M. Widmann. 2010. Evaluation of the skill and added value of a reanalysis-driven regional simulation for Alpine temperature. *International Journal of Climatology*, 30:760–773. doi: 10.1002/joc.1916.

Redelsperger, J.-L., A. Diongue, A. Diedhiou, J. P. Ceron, M. Diop, J. F. Gueremy et J.-P. Lafore. 2002. Multi-scale desciption of a Sahelain synopticweather system representative of theWest African monsoon. *Quarterly Journal of the Royal Meteorological Society*, 128:1229–1257.

Rockel, B., C. Castro, Sr. R. Pielke, H. von Storch et G. Lencini. 2008. Dynamical downscaling: Assessment of model system dependent retained and added variability for two different regional climate models. *Journal of Geophysical Research*, 113:D21107, doi:10.1029/2007JD009461

Rummukainen, M. 2010. State-of-the-art with regional climate models. Wiley Interdisciplinary Reviews: *Climatic Change* 1:82–96.

Semazzi, F. H. M. et L. Sun. 1997. The role of orography in determining the Sahelian climate. *International Journal of Climatology,* 17:581–596.

Shillington, F., C. J. C. Reason, C M. D. Rae, P. Florenchie, et P. Penven. 2006. Large scale physical variability of the Benguela current large marine ecosystem (BCLME),

in: V. Shannon, G. Hempel, P. Malanotte-Rizzoli, C. Moloney, J. Woods (Eds.), Benguela: Predicting a Large Marine Ecosystem, Chapter 4, Large Marine Ecosystems, vol. 14 (2006), p. 49–70.

Sultan, B., S. Janicot et A. Diedhiou. 2003. West African monsoon dynamics.Part I: Documentation of intraseasonal variability. *Journal of Climate*, 16:3389–3406.

Sundqvist, H., E. Berge et J.E. Kristjansson. 1989. Condensation and Cloud Parameterization Studies with a Mesoscale Numerical Weather Prediction Model. *Monthly Weather Review*, 117:1641-1657.

Sylla, M. B., E. Coppola, L. Mariotti, F. Giorgi, P. M. Ruti, A. Dell'Aquila, et X. Bi. 2010a. Multiyear simulation of the African climate using a regional climate model (RegCM3) with the high resolution ERA-interim reanalysis. *Climate Dynamics*, 35:231–247. doi: 10.1007/s00382-009-0613-9.

Sylla, M.B., A. Dell'Aquila, P. M. Ruti, et F. Giorgi. 2010b. Simulation of the intraseasonal and the interannual variability of rainfall over West Africa with a Regional Climate Model (RegCM3) during the monsoon period. *International Journal of Climatology,* 30:1865–1883.

Thorncroft, C. D. et M. Blackburn. 1999. Maintenance of the African easterly jet. *Quarterly Journal of the Royal Meteorological Society*, 125:763–786.

Thorncroft, C. D. et K. L. Hodges. 2001. African easterly wave variability and its relationship to Atlantic tropical cyclone activity *Journal of Climate*, 14:1166–1179.

Thorncroft, C. D., H. Nguyen, C. Zhang et P. Peyrillé. 2011. Annual cycle of the West African Monsoon—regional circulations and associated water vapour transport. *Quarterly Journal of the Royal Meteorological Society,* 137:129–147.

Todd, M. C., R. Washington et P. I. Palmer. 2004. Water vapour transport associated with tropical-temperate trough systems over Southern Africa and the southwest Indian Ocean. *International Journal of Climatology,* 24:555–568.

Trenberth, K. E. 1998. Atmospheric moisture residence times and cycling: Implications for rainfall rates and climate change. *Climatic Change*, 39:667–694.

Trenberth, K. E. 1999a. Atmospheric Moisture Recycling: Role of Advection and Local Evaporation. *Journal of Climate,* 12:1368–1381.

Trenberth, K. E. 1999b. Conceptual framework for changes of extremes of the hydrological cycle with climate change. *Climatic Change,* 42:327–339.

Trenberth, K. E., A. Dai, R. Rasmussen et D. Parsons. 2003. The changing character of precipitation. *Bulletin of the American Meteorological Society*, 84:1205-1217.

Uppala, S., D. Dee, S. Kobayashi, P. Berrisford et A. Simmons. 2008. Towards a climate data assimilation system: status update of ERA-Interim. *ECMWF Newsletter,* 115:12-18.

Van den Heever. S. C, P. C. D'Abreton et P. D. Tyson. 1997. Numerical simulation of tropical-temperate troughs over southern Africa using the CSU RAMS model. *South African Journal of Science*, 93:359-365.

Verseghy, D. L. 1991. CLASS-A Canadian Land Surface Scheme for GCMS, I. Soil Model. *International Journal of Climatology*, 11:111-133.

Verseghy, D. L., N. A. McFarlane et M. Lazare. 1993. CLASS-A Canadian land surface scheme for GCMS, II. Vegetation model and coupled runs. *International Journal of Climatology, 13*:347-370.

Verseghy, D. L. 2000. The Canadian Land Surface Scheme (CLASS): its history and future. *Atmosphere-Ocean*, 38:1, 1-13

Vigaud, N., Y. Richard, M. Rouault et N. Fauchereau. 2007. Water vapor transport from the tropical Atlantic and summer rainfall in tropical southern Africa. *Climate Dynamics*, 28:113–123.

Von Storch, H., H. Langenberg et F. Feser. 2000. A spectral nudging technique for dynamical downscaling purposes. *Monthly Weather Review*, 128:3664–3673.

Yeh, K.-S., S. Gravel, A. Méthot, A. Patoine, M. Roch et A. Staniforth. 2002. The operational CMC-MRB global environmental multiscale (GEM) model. Part III: Non-hydrostatic formulation. *Monthly Weather Review*, 130:339-356.

Zadra, A., D. Caya, J. Côté, B. Dugas, C. Jones, R. Laprise, K. Winger et L.-P. Caron. 2008. The next Canadian Regional Climate Model. *Physics in Canada*, 64(2):75-83.

Zhang, C., D. S. Nolan, C. D. Thorncroft et H. Nguyen. 2008. Shallow meridional circulations in the tropical atmosphere. *Journal of Climate*, 21:3453–3470.